DETECTION OF BREAST CANCER WITH ELECTRICAL IMPEDANCE MAMMOGRAPHY

Gerald SZE

BSc (Engineering Physics) & MSc (Digital Signal and Image Processing)

SUBMITTED FOR THE DEGREE OF DOCTOR OF PHILOSOPHY AT THE UNIVERSITY OF SUSSEX

SCHOOL OF ENGINEERING AND DESIGN

UNIVERSITY OF SUSSEX

BRIGHTON UK

May 2012

Dedicated to my parents,

my wife Pik-Yee and our beloved son Nathaniel

SUMMARY

Electrical Impedance Tomography (EIT) is a medical imaging technique that reconstructs internal electrical conductivity distribution of a body from impedance data that is measured on the body surface, and Electrical Impedance Mammography (EIM) is the technique that applies EIT in breast cancer detection. The use of EIM for breast cancer identification is highly desirable because it is a non-invasive and low-cost imaging technology. EIM has the potential in detecting early stage cancer, however there are still challenges that hindering EIM to be provided as a routine health care system. There are three major groups of obstacles. One is the hardware design, which includes the selection of electronic components, electrode-skin contacting methods, etc. Second is theoretical problems such as electrode configurations, image reconstruction and regularization methods. Third is the development of analysis methods and generation of a cancerous tissue database. Research reported in this thesis strives to understand these problems and aims to provide possible solutions to build a clinical EIM system.

The studies are carried out in four parts. First the functionalities of the Sussex Mk4 EIM system have been studied. Sensitivity of the system was investigated to find out the strength and weakness of the system. Then work has been made on image reconstruction and regularization methods in order to enhance the system's endurance to noise, also to balance the reconstruction conductivity distribution throughout the reconstructed object. Then a novel cancer diagnosis technique was proposed. It was developed based on the electrical property of human breast tissue and the behaviour or systematic noise, to provide repeatable results for each patient. Finally evaluation has been made on previous EIM systems to find out the major problems. Based on sensitivity analysis, an optimal combined electrode configuration has been proposed to improve sensitivity.

The system has been developed and produced meaningful clinical images. The work makes significant contributions to society. This novel cancer diagnosis method has high accuracy for cancer identification. The combined electrode configuration has also provided flexibilities in the designing of current driving and voltage receiving patterns, thus sensitivity of the EIM system can be greatly improved.

ACKNOWLEDGEMENTS

I would like to express my gratitude to my supervisor Dr. Wei Wang, who gave me the opportunity to join the Biomedical Engineering Research group to start my research journey. I have learnt a lot from him during these days. And I will never forget great help from him as well as the delicious home-made Chinese food he shared when we were discussing the research work. Prof. Chris Chatwin, Dr. Rupert Young, Dr. Phil Birch for their teaching on my studies, advices on my publication and arrangement of my VIVA examination. Dr. Xin Kai Li for his suggestions on my mathematical problems and also be my external examiner. Also thanks to my friends and colleagues: Yi He, Louis Lu, Dr. Li Wang for the fruitful discussions and their assistance when I was in Leicester. Dr. Guofeng Qiao for his acompany through all these years, also for his selfless help, support and advice in all aspects, also for his and his wife Lina's hospitality. Chris Beardmore and Yajun Xing for the friendship and the teaching on electronics. Dr. James Wheeler, Dr. Martin Brien, Nevis Beqo, Rabia Bilal, Xiaolin Zhang, Fan Zheng, Wei Duan, Weida, Nan Li, Sally Owen, Smita Parmar and all other members within the Biomedical Engineering Research Group for their support, friendship and assistance.

I have to say thank you to Prof. David Barber for all his time and guidance, also for the directions he gave on my research, especially for the feedback on my rough notes. Dr. Andre Ng for his advice when I cannot see the way out, also his wife Dr. Carmen Ng for the caring and hospitality on my last days in Leicester.

I must take this opportunity to thank you my sister Sarah and brother-in-law Stanley for all the prayers, hospitality and the mentally/financially/academically support in all these years. I can see all these are because of love. My dad and mum, who gave me confidence and allowed me to choose my own path in each step of my life.

Lastly I need to say thank you to God, who led my beloved wife Pik-Yee to me, who sacrifice most of her time and holidays to support and encourage me to finish the PhD study, which I never believe I can finish it until the last minute of my VIVA examination.

CONTENTS

LIST OF PUBLICATION

First author conference papers:

1. **G Sze**, W Wang , G Qiao, L Wang, B Tunstall, Da-Wei Gu and M Tang, Preliminary Investigation of Correlation Between In-Vitro Specimen Measurement and In-Vivo Imaging Data from ROI Analysis. *13th International Conference on Electrical Bioimpedance and the 8th Conference on Electrical Impedance Tomography ICEBI 2007, August 29th - September 2nd 2007, Graz, Austria*
2. **G Sze**, D C Barber, G Qiao, N Huber, N Beqo and W Wang, Image Reconstruction for 3D Electrical Impedance Mammography. *10th* International *Conference on Electrical Bioimpedance, April 4th - 8th 2010, Florida, USA*
3. **G Sze**, N Beqo, N Huber, B Tunstall and W Wang, Signal calibration for a Electrical Impedance Mammography system. *Journal of Physics: Conference Series 224 (2010)*
4. **G Sze**, W Wang, D C Barber and N Huber, Preliminary study of conductivity changes of planar electrode system of Sussex Mk4 Electrical Impedance Mammography. *12th International Conference in Electrical Impedance Tomography EIT 2011, May 4th-6th 2011, University of Bath, UK*

Co-author conference papers:

1. Y He, W Wang, **G Sze**, G Qiao, Da-Wei Gu and B Bramer, Preliminary study of a Cole-Cole model curve fitting method for Electrical Impedance Tomography. *13th International Conference on Electrical Bioimpedance and the 8th Conference on Electrical Impedance Tomography ICEBI 2007, August 29th - September 2nd 2007, Graz, Austria*
2. W Wang, L Wang, Tao Huang, B. Tunstall, D-W Gu and **G Sze**, Parametric image: a step forward for virtual biopsy by EIT? *13th International Conference on Electrical Bioimpedance and the 8th Conference on Electrical Impedance Tomography ICEBI 2007, August 29th - September 2nd 2007, Graz, Austria*
3. G Qiao, W Wang, **G Sze**, W Hussain, L Wang and M Al-Akaidi, Investigation of in-vitro bioimpedance test system for mouse pancreas. *9th 2008 Electrical Impedance Tomography Conference, June 16th - 18th 2008, Hanover, USA*

4. N Béqo, **G Sze**, N Huber and W Wang, The flexible and configurable Sussex EIM MK4 using PCI eXtensions for Instrumentation (PXI). *Journal of Physics: Conference Series 224 (2010)*
5. N Béqo, **G Sze**, B Tunstall, G Qiao, A Zarafshani and W Wang, A flexible and configurable hardware for the combined EIM and Ultrasound device. *Journal of Physics: Conference Series 224 (2010)*
6. N Huber, N Beqo, C Adams, **G Sze**, B Tunstall, G Qiao, and W Wang, Further investigation of a contactless patient-electrode interface of an Electrical Impedance Mammography system. *Journal of Physics: Conference Series 224 (2010)*
7. A Zarafshani, N Huber, N Béqo, B Tunstall, **G Sze**, C Chatwin and Wei Wang, A flexible low-cost, high-precision, single interface electrical impedance tomography system for breast cancer detection using FPGA. *Journal of Physics: Conference Series 224 (2010)*
8. N Béqo, B Lingham, C Lobstein-Adams, **G Sze** and W Wang, Dual scans with Combined Ultrasound and Electrical Impedance Mammography. *12th* International *Conference in Electrical Impedance Tomography EIT 2011, May 4th-6th 2011, University of Bath, UK*

Oral presentations on conferences:

1. Image Reconstruction for 3D Electrical Impedance Mammography. *10th* International *Conference on Electrical Bioimpedance, April 4th - 8th 2010, Florida, USA*
2. Preliminary study of conductivity changes of planar electrode system of Sussex Mk4 Electrical Impedance Mammography. *12th International* Conference *in Electrical Impedance Tomography EIT 2011, May 4th-6th 2011, University of Bath, UK*

First author journal papers:

1. **G Sze**, W Wang, G Qiao and D C Barber, Preliminary results of the Sussex Electrical Impedance Mammography planar electrode array system. *Submitted to Physiological Measurement*
2. **G Sze**, W Wang, Image reconstruction and regularization methods in 3D electrical impedance mammography. *Submitted to Physiological Measurement*

Co-author journal papers:

1. G Qiao, L Wang, **G Sze**, N Beqo, B Tunstall, C Chatwin and W Wang, Investigation of a compact *in-vitro* bio-impedance measurement system. *Asian Journal of Physics Vol. 19, No. 1 (2010) 79-86*

LIST OF TABLES

LIST OF FIGURES

ABBREVIATIONS

3D:	Three dimensional
ACT:	Adaptive Current Tomography
AC:	Alternating Current
APT:	Applied Potential Tomography
CT:	Computed Tomography
CRP:	Combined Ring-Planar
DAQ:	Data Acquisition
DBT:	Digital Breast Tomosynthesis
DC:	Direct Current
EIM:	Electrical Impedance Mammography
EIT:	Electrical Impedance Tomography
EITS:	Electrical Impedance Tomography Spectroscopic
ERT:	Electrical Resistance Tomography
FDA:	Food and Drug Administration
fdEIT:	frequency-difference Electrical Impedance Tomography
FFT:	Fast Fourier Transform
FWHW:	Full Width Half Maximum
GCV:	Generalised Cross Validation
HMHA:	Half Maximum Height Area
LCM:	Linear Correlation Measure
MIT:	Magnetic Induction Tomography
MNR:	Modified Newton Raphson
MRI:	Magnetic Resonance Imaging
MUX:	Multiplexer

NI:	National Instrument
NOSER:	Newton One-Step Error Reconstruction
OT:	Optical Tomography
PC:	Personal Computer
PET:	Positron Emission Tomography
POS:	Positivity Constraint
RDF:	Ratio Difference Frequency
SNR:	Signal to Noise Ratio
URT:	Ultrasound Reflection Tomography

MATHEMATICAL SYMBOLS

c, σ:	Conductivity
I:	Current
J:	Current density
F:	Electric field
$\emptyset$, ψ:	Electric potential
I:	Identity matrix
l:	Length
g:	Potential different
s:	Region on the boundary
λ , α :	Regularization parameter
R:	Resistance
S, B, F:	Sensitivity Matrix
V:	Voltage
Ω:	Volume

CHAPTER 1 INTRODUCTION

This thesis describes the original research in application of a medical imaging technique known as Electrical Impedance Tomography (EIT) on breast cancer detection, which shall be named hereto as Electrical Impedance Mammography (EIM).

I will present the basis and principles for EIT, followed by a discussion on current different mammography techniques in comparison to EIM. The status of development for the technology behind EIM and technical challenges will also be reviewed.

The aims and objectives of this research will be presented followed by an outline structure of this thesis.

1.1 Electrical Impedance Tomography (EIT)

Electrical Impedance Tomography (EIT) is a medical imaging technique that aims to create medical images of the human body by means of external scanning. Like magnetic resonance imaging (MRI) and ultrasound scanning, it is a non-invasive imaging technology. Similar to magnetic induction tomography (MIT) (Griffiths, 2001), it measures changes in electromagnetic phenomena.

Electrical Impedance refers to the measurement in real and imaginary units (Barber, 2000). Admittivity images can be constructed using measurements in surface impedance.

The most widely adopted EIT measurement method is the “four-electrodes” method, which utilizes two electrodes on the object surface as a source of injecting small alternating current (AC) generating an electric field, and two electrodes on the object surface as a voltage recorder, which measures the differences in electric potential.

Apart from measuring signal magnitude, the phase angle difference between the injecting current and recorded voltage may also be captured as the impedance

phase difference. This polar form of impedance can be directly converted into Cartesian form for reconstructing admittivity images.

When phase angle information is absent, reactance is deemed to be zero. As such, it becomes a measurement for resistance rather than impedance. Under such circumstances the reconstructed images are actually conductivity images, as opposed to admittivity images, as there is no information on permittivity. The technique of measuring resistance alone is known as Electrical Resistance Tomography (ERT), which is also a geophysical technique for imaging subsurface materials.

The term "tomography" refers to the reconstruction of internal distribution from multiple external viewpoints (Scott *et al.*, 2005), thus providing a cross-sectional slice image through an object. The term originates from the Greek words tomos (slice) and graph (image). EIT, however, is different from traditional tomography as electric field changes actually reflect conductivity changes in a three dimensional domain. This is because, as we know, low-frequency electrical current cannot be confined to a two-dimensional plane (Bayford, 2006).

Therefore, when designing an EIT system, we can either simplify the mathematics for reconstruction to allow for artefacts in the images, or we aim to improve the accuracy of the reconstructed images by building a three-dimensional conductivity model.

EIT uses the differences in electrical conductivity of different body tissues to reproduce images of conductivity distribution within a certain part of the body. It has the advantages of being a non-invasive and relatively low cost method. The utilization of the bio-impedance characteristics in living tissues to aid disease diagnosis was a novel subject. Initially it was called Applied Potential Tomography (APT) until 1986 when the term Electrical Impedance Tomography (EIT) was coined in a meeting in Sheffield.

Both the first published images (Barber *et al.*, 1983) and the first clinical system known as the Sheffield Mark 1 system (Barber *et al.*, 1987) came from the Sheffield research group. In 1996, the same research group published the first 3D EIT images (Metherall *et al.*, 1996), which were multiple slices of chest images reconstructed from data collected by multiple-ring electrode system.

EIT has been applied in scanning different body parts, including the brain (Holder, 1992), breasts (Ybarra *et al.*; Jossinet, 1988; Wang *et al.*, 2001; Cherepenin *et al.*, 2002; Laszlo *et al.*, 2007; Stoneman *et al.*, 2007; E. K. Murphy *et al.*, 2010), the heart (Li, 1996) and lung (Brown *et al.*, 1995). It has also been used to measure physiological parameters like cerebral haemodynamics (Holder, 1992), pulmonary ventilation (Frerichs *et al.*, 1999; Kuen, 2009; Hahn *et al.*, 2010), and total body water and body fat (Henry *et al.*, 1985). Furthermore, it has been used in monitoring apnea, fracture healing, gastrointestinal emptying, hyperthermia; it has also been used in bladder volume measurement and in limb plethysmography (Webster, 1990), as well as in detection of pulmonary emboli (Metherall *et al.*, 1996).

1.2 Electrical Impedance Mammography (EIM)

The current established method for breast cancer screening is X-ray mammography. During examination, a low dose X-ray is passed through a breast, which has been stabilized by compression in between a pair of parallel glass panels to ensure that all breast tissue is viewed.

If cancer tissue is suspected, a further diagnostic procedure and definitive tissue typing will need to be done by collecting a tissue sample, via needle aspiration or tissue biopsy, from the suspicious lesion.

The tissue typing of the suspicious lesion may sometimes be aided by other imaging technologies such as X-ray Computed Tomography (CT), Magnetic Resonance Imaging (MRI) or Ultrasound. These techniques can also provide information on the location and staging of the cancer.

As such, the current breast cancer screening method can sometimes be invasive, and it can become relatively expensive, not to mention the physical discomfort and pain the patient experience during the process.

Digital Tomosynthesis (Dobbins, 2009; Tingberg, 2010) is a modified technique based on X-ray CT, and when it is applied to breast cancer scanning it is known as Digital Breast Tomosynthesis (DBT) (Wu *et al.*, 2003; Smith, 2008; Gennaro *et al.*, 2010).

The major advantages of this method include the use of lower dose X-ray, the avoidance of overlapping between normal-dense region and cancerous tissues on traditional 2D imaging, the use of cone beams instead of full beam rotations, and the lesser compression on the breast. DBT systems such as the Selenia Dimensions Tomosynthesis System (Bertolini *et al.*, 2011) have been approved by the U.S. Food and Drug Administration (FDA) as a medical diagnostic system, although more clinical results are necessary to attract more clients. Nevertheless, this technique is still relatively invasive and expensive, and it can only do single spectrum analysis.

EIM examines breast cancer in-vivo using the EIT technology. In principle, EIM has the advantage in multiple parameters spectrum analysis by using the Cole-Cole theory (Cole *et al.*, 1941; Foster *et al.*, 1989). The di-electric properties between normal and cancerous breast tissues show significant difference from in-vitro experiments (Surowiec *et al.*, 1988; A. M. Campbell *et al.*, 1992; Tunstall *et al.*, 1997; Jossinet, 1998; Chauveau *et al.*, 1999; Sha *et al.*, 2002).

Applying EIT on human breast has several additional advantages. Firstly, EIM is totally non-invasive, and it will not induce any discomfort or fear. It also provides a possible solution for regular clinical screening assessment without causing any harm to the human body.

Image reconstruction algorithm such as back-projection (Barber *et al.*, 1987) offers rapid answers that even when used on an ordinary computer, the reconstruction can be completed in the order of milli-seconds. As such EIM can be developed as a real-time monitoring unit. Besides, diagnosis will be based on in-vivo measurement and biopsy may not be necessary, so that both physical pain and discomfort can be avoided.

Lastly, EIM instrument is relatively low cost and could be manufactured in as a compact size clinical instrument and it shall be easily fitted in a doctor's surgery. Theoretically it can detect early stage breast cancer and it would be able to identify different types of abnormal tissues. Compared to X-ray, biopsy, CT, MRI, ultrasound and DBT, EIM is a safe, quick and inexpensive method.

1.3 Various EIM System

1.3.1 The Israel research group

The earliest commercialized EIM instrument was developed in Israel in 1990 (Piperno *et al.*, 1990) and it was later named as T-SCAN™ technology TS2000 system (Assenheimer *et al.*, 2001). It was manufactured by TransScan and distributed by the Siemens Medical Systems, Inc. in 2000. In the first clinical trial, 58 women have been examined (Malich *et al.*, 2000). Results showed that, the detecting depth of this system cannot be too far from the electrode plane, and the depth is limited to 3cm to 3.5cm. Besides, the system cannot detect lesions behind the nipple because of the "bright white spot" at the nipples, caused by decreased impedance of the nipple tissues. As such its ability to detect malignant tissues behind the nipples was significantly impaired because of the overlapping conductivity changes from the nipples creating a detection blind spot.

1.3.2 The Moscow research group

Another commercial system was developed by the Moscow research group who patented their EIM system in 1999 (Cherepenin *et al.*, 2000) and they published two sets of clinical results in 2001 and 2002 respectively (Cherepenin *et al.*, 2001; Cherepenin *et al.*, 2002).

Using the first set of results, and comparing EIM to traditional X-ray mammography, the researchers concluded that EIM is capable to detect breast cancer tissues by analysis of single frequency static images. This is based on the fact that abnormal cancerous tissues have higher conductivity. However this method of analysis is limited by the different conductivity in nipple tissues and the denser breasts in young woman.

The second group of results (in 2002) showed that the conductivity of mammary glands in healthy women actually changes with the menstrual cycle, as well as with lactation and menopause. It is believed that these physiological events affect the background conductivity of the breast.

Later Campbell published more patient data collected from Czech Republic, Italy and Malaysia of different age groups on the European Community (EC) certificated version, 3D EIT medical instrument MEIK in 2007 (J. Campbell *et al.*, 2007). He suggested that the MEIK system could be used to monitor fibrocystic changes regularly without any side effect, but the problem of high conductivity in normal nipple tissues and the lesion being detected still remained as a challenge.

More clinical results were collected by another version named MEM in 2008 (Trokhanova *et al.*, 2008). The objective of the research was on the diagnosis of mastopathy and other non-cancerous diseases of the mammary gland. By comparing the averaged conductivity (by averaging the whole region of visible breast tissue), mastopathy tissues showed a lower averaged conductivity value than normal tissues in both frequencies (10 kHz and 50 kHz). Here to separate the two tissue types becomes difficult as the conductivity range of most normal tissues is actually broader than abnormal tissues. Further research is required to accurately define the border between two.

1.3.3 The Rensselaer Polytechnic Institute research group

The Rensselaer Polytechnic Institute research group customized the 4th generation of Adaptive Current Tomography (ACT) system as Electrical Impedance Spectroscopy System (Saulnier *et al.*, 2007) for breast cancer detection. The ACT system uses adaptive method of data collection (Gisser *et al.*, 1987), also named as optimal current method. It injects currents simultaneously through all electrodes and the voltages on each electrode are measured. The power to distinguish between different tissue types can be increased as the number of electrodes increases. Moreover, the ACT4 EIT system uses planar radiolucent electrodes to register EIT images with X-ray images, and it produces dual images using the two different modalities that doubly confirm the existence of abnormal tissue.

Preliminary results (Kao *et al.*, 2008) showed the ability to distinguish normal from abnormal tissues. From the four presented static frequency images, two malignant cases were identified clearly by using the Linear Correlation Measure (LCM) method. However, more case studies are required to verify the results,

particularly to analyse if the LCM method could distinguish between normal and benign tissues.

The above systems use planar electrode array system, with evenly distributed sensors in a direction parallel to the electrode plane (except when it is at the periphery of the plane). The further it is from the current injecting electrodes, the weaker the sensitivity. The sensitivity also decreases as the depth from electrode plane increases.

1.3.4 The Dartmouth research group

The Dartmouth research group developed the Electrical Impedance Tomography Spectroscopic (EITS) imaging system (Hartov *et al.*, 2000) using circular electrode array design. The EITS system supports broad range of frequencies (10 kHz to 1 MHz) and generates both conductivity and permittivity distributions. The *in* vivo results (Osterman *et al.*, 2000) were encouraging that homogeneous absolute conductivity and permittivity images could be shown for all normal cases. However the average values of both conductivity and permittivity has large variation and the central 60% of the image was disturbed by electrode artefacts created by the shunting effect (Hua *et al.*, 1993) associated with finite size electrodes or the electrode/gel/skin contact impedance.

Kerner published clinical imaging results in 2002 (Kerner *et al.*, 2002) based on a modified platform that improved the contact between electrodes and skin so that accuracy was increased in repeated test. A breast model simulation study by the De Montfort group (Wang *et al.*, 2001) showed similar results. It was shown that tumours are most easily distinguished both visually and numerically at frequencies above 500 kHz, and noise would be degraded less at higher frequency images. One important finding is that normal breasts usually produce smooth images, while malignancies tend to have inhomogeneous images.

Soni published more clinical results (Soni *et al.*, 2004) acquired by the same system. It was found that permittivity images seems to be a better visual tool for distinguishing abnormal from normal breasts. The EITS system has been modified (Halter *et al.*, 2008) with an increase in the range of frequency from 10 kHz to 10 MHz. At this frequency range the signal to noise ratio (SNR) can be increased to a

more decent level (94 up to 2 MHz, 65 at 10 MHz). 96 women were examined using this system, and they were categorized into four groups according to the breast tissue density. The resulting conductivity images did match the tissue density report.

1.3.5 The Duke University research group

For one ring of planar electrode array can only reconstruct image in one layer of 2D plane, the Duke University research group modified the 2D circular electrode array system and developed a 3D EIM system (Ye *et al.*, 2006; Ye *et al.*, 2008) by combining multiple circular arrays into cone shape. A high resistivity cylindrical object and a round tumour phantom have used in the measurement. During measurement, the tumour phantom was soaked in conductive fluid. The system was designed to inject currents that pass through the objects inside the cone shape measurement tank, thus the two current injecting electrodes may locate in different planes of electrodes. Both the cylindrical object and the tumour phantom were successfully reconstructed in the expected depths in the 3D reconstruction.

1.4 The Problems

The diagnostic capability of current EIM systems is mainly limited by the performance of the systems, electrical artefacts, and the density of various tissues. These are the current challenges in diagnosing breast cancer using EIM.

As the use of dielectric properties is a unique characteristic of EIT, it is difficult to obtain this physiological information by other imaging modalities. The major challenges limiting the diagnostic capability should be tackled first, whilst other factors such as speed and spatial resolution can be improved later. Diagnosis capability is underpinned by four basic factors: *sensitivity*, *repeatability*, *reliability* and *accuracy*:

1.4.1 Sensitivity

Sensitivity depends on system design. It measures how well the electrodes can sense the changes inside the boundary of measurement. Factors such as distance between electrode and object, current drive and voltage receive pattern, or injecting current amplitude can vary sensitivity. Usually simulation study is carried out before manufacturing an EIT system. Simulation involves heavy theoretical studies to justify how well the EIT system could be, and sensitivity is one of the major items in it. In the theoretical studies, mathematical techniques such as modelling, finite element and forward method are used to generate simulated measurement data, thus design the best electrode configuration for the target application. Those mathematic skills are the physical knowledge of electrical and magnetism that applied to EIT. Image reconstruction may follow after generating the simulated measurement data. Images could be analysed to verify if the system could produce the images containing sufficient information for the use.

1.4.2 Repeatability

Repeatability is directly related to the random noise induced by the system. Early studies (Brown *et al.*, 1987) showed that for any electrical impedance measuring device, a maximally allowed background electrical noise should be determined. For example, a 16 electrode rings electrode array EIT system should have a maximum of 0.1% noise (equivalent to 60 dB signal to noise ratio) in order to pick up impedance changes in human lungs and ventricles.

Human breasts are relatively simple structures anatomically, without any bone, air or any major blood vessels. However, from the EIM studies of the Dartmouth group and the Moscow group, we know that the density of the adipose tissue and mammary gland status in different phases of the menstrual cycle can have a significant effect on the conductivity in the breast. This variation of breast tissue conductivity creates a challenge in breast imaging.

To tackle the problem of this variable physiologic signal range, we can selectively use higher voltage signals, thus decreasing the impact created by the variable dynamic signal range. As such, even the noise due to electrical component (e.g. stray capacitance) will be reduced as all signal sizes have been increased.

Another system noise may come from the shunting effect associated with finite size electrodes or the contact impedance between electrode and the medium such as skin or gel. Preliminary study (Wang *et al.*, 2007) shows that wet electrode may be a possible solution to reduce the contact impedance problem.

1.4.3 Reliability

Reliability is also important as all image reconstruction algorithms require the solution of a forward problem (Barber *et al.*, 1988), accurate information about the electrode positions and boundary of the body surface is very important. Any incompatible information from electrode positions to the body surface boundary can cause mismatching between real and simulated data (Tang *et al.*, 2002a). We can use image reconstruction algorithm that does not require forward solution, such as Back-Project method (Barber *et al.*, 1984), or alternatively, we can modify the hardware system such that body boundary and electrode positions can be accurately measured.

Imaging technology can either be “local” or “non-local”. X-ray CT is “local” as one straight X-ray beam is passed through the body, which forms a pixel of the image. The value of this pixel is only dependent on the material that lies in the path of this beam. By using multiple angles of measurement, the captured 2D slices could be reconstructed to produce a 3D view of the scanned object.

Technologies with this “local” property are categorized as “hard-field” tomography. Other imaging technologies that are “local” or “hard-field” include Magnetic Resonance Imaging (MRI) and Positron emission tomography (PET).

EIT is classified as a “non-local” or “soft-field” tomography, which means that any points in the scanned object can affect measurement results. Other “non-local” or “soft-field” tomography techniques include Ultrasound Reflection Tomography (URT) and Optical Tomography (OT) (Horesh, 2005).

All “soft-field” techniques face a similar challenge. The reconstruction calculation is relatively ill-conditioned, as the conductivity image does not have a linear relationship with body surface voltage measurement. Because of this “ill-posed” problem, even increasing the number of measurement could only marginally enhance the image quality.

Furthermore, it means that a small error of collected data can significantly affect the resultant image. That is why accurate information about the electrode position and body surface boundary is of paramount importance. Therefore, finding an appropriate number of measurements with a suitable number of image pixels would be much better than blindly increase the number of measurement in order to enhance the spatial resolution.

We have to solve the "non-local" inverse problems carefully, and this "non-local" property of EIT (Lionheart, 2004) can result in a limited spatial resolution.

In solving this "non-local", ill-posed problem, a priori information (Avis *et al.*, 1995; M. Vauhkonen *et al.*, 1998; Bayford, 2006) plays an important role in calculating the forward model and regularization of the inverse calculation.

Some investigations have been done recently to enhance the accuracy of forward model such as complete electrode model for EIM geometry (Kim *et al.*, 2007) and forward model of breast (Kulkarni, 2008), in which they calculate a closer forward solution to the physical measurement by using an accurate electrode size, electrode position or breast shape.

Regularisation is another important technique in solving ill-posed problem. This technique has been applied in solving electrical impedance inverse calculation (Breckon *et al.*, 1987). Regularisation means providing constrains in the calculation of the solution by applying certain criteria to avoid wrongly diverged answers. Solution can then become more reliable and trustworthy. As a trade-off, some information from the measurement may have to be discarded.

1.4.4 Accuracy

Accuracy in true positive for diagnosing cancerous tissue is related to the method in identifying different types of tissues. To identify specific tissue types, we need to answer a series of questions, for example, how to define what normal is and abnormal, how to define the range of parameters, and how to categorize so many different abnormal cases, etc.

In different measuring situations, e.g. breasts with different adipose tissue densities and different water content, EIM images become more difficult to be normalized. Also measurements using different frequencies have to be normalized differently as well.

We need to arrange good clinical trials as this is essential to determine these parameters. The more the number of good quality samples, the better the definition of such parameters.

A method using multiple frequencies analysis faces difficulty in extracting parametric imaging, as absolute conductivity reconstruction can be affected by non-linear measurement problems such as stray capacitance changes through frequencies.

The Kyung Hee University research group found an alternative method fdEIT (Harrach *et al.*, 2010). It does cross frequency analysis by differentiating data before image reconstruction to avoid the enlarging any error.

Furthermore, the use of phantom may be effective in such case and real clinical data should be urgently needed (Boone *et al.*, 1997) for the maturity stage of EIM system development.

1.5 Research aim and objectives

The aim of this thesis is to present the developed imaging and analysing techniques for the Sussex Mk4 EIM system and for the purpose of improving the sensitivity to detect abnormal breast tissue.

The thesis has the following objectives:

1. To investigate on the functionality of the Sussex Mk4 EIM system
2. To develop the image reconstruction and regularization methods for data acquired from system using planar electrode configuration
3. To investigate on electrode configurations of EIM system based on sensitivity analysis

1.6 Thesis organisation

The next chapter begins with the introduction of the biomedical engineering research group in Sussex and its developed EIM systems. The mathematical model and basic theories of EIT are presented. Two common electrode configurations of EIT systems are then introduced, and lastly the image reconstruction algorithms.

In Chapter 3, the Sussex 3D electrical impedance mammography Mk4 system will be introduced, which is designed for detecting breast cancer by using planar electrode array system. The characteristics of the system are on the localized drive and receive pattern that reduces noise level, and also the rotatory drive pattern to narrow the possible solution of inverse calculation. Simulated result is presented to analyse the performance of the system.

In Chapter 4, the method in modifying image reconstruction algorithm for processing clinical breast data will be the mainly focused task. Image reconstruction algorithm can be customised by a priori information that is acquired from the system such as signal to noise level and expected conductivity distribution of object. Simulated experiment results are presented to support the modified algorithm.

Chapter 5 will be focused on an investigation of a combined ring and planar electrode model of 3D EIM system. This system is designed to solve the weak sensitivity problem found from the Sussex EIM Mk4 system. Sensitivity analysis and reconstruction results will be presented.

In the final chapter, the conclusion will be given together with the suggested future research.

CHAPTER 2 PROJECT BACKGROUND

This chapter addresses the background theories underlying the techniques that are applied to the Sussex EIM Mk4 system. In Section 2.1 I will give an overview of Sussex EIM Mk4 system. Section 2.2 will illustrate the mathematical model and the traditional EIT electrode configuration. The image reconstruction algorithms will be discussed in section 2.3, and finally a brief summary of this Chapter in Section 2.4.

2.1 Overview of the Sussex EIM Mk4 system

The Sussex Biomedical Engineering Research Group (formerly Biomedical Engineering Research Group of the De Montfort) started its EIM research studies in 1996. The De Montfort Mk3 EIM system (Wang *et al.*, 2001) was first developed for breast imaging since 1996 using a ring electrode configuration of EIT. In the year 2003, new research on planar electrode array system was started in order to enhance the sensitivity in detecting breast cancer in 3D. The instrument that was developed following this new research was named "Sussex Mk4 EIM system". There were 5 stages in the development of this new system.

2.1.1 Theoretical Studies

In this initial stage, mathematical studies were carried out, which covered electrode configuration, human breast modelling, sensitivity analysis, finite element method (FEM), 3D mesh generation and image reconstruction algorithm. Results were then simulated, which was the prerequisite for moving onto hardware design and manufacture. Based on the its predecessor the De Montfort Mk3 EIM system, major modifications were made on electrode configuration, and the drive and receive patterns for the electrode pairs. Preliminary results has proven the possibility in detecting breast cancer tissue in-vivo by using this newly proposed EIM system.

2.1.2 System Design, Signal Calibration and Manufacturing

Figure 2.1 shows the hardware set up of the Mk4 System. Note that components could be replaced by other model from time to time, as the performance and price are concerned. The arrows show the flow of the input/output signals.

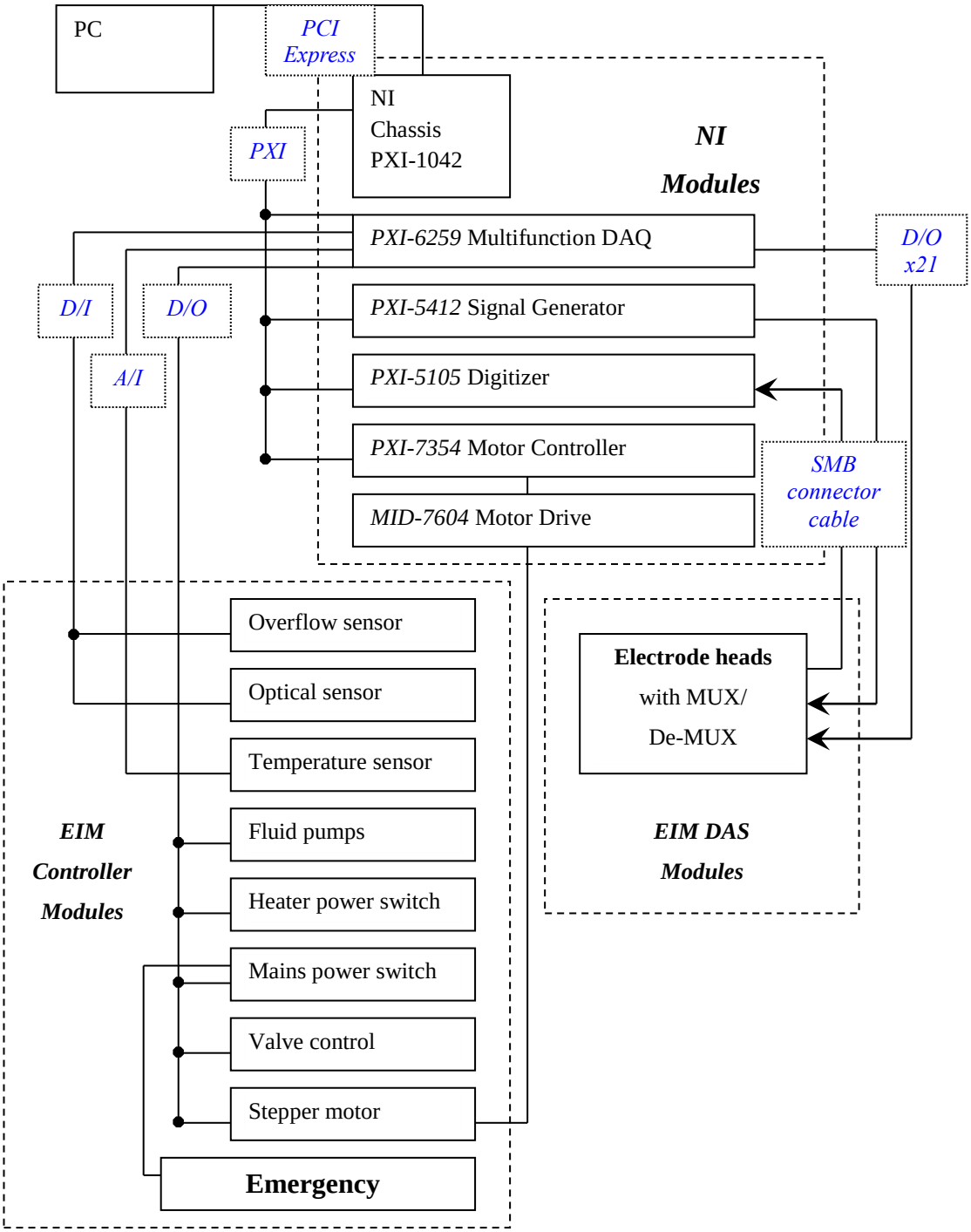

Figure 2.1 *Hardware set up for the Mk4 EIM system*

The latest version of Mk4 system is based on National Instruments' (NI) system consists of a signal generator as source and digitizers to receive output signal. These devices provide higher accuracy for clinical application. The acquired signals must be clean and stable, as such it will be capable to provide good digital resolution. This is particularly important for high speed real-time data acquisition. The Sussex EIM Mk4 system is designed to be compatible to a wide range of loadings

(conductivity) from different breast sizes and architecture. It can also utilize different frequencies for multiple frequency analysis.

The multifunction DAQ device for digital data acquisition is based on NI. It is designed to send digital signal to the multiplexer (MUX) for switching on or off the electrodes. In such the 85 electrodes on the scan-head can be rapidly controlled by computer program.

Signal calibration is essential. It filters signal noise that is generated from the electronic components. It also balances the readings between the electrodes. The signals can be affected by noises in other frequencies, as such Fast Fourier Transform (FFT) has been applied in the Sussex EIM Mk4 system. It extracts the magnitude and phase angle difference of impedance in different frequencies. The magnitude and phase angle differences are arranged as two arrays of numbers corresponding to each measurement by a combination of drive and receive electrodes.

We use two different methods for filtering signal noise. The first method involves cross-checking reciprocal measurements. Reciprocal measurements can be obtained either by inverting the driving pair and the receiving pair of electrodes, or by changing the driving and receiving electrodes to a mirrored position. Reciprocal measurements should be the same as the original measurements. If there is a discrepancy, it means there is a difference in the performance of electrodes concerned. As such it is necessary to calibrate the hardware. The second method we use for signal noise filtering is by comparing real and simulated measurements. If there is a discrepancy linear to changes in frequency and loading, then signal processing can help the calibration and improves accuracy. However, if the discrepancies appear in a non-linear relationship to frequency and loading changes, then further hardware calibration is necessary.

Several mechanical components were integrated into the Sussex EIM Mk4 system. There is a temperature control system that keeping saline in body temperature and saline is the media between body and electrodes. A pumping system has been integrated for pumping saline and disinfectant through measurement tank into the wash tank. Depth of the scan head is adjustable and being controlled by stepping motors. The signals for the stepping motors are sending from the computer

through the COM port. Sensors are using as safety devices to detect the position of the scan head and saline levels such that all parts could be physically stopped by pressing the emergency button.

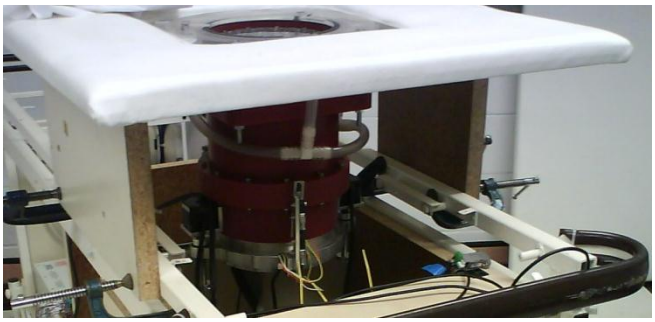

Figure 2.2 *Measurement tank (red) inside the trolley*

2.1.3 Image Reconstruction

Two conventional image reconstruction methods were adapted from the De Montfort EIM Mk3 system to the Sussex EIM Mk4 system, which are the Back-Projection (Barber *et al.*, 1983) and the Newton-Raphson based (Yorkey *et al.*, 1987) Method. Customized items such as 3D mesh, regularization constraint and multiple frequency reconstruction method were implemented. The basic theories of image reconstruction algorithms were introduced in section 2.3 and the research on image reconstruction algorithm has been written in chapter 4.

2.1.4 Image Analysis

Since 1997, the Sussex Biomedical Engineering Research group started *in-vitro* studies on human breast tissues dielectric properties by using the Hewlett-Packard impedance analyzer 4194A (figure 2.3). The di-electric properties that derived from *in-vitro* measurement enable the possibility in distinguishing normal and abnormal tissues from *in-vivo* measurement. Thus, the characteristics of cancerous tissue could be derived by using the database of breast tissue di-electric properties instead of purely empirical analysis. This could reduce the number of clinical trials and enhance persuasiveness. Human breast tissue properties, 3D breast modelling and the basic EIT image analysis techniques were discussed in section 2.4, while a novel image analysis method has been written in chapter 5.

Figure 2.3 *HP impedance analyzer 4194A*

2.1.5 Clinical Trial

Indeed EIT has been advanced to the point where clinical trials can be implemented since late 90's (Boone *et al.*, 1997). Clinical trials have been inducted by the Sussex Biomedical Engineering Research group in Leicester in 2000 by using the Mk2 system (Wang *et al.*, 1998), then, Wuhan, China in 2004 by using the Mk3 system, and finally in UK since 2009 until present by using the Mk4 system. Details analysis of the UK clinical trial data could be found in chapter 5.

2.2 Mathematical model

2.2.1 Fundamentals

EIT calculates the admittivity changes within a closed volume by using surface impedance measurement. This calculation between volumetric data and surface measurement data could be derived from the Ohm's law $V = IR$ (Duffin, 1990) which describes the voltage V measured across a resistor with constant resistance R and current I going through it. It could be written into a more general differential form applying to a point as

$$-\mathrm{d}V = R \cdot \mathrm{d}I \tag{2.1}$$

Convert R into conductivity σ, length l and area A,

$$-\mathrm{d}V = (\mathrm{d}l/\sigma \mathrm{d}A) \cdot \mathrm{d}I \tag{2.2}$$

Voltage is negative because potential falls along the direction of positive current flow. Exchanges the positions of the terms,

$$\mathrm{d}I/\mathrm{d}A = -\sigma \cdot \mathrm{d}V/\mathrm{d}l \tag{2.3}$$

For a continuous conductive medium, current density J = dI/dA, and gradient of potential $\boldsymbol{\nabla}\emptyset$ = dV/dl. The Ohm's law for conduction could be rewritten as

$$\boldsymbol{J} = -\sigma \boldsymbol{\nabla}\emptyset \tag{2.4}$$

For a four-electrodes EIT measurement, because a steady current source is flowing in and out of the conductive medium as a closed body Ω, and there is no other current sources inside the body, the divergence of current density is equal to zero,

$$\boldsymbol{\nabla} \cdot \boldsymbol{J} = 0 \tag{2.5}$$

Thus combining with equation (2.4) we have the continuum Kirchoff's law

$$\boldsymbol{\nabla} \cdot (\sigma \boldsymbol{\nabla}\emptyset) = 0 \qquad \text{in a closed body } \Omega \tag{2.6}$$

with the Dirichlet boundary conditions that electric potential ∅ on the boundary $\partial\Omega$ equals to the voltage distribution v_i under electrode i,

$$\emptyset|_{\partial\Omega} = v_i \qquad \text{under electrode } i \tag{2.7}$$

also with the Neumann boundary conditions that current density on boundary equals to j_i under electrode i and zero elsewhere

$$\sigma \boldsymbol{\nabla}\emptyset \cdot \mathrm{n} = \begin{cases} j_i & \text{under electrode } i \\ 0 & \text{elsewhere} \end{cases} \tag{2.8}$$

where n is the outward unit normal to the boundary $\partial\Omega$ of closed body Ω.

In EIT system, the injected current j_i for every electrode is known, such that the Neumann problem could be solved if the conductivity distribution σ could be

pre-defined. Once $\emptyset$ is found, voltage distribution v_i could also be calculated by solving the Dirichlet problem. This is a forward problem, and the relationship between conductivity and voltage measurement (Barber, 2000) could be written in matrix format

$$S_\sigma \sigma = V \tag{2.9}$$

where S_σ is the sensitivity matrix, that is dependent on σ, and V is a vector with finite number of voltage measurement $v_{1\ldots N}$.

In practice, EIT instrument measures voltage V on the boundary of a body and the problem would become the solving of conductivity distribution σ. This is an inverse problem. Because S is dependent on σ, the problem is non-linear and thus increased the difficulties in image reconstruction.

2.2.2 The sensitivity relationship

Equation (2.9) defined the discrete form of sensitivity relationship between conductivity and voltage measurement, and the sensitivity matrix S could be derived by using the Geselowitz's relationship (Geselowitz, 1971).

From equation (2.6), if σ is constant, it becomes Laplace's equation

$$\boldsymbol{\nabla^2} V = 0 \tag{2.10}$$

If σ is not constant, we have

$$\boldsymbol{\nabla} \cdot (\sigma \boldsymbol{\nabla} V) = \boldsymbol{\nabla}\sigma \cdot \boldsymbol{\nabla} V + \sigma \boldsymbol{\nabla^2} V = 0 \tag{2.11}$$

and it becomes Poisson's equation

$$\boldsymbol{\nabla^2} V = -\frac{\boldsymbol{\nabla}\sigma \cdot \boldsymbol{\nabla} V}{\sigma} \tag{2.12}$$

In EIT measurement, a series of potential difference on a surface are measured to calculate the conductivity of a closed volume. The relationship between the measured potential different and the conductivity of the closed volume could be described by the Gauss's divergence theorem: If a closed surface T bounds a volume

Ω, then the surface integral of an outward flux $\boldsymbol{F}$ over T is equal to the volume integral of the divergence of $\boldsymbol{F}$ over Ω

$$\oint_T \boldsymbol{F} \cdot \mathrm{d}\boldsymbol{s} = \int_\Omega \boldsymbol{\nabla} \cdot \boldsymbol{F} \, \mathrm{d}v \tag{2.13}$$

Now substitute the vector field $\boldsymbol{F}$ as $\phi\boldsymbol{\nabla}\psi$, where ϕ is a scalar function and $\boldsymbol{\nabla}\psi$ is a vector field. The equation becomes the Green's first identity

$$\oint_T \phi\boldsymbol{\nabla}\psi \cdot \mathrm{d}\boldsymbol{s} = \int_\Omega \boldsymbol{\nabla} \cdot (\phi\boldsymbol{\nabla}\psi) \, \mathrm{d}v \tag{2.14}$$

expand right hand side

$$\oint_T \phi\boldsymbol{\nabla}\psi \cdot \mathrm{d}\boldsymbol{s} = \int_\Omega \phi\boldsymbol{\nabla} \cdot (\boldsymbol{\nabla}\psi) \, \mathrm{d}v + \int_\Omega \boldsymbol{\nabla}\phi \cdot \boldsymbol{\nabla}\psi \, \mathrm{d}v \tag{2.15}$$

substitute $\boldsymbol{\nabla}\psi$ by $\sigma\boldsymbol{\nabla}\psi$ we have

$$\oint_T \phi \, \sigma\boldsymbol{\nabla}\psi \cdot \mathrm{d}\boldsymbol{s} = \int_\Omega \phi\boldsymbol{\nabla} \cdot (\sigma\boldsymbol{\nabla}\psi) \, \mathrm{d}v + \int_\Omega \sigma\boldsymbol{\nabla}\phi \cdot \boldsymbol{\nabla}\psi \, \mathrm{d}v \tag{2.16}$$

If ψ is taken to be a solution to Poisson's equation within the region then from equation (2.6) the first term on the right hand side is zero so

$$\oint_T \phi \, \sigma\boldsymbol{\nabla}\psi \cdot \mathrm{d}\boldsymbol{s} = \int_\Omega \sigma\boldsymbol{\nabla}\phi \cdot \boldsymbol{\nabla}\psi \, \mathrm{d}v \tag{2.17}$$

The term $\sigma\boldsymbol{\nabla}\psi \cdot \mathrm{d}\boldsymbol{s}$ in the left hand side can actually interpret as $\boldsymbol{J} \cdot \mathrm{d}\boldsymbol{s} = \mathrm{d}I$, it is the current flowing across the boundary of the region at a point on the boundary. So we can take out the magnitude of the current I and write this intergral by

$$I \oint_T \phi \, \beta \mathrm{d}\boldsymbol{s} \tag{2.18}$$

where β is a function defined on the boundary, whose value is 1 for the unit current injecting electrodes and 0 elsewhere.

Let ϕ be also a solution to Poisson's equation and the unit current is applied to the region by the other pair of electrodes. Then the above expression is a measure of the voltage difference between the first two electrodes when a current I is applied to the region between the second pair of electrodes.

If we represent this difference by g_{rd} where r refers to the electrode pair between which the measurement is made (the receive pair) and d refers to the electrode pair through which current is flowing (the drive pair) and we consider unit currents applied throughout we have

$$g_{rd} = \int_{\Omega} \sigma \nabla\phi \cdot \nabla\psi \, \mathrm{d}v \tag{2.19}$$

which is the sensitivity relationship.

In electrical impedance tomography measurement, a set of boundary values g_{rd} is acquired and we are extracting the conductivity distribution σ.

2.2.3 Geselowitz's relationship

Equation (2.19) states the boundary potential measurement from a uniform conductivity volume. It is the sensitivity relationship between a pair of current drive electrodes and a pair of voltage measuring electrodes. When there is perturbation from this uniform conductivity case, we have to develop Geselowitz's relationship. The sensitivity relationship can be expanded relative to uniform conductivity *u* as

$$g_{rd} = \int_{\Omega} \left(\sigma + c_p\right)\left(\nabla\phi_u + \nabla\phi_p\right) \cdot \left(\nabla\psi_u + \nabla\psi_p\right) \mathrm{d}v \tag{2.20}$$

where

σ is the uniform conductivity

c_p is the difference between c and the uniform conductivity such that $c_p = c - \sigma$

$\nabla\phi_u$ is the field associated for the uniform conductivity for the first pair of electrodes

$\nabla\phi_p$ is the additional field component due to c_p for the first pair of electrodes

$\nabla\psi_u$ is the field associated for the uniform conductivity for the second pair of electrodes

$\nabla\psi_p$ is the additional field component due to c_p for the second pair of electrodes

Let us drop the subscript $_{rd}$. Expanding, but retaining for the present $c = \sigma + c_p$, we have

$$g = \int_{\Omega} c\nabla\phi_u \cdot \nabla\psi_u \mathrm{d}v + \int_{\Omega} c\nabla\phi_p \cdot \nabla\psi_u \mathrm{d}v + \int_{\Omega} c\nabla\phi_u \cdot \nabla\psi_p \mathrm{d}v + \int_{\Omega} c\nabla\phi_p \cdot \nabla\psi_p \mathrm{d}v \tag{2.21}$$

We note that, from the previous result of equation (2.16),

$$\oint_T \phi_u \, c\nabla\psi_p \cdot \mathrm{d}\boldsymbol{s} = \int_{\Omega} \phi_u \nabla \cdot (c\nabla\psi_p) \, \mathrm{d}v + \int_{\Omega} c\nabla\phi_p \cdot \nabla\psi_u \, \mathrm{d}v \tag{2.22}$$

From equation (2.11),

$$\nabla \cdot (c\nabla\psi) = \nabla c \cdot \nabla\psi + c\nabla^2\psi = 0 \tag{2.23}$$

Since $\psi = \psi_u + \psi_p$ and $\nabla^2\psi_u = 0$, we have

$$c\nabla^2\psi_p = -\nabla c \cdot \nabla\psi \tag{2.24}$$

Now

$$\begin{aligned} \nabla \cdot (c\nabla\psi_p) &= \nabla c \cdot \nabla\psi_p + c\nabla^2\psi_p \\ &= \nabla c \cdot \nabla\psi_p - \nabla c \cdot \nabla\psi \\ &= \nabla c \cdot \nabla\psi_p - \nabla c \cdot \nabla\psi_u - \nabla c \cdot \nabla\psi_p \\ &= -\nabla c \cdot \nabla\psi_u \end{aligned} \tag{2.25}$$

Substitute this into equation (2.23)

$$\oint_T \phi_u \, c\nabla\psi_p \cdot \mathrm{d}\boldsymbol{s} = -\int_{\Omega} \phi_u \nabla c \cdot \nabla\psi_u \, \mathrm{d}v + \int_{\Omega} c\nabla\phi_p \cdot \nabla\psi_u \, \mathrm{d}v \tag{2.26}$$

The gradient of uniform conductivity is zero, so that $\nabla\sigma = 0$, and $\nabla c = \nabla c_p$, we have

$$\oint_T \phi_u \, c\nabla\psi_p \cdot \mathrm{d}\boldsymbol{s} = -\int_{\Omega} \phi_u \nabla c_p \cdot \nabla\psi_u \, \mathrm{d}v + \int_{\Omega} c\nabla\phi_p \cdot \nabla\psi_u \, \mathrm{d}v \tag{2.27}$$

Now substituting ϕ_u, c_p and ψ_u into equation (2.6)

$$\oint_T \phi_u \, c_p\nabla\psi_u \cdot \mathrm{d}\boldsymbol{s} = \int_{\Omega} \phi_u \nabla \cdot (c_p\nabla\psi_u) \, \mathrm{d}v + \int_{\Omega} c_p\nabla\phi_u \cdot \nabla\psi_u \, \mathrm{d}v \tag{2.28}$$

From equation (2.11)

$$\nabla \cdot (c_p\nabla\psi_u) = \nabla c_p \cdot \nabla\psi_u + c_p\nabla^2\psi_u = 0 \tag{2.29}$$

Since $\nabla^2\psi_u = 0$, equation (2.29) can be written as $\nabla \cdot (c_p \nabla\psi_u) = \nabla c_p \cdot \nabla\psi_u$, equation (2.28) becomes

$$\oint_T \phi_u \, c_p \nabla\psi_u \cdot \mathrm{d}\boldsymbol{s} = \int_\Omega \phi_u \nabla c_p \cdot \nabla\psi_u \, \mathrm{d}v + \int_\Omega c_p \nabla\phi_u \cdot \nabla\psi_u \, \mathrm{d}v \tag{2.30}$$

Adding equations (2.27) and (2.30)

$$\oint_T \phi_u \, c_p \nabla\psi_u \cdot \mathrm{d}\boldsymbol{s} + \oint_T \phi_u \, c \nabla\psi_p \cdot \mathrm{d}\boldsymbol{s} = \int_\Omega c \nabla\phi_p \cdot \nabla\psi_u \, dv + \int_\Omega c_p \nabla\phi_u \cdot \nabla\psi_u \, \mathrm{d}v \tag{2.31}$$

From this, we interpret the terms on the left hand side by the three equations as below. Since $\psi = \psi_u + \psi_p$, we can expand the following term

$$\oint_T \phi c \nabla\psi \cdot \mathrm{d}\boldsymbol{s} = \oint_T \phi c \nabla\psi_u \cdot \mathrm{d}\boldsymbol{s} + \oint_T \phi c \nabla\psi_p \cdot \mathrm{d}\boldsymbol{s} \tag{2.32}$$

From $c = \sigma + c_p$, we can further expand the terms as

$$\oint_T \phi c \nabla\psi \cdot \mathrm{d}\boldsymbol{s} = \oint_T \phi \sigma \nabla\psi_u \cdot \mathrm{d}\boldsymbol{s} + \oint_T \phi c_p \nabla\psi_u \cdot \mathrm{d}\boldsymbol{s} + \oint_T \phi c \nabla\psi_p \cdot \mathrm{d}\boldsymbol{s} \tag{2.33}$$

For the term $\phi c \nabla\psi \cdot \mathrm{d}\boldsymbol{s}$ is the normal current across the boundary after the change to c occurs. The term $\sigma \nabla\psi_u \cdot \mathrm{d}\boldsymbol{s}$ is the current before the change occurs and these two terms are equal since we always use constant current. So we have

$$\oint_T \phi c_p \nabla\psi_u \cdot d\boldsymbol{s} + \oint_T \phi c \nabla\psi_p \cdot \mathrm{d}\boldsymbol{s} = 0 \tag{2.34}$$

Substitute this equation into equation (2.31), the left hand side terms equal to zero,

$$\int_\Omega c \nabla\phi_p \cdot \nabla\psi_u \, \mathrm{d}v = -\int_\Omega c_p \nabla\phi_u \cdot \nabla\psi_u \, \mathrm{d}v \tag{2.35}$$

Using the argument that $\nabla\phi_p \cdot \nabla\psi_u = \nabla\phi_u \cdot \nabla\psi_p$

$$\int_\Omega c \nabla\phi_u \cdot \nabla\psi_p \, \mathrm{d}v = -\int_\Omega c_p \nabla\phi_u \cdot \nabla\psi_u \, \mathrm{d}v \tag{2.36}$$

Now we can go back to equation (2.21) and rewrite it as

$$g = \int_\Omega c \nabla\phi_u \cdot \nabla\psi_u \mathrm{d}v - 2\int_\Omega c_p \nabla\phi_u \cdot \nabla\psi_u \mathrm{d}v + \int_\Omega c \nabla\phi_p \cdot \nabla\psi_p \mathrm{d}v \tag{2.37}$$

As $c = \sigma + c_p$, we rewrite the first term on the right hand side

$$\int_\Omega c\nabla\phi_u \cdot \nabla\psi_u \mathrm{d}v = \int_\Omega \sigma\nabla\phi_u \cdot \nabla\psi_u \mathrm{d}v + \int_\Omega c_p\nabla\phi_u \cdot \nabla\psi_u \mathrm{d}v \tag{2.38}$$

and so

$$g = \int_\Omega \sigma\nabla\phi_u \cdot \nabla\psi_u \mathrm{d}v - \int_\Omega c_p\nabla\phi_u \cdot \nabla\psi_u \mathrm{d}v + \int_\Omega c\nabla\phi_p \cdot \nabla\psi_p \mathrm{d}v \tag{2.39}$$

The change in g is given by

$$g_p = g - g_u \tag{2.40}$$

where g_u the boundary values measured from a uniform conductivity is,

$$g_u = \int_\Omega \sigma\nabla\phi_u \cdot \nabla\psi_u \mathrm{d}v \tag{2.41}$$

and g_p is the change in boundary values due to the conductivity change c_p is,

$$g_p = -\int_\Omega c_p\nabla\phi_u \cdot \nabla\psi_u \mathrm{d}v + \int_\Omega c\nabla\phi_p \cdot \nabla\psi_p \mathrm{d}v \tag{242}$$

Equation (2.41) are the boundary values measured from a uniform conductivity. Equation (2.42) are the changes in boundary values, and there are two terms on the right hand side. The first term is in a form appropriate for reconstruction if it is suitably normalised. The second term is non-linear, it is small if c_p is small and can be ignored so that **linear sensitivity relationship** is obtained.

$$g_p = -\int_\Omega c_p\nabla\phi_u \cdot \nabla\psi_u \mathrm{d}v \tag{2.43}$$

Now consider the second non-linear term, we write

$$\oint_T \phi_p\, c\nabla\psi_p \cdot \mathrm{d}\boldsymbol{s} = \int_\Omega \phi_p\nabla \cdot (c\nabla\psi_p)\, \mathrm{d}v + \int_\Omega c\nabla\phi_p \cdot \nabla\psi_p\, \mathrm{d}v \tag{2.44}$$

We can also write

$$\oint_T \phi_p\, c_p\nabla\psi_u \cdot \mathrm{d}\boldsymbol{s} = \int_\Omega \phi_p\nabla \cdot (c_p\nabla\psi_u)\, \mathrm{d}v + \int_\Omega c_p\nabla\phi_p \cdot \nabla\psi_u\, \mathrm{d}v \tag{2.45}$$

by an argument identical to the above it can be showed that

$$\int_{\Omega} c\nabla\phi_p \cdot \nabla\psi_p \, \mathrm{d}v = -\int_{\Omega} c_p \nabla\phi_u \cdot \nabla\psi_p \, \mathrm{d}v \tag{2.46}$$

Substitute into (2.42) gives

$$g_p = -\int_{\Omega} c_p \nabla\phi_u \cdot \nabla\psi_u \mathrm{d}v - \int_{\Omega} c_p \nabla\phi_u \cdot \nabla\psi_p \, \mathrm{d}v \tag{2.47}$$

and finally

$$g_p = -\int_{\Omega} c_p \nabla\phi_u \cdot \nabla\psi \mathrm{d}v \tag{2.48}$$

which is Geselowitz's reciprocal theorem (Geselowitz, 1971) for the relationship of measured potential difference and conductivity of a closed volume by using the four electrodes measurement method.

2.2.4 EIT electrode configurations

2.2.4.1 Ring electrode configuration

Ring electrode array system is firstly developed by the Sheffield group as clinical instrument (Barber *et al.*, 1983), that cross-sectional conductivity distributions of forearm and chest have been successfully reconstructed by the data collection system. As shown in figure 2.4, electrodes are arranged in equal space on a circular plane. In clinical application, the array of encircling electrodes is usually attached to the region of interest, the position have to be approximated. This positioning error could be the major factor that altering the sensitivity and image spatial resolution Different number of electrodes (Tang *et al.*, 2002b; Wheeler *et al.*, 2002) and different patterns of current injection and voltage measurement (Webster, 1990) can also affect the performance of the system. Most ring electrode systems have 16 or 32 electrodes. For 3D systems multiple rings of electrode would be used and this multiplies the number of electrodes by four or more times. Current injection and voltage measurement pattern define which pair of electrodes applies current and which pair of electrodes measures voltage. For a 16 electrodes system, if current is only applied on adjacent pairs and measure voltage on the other possible adjacent pairs, total 104 (N(N − 3)/2) independent measurements (Barber, 1990) can be made. This measurement pattern was called adjacent method (Brown *et al.*, 1987). To optimize results under different circumstances, other patterns may be applied such as

adaptive (trigonometric) (Isaacson, 1986 ; Gisser *et al.*, 1987), opposite (Hua, 1987), and parallel system (Cook *et al.*, 1994).

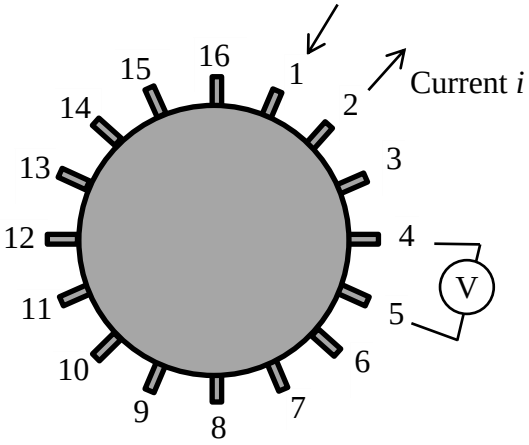

Figure 2.4 *Ring electrode array*

2.2.4.2 Planar Electrode configuration

Electrodes of planar electrode configuration are arranged on the same plane (figure 2.5) instead of a ring. For some region of interest that is difficult to be surrounded by electrode, planar electrode configuration could be an alternative choice. The first experimental result was published by the Sheffield group (Powell *et al.*, 1987) and this technique was named as linear electrode array. The paper was particularly presenting the resolution and sensitivity of planar electrode array. Simulated experimental results showed that the array can detect object close to the surface, but there was a sharp fall of sensitivity against the depth of the object (figure 2.6), and this limit the usefulness of planar electrode array.

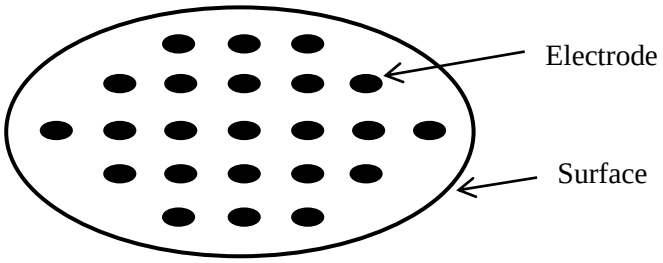

Figure 2.5 *Planar electrode array are implanted below a surface*

On the other hand, the advantages for the application of planar electrode array configuration are listed as below:

1. Electrodes are fixed on a plate and position of electrodes could be accurately known such that the positioning error problem could be avoided.

2. The scan-head is flexible and can readily be moved away from the body of patient, such that the technique could be designed for the use of real time diagnostic scanning.

3. Sensitivity of planar electrodes is comparatively more concentrated than the region encircled by a ring, that resolution could possibly be increased on the local region.

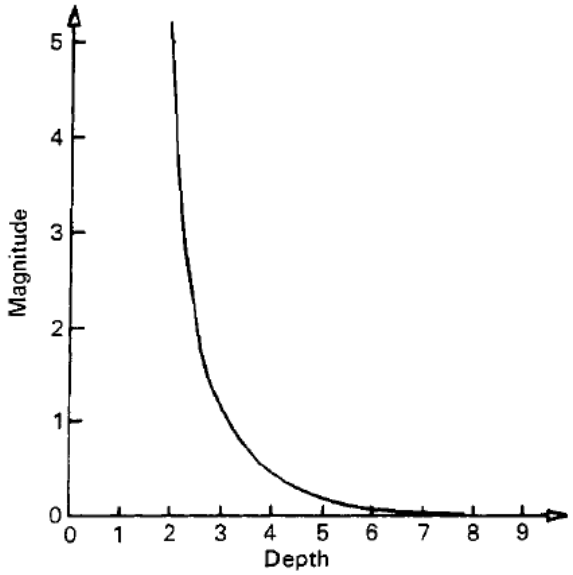

Figure 2.6 *Variation of peak amplitude of image with depth of a point object below the surface (measured in electrode spacing).*

One of the EIT applications using planar electrode array is breast cancer detection (Assenheimer *et al.*, 2001; Cherepenin *et al.*, 2001; Kao *et al.*, 2006). Since the major components of female human breast are the adipose and stroma tissue, they are soft and could be deformed and attached to the plate that implanted with electrode array. It was assumed that the maximum depth of breast tissue is 42 mm for a flattened breast (Hagness, 1998). From the preliminary result of the Sheffield group, the minimum electrode spacing should be around 84mm in order to detect cancerous breast tissue in the deepest depth. However, the results are based on back-project image reconstruction algorithm and a one dimensional array of electrode on a plate, results could be improved with different data acquisition and image

reconstruction approaches. Besides, planar electrode has better resolution in central region comparing with encircled array.

2.3 Image Reconstruction Algorithms

The back-projection and modified Newton-Raphson method have been heavily employed in EIT applications. These two image reconstruction algorithms were introduced in this section:

2.3.1 Back-projection

Back-projection was firstly applied in EIT clinically by the Sheffield group (Barber *et al.*, 1983). It is a linear relationship bases on the assumption of small change in impedance and small change in boundary measurements. In discrete form, the relationship (Barber, 2000) is

$$v = S(c) \tag{2.49}$$

where v is a vector of boundary measurement and c is the vector represents the conductivity distribution of object. Both vectors are related by a forward transformation matrix S, which is the solution to the Poisson's equation:

$$\nabla \cdot (\sigma \nabla \phi) = 0 \tag{2.50}$$

σ is the space-variant conductivity, and ϕ is the distribution of electrical potential with an inhomogeneous conducting medium through which steady current is flowing. Conductivity could be replaced by logarithmic resistivity $R = -\ln \sigma$ and when resistivity is non-uniform equation (2.50) can be approximated as:

$$\nabla^2 \phi_p = \nabla \phi_u \cdot \nabla R \tag{2.51}$$

Here ϕ_u is the uniform potential distribution before change, and ϕ_p is the perturbation from the potential distribution ϕ_u. As ϕ_p is linear to the resistivity R, relationship between change in impedance and change in measurement could be written as equation (2.49). The image reconstruction problem for equation (2.49) appears to find the inverse transformation such that

$$c = S^{-1}(v) \tag{2.52}$$

Base on the derived linear relationship, the inverse matrix could be found by back-projecting the boundary measurement along the equipotential lines (figure 2.7) as presented as:

$$c = B \cdot v \tag{2.53}$$

where B is the back-projection matrix.

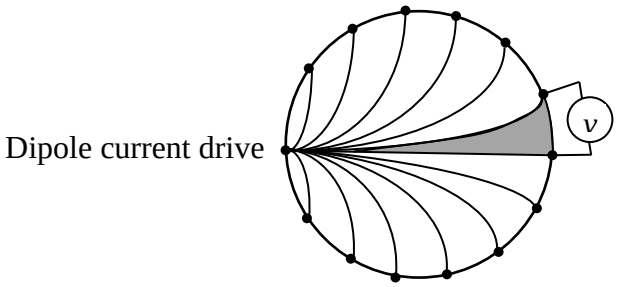

Figure 2.7 *Back-projecting the boundary measurement along the equipotential lines*

The sensitivity of planar electrode array configuration for EIT system was firstly investigated by the Sheffield Group (Powell *et al.*, 1987) with images reconstructed using Back-Projection method. An array of electrodes was arranged linearly in one direction, measuring an object located in different depth. The sensitivity was quantified by using peak conductivity and found to be rapidly decreased with depth of the object from the surface of electrodes. Although peak conductivity dropped significantly with depth, the signature of biological tissue dielectric properties may still exist. The possibility of extracting the dielectric information becomes depending on the level of system noise.

The Sussex EIM Mk4 system has adapted the planar electrode configuration. As current is injecting through a plane of electrodes into the object, the equipotential lines are less dense through the depth (figure 2.8). Unlike ring electrode configuration, planar electrodes are distributed in hexagonal shape on the plane, such that the developed electric field is being considered as a 3D region instead of a 2D layer and accuracy is expected to be increased. Furthermore, electrodes are fixed on the plane, which could avoid the electrode position error problem reported in earlier EIT back-projection studies (Barber *et al.*, 1987; Tang *et al.*, 2002a).

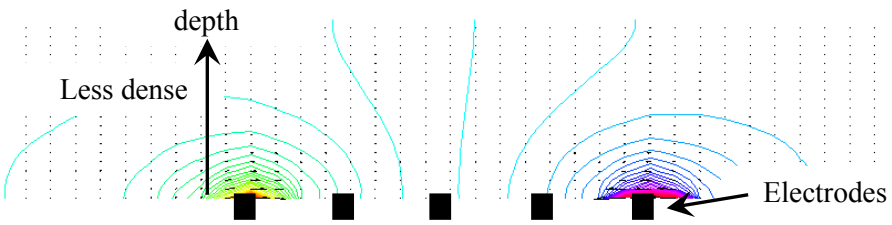

Figure 2.8 *Equipotential lines are less dense through the depth for planar electrode array.*

Another application of back-projection on planar electrode array system was the 3D EIT system that developed for breast cancer detection by the Moscow group (Cherepenin *et al.*, 2001; Cherepenin *et al.*, 2002). They used weighted back-projection along equipotential surfaces of the electric field to reconstruction 3D static frequency images. Images are reconstructed by slices that parallel to the plane of electrode array, and some promising results are produced for detecting breast malignancies. In our study, Back-Projection method has been enforced to produce 2D images instead of 3D. This is because of the back-projected conductivity distribution was found to be seriously overlapped through the depth direction and multiple layer images become less meaningful.

Image reconstructed by back-projection is very stable and less sensible by systematic errors and noise. Processing time of back-projection is rapid, which is counted in mini-seconds, is ideal for applying in real-time clinical diagnosis.

2.3.2 Modified Newton-Raphson algorithm

Modified Newton-Raphson algorithm is known as nonlinear least square estimation (Bayford, 2006), which converges in distribution. It solves inverse problem by iterative linearization of the nonlinear relationship between resistivity and the electrical measurement.

In principle, two sets of data are recorded, a reference set V_{ref}, typically from a conductivity of known value c_{ref}, and a second set V_m from the patient with unknown conductivity distribution c. From the EIT equation

$$v = V_m - V_{ref} = S(c - c_{ref}) = Sc \tag{2.54}$$

And the formal solution is

$$(S^t S)^{-1} S^t (V_m - V_{ref}) = c - c_{ref} \tag{2.55}$$

Where S is the sensitivity matrix and the inverse problem of S is very ill-conditioned. Also, S is in general a function of c so direction solution of this equation is not possible. In this case, $S^t S$ is employed because it is invertible. This method is known as pseudoinverse or Moore-Penrose inverse of S. Then, to find out c, a standard approach is to regularize S^tS by Tikhonov Regularization (Yorky *et al* 1987) with the constraint that c-c_{ref} is as close to zero as possible, such that in matrix terms

$$0 = I(c - c_{ref}) \tag{2.56}$$

Where I is the unit matrix. We then combine these two equations and write

$$\begin{pmatrix} v_m - v_{ref} \\ 0 \end{pmatrix} = \begin{pmatrix} S \\ \alpha I \end{pmatrix} (c - c_{ref}) \tag{2.57}$$

There are two opposing 'forces' here. Equation (2.55) is trying to find a value of which fits the data and equation (2.56) is trying to ensure that the value of c is as close to the reference as possible. The parameter α balances these two 'forces'. The solution of the above equation is

$$\left[\begin{pmatrix} S^t & \alpha I \end{pmatrix} \begin{pmatrix} S \\ \alpha I \end{pmatrix} \right]^{-1} \begin{pmatrix} S^t & \alpha I \end{pmatrix} \cdot \begin{pmatrix} V_m \\ V_{ref} \end{pmatrix} = (c - c_{ref}) \tag{2.58}$$

Expanding this gives us the usual solution equation where $\lambda = \alpha^2$. This is the linear form of the modified Newton Raphson algorithm to find the unknown conductivity distribution c, also known as the Newton One-Step Error Reconstruction (NOSER) (Cheney *et al.*, 1990).

2.4 Summary

The background of the Sussex Biomedical Engineering Research Group has been introduced with each developed EIM systems and the current research status in various clinical trials. The mathematical model of EIT has been introduced which

bring out the theory and some examples of electrode configuration. Then the two major image reconstruction algorithms have been described.

Basic theories of the EIT technology are mature over the developments in past two decades. Effort should be made on the customization in particular application, which is the human breast in our case. Indeed, on-going studies are being, and needed to be, carried out by the research groups around the world to improve analytical methods so that EIT could be practically applied in clinical use. As said in one of the EIT review (Barber, 2004), “Credibility is wearing thin and it is time to realize some of the promises made over the past 20 years, or close the shop”.

CHAPTER 3 PRELIMINARY STUDY OF THE SUSSEX ELECTRICAL IMPEDANCE MAMMOGRAPHY PLANAR ELECTRODE ARRAY SYSTEM

The Sussex Electrical Impedance Mammography (EIM) Mk4 system has been developed as a clinical imaging modality for detecting breast cancer *in-vivo*. The system is using a planar electrode array to improve the sensitivity for the screening of human breast and also for ease of clinical use. This chapter mainly shows the designs of planar electrode configuration based system, with detail analysis of sensitivity by using three dimensional simulated and real agar models. Results show that the novel planar electrode system is capable of producing stable and repeatable images. The Sussex Mk4 EIM system is under clinical trial as a potential breast cancer screening imaging modality.

3.1 Introduction

Electrical Impedance Tomography (EIT) has been researched for clinical use (Barber *et al.*, 1983; Metherall *et al.*, 1996; Wang *et al.*, 1998; McEwan *et al.*, 2006; S. C. Murphy *et al.*, 2006; Saulnier *et al.*, 2007; Xu *et al.*, 2007; Halter *et al.*, 2008; Trokhanova *et al.*, 2008; Oh *et al.*, 2011). It has the advantages of: low cost, it is non-invasive and can potentially provide tissue characterisation by measuring the dielectric properties of tissue (Schwan, 1957; Shallof *et al.*, 1996). This potential ability to specifically identify tissue type is unique amongst medical imaging modalities. However, the development of EIT for medical use is challenging as image reconstruction for EIT is a very ill-posed problem, which means even minor perturbations induced during data collection, such as electrode or patient movement cause significant artefacts to be presented in the resulting images.

The specific application of EIT to the detection of breast cancer is called Electrical Impedance Mammography (EIM) (Wang *et al.*, 2001). In EIM electrodes must be placed around the breast for data collection. Two major approaches to electrode placement are found. Electrodes can be placed directly over the surface of

the breast as a single circular array or ring-electrode (Jossinet, 1988; Kerner *et al.*, 2002; Halter *et al.*, 2008). The circular electrode array design was adapted from the design of the first EIT system for chest imaging (Barber *et al.*, 1984). Later, the technique was modified to produce 3D images by acquiring 3D information using multiple rings of electrodes arranged around the surface of a cylinder (Metherall *et al.*, 1996; Wang *et al.*, 2001; Ye *et al.*, 2006). An alternative approach was to use a planar array of electrodes. In this configuration electrodes can be mounted on a hand held probe (Assenheimer *et al.*, 2001; Cherepenin *et al.*, 2001; Kao *et al.*, 2006), on parallel planes (Samani *et al.*, 1999) or on the bottom of a saline filled tank (Wang *et al.*, 2001). A key feature of all these approaches to breast imaging is that the electrodes are in a fixed and known position relative to each other. Typically they are mounted flush with the inner surface of a breast shaped container into which the breast is inserted. This is a key requirement (amongst others) for reducing image artefacts during reconstruction. The breast is a flexible structure and can be moulded to fit the container holding the electrodes. In EIT the further away structures are from the electrodes the less well they will be imaged. The optimum electrode configuration is therefore one which ensures the minimum distance from electrodes to internal structures. Provided the breast is with limited size, a minimum distance can be achieved by flattening the breast as far as possible against the chest wall. The breast then becomes (approximately) a flat cylinder a few centimetres in height with a diameter of the order of 20 cm. If electrodes are placed across the flat face they are a few cm from the chest wall. This is the configuration used in the EIM system being presented herein.

This chapter describes the construction and configuration of the Sussex EIM system (Wang *et al.*, 1998; Wang *et al.*, 2001) designed for breast cancer detection. The EIM system uses a planar electrode array design, associated with a data acquisition method that overcomes low sensitivity problem suffered by the traditional ring-electrode based EIT system design. As the ultimate target of the EIM system is to distinguish between normal and abnormal tissues, the system must be able to acquire data with a high signal to noise ratio (SNR) over a range of frequencies of applied current so that reliable admittivity images can be reconstructed.

3.2 Hardware design

The Sussex 3D EIM system was designed to measure the impedance of the breast. The system has been designed for clinical use so attention has been paid to safety, and ease of use in the clinic. The breast is imaged by inserting it into a cylindrical tank full of saline. The electrodes are set into the base of the tank.

3.2.1 Measurement tank

The characteristics of the measurement tank are listed below:

- 18 cm wide circular saline filled tank (Figure 3.1) with adjustable depth to fit different sizes of breast (Cup AA to G).
- Saline is kept at body temperature during imaging.
- A planar electrode array is fixed to the bottom plane of the tank.
- Electrodes are indented into the bottom plane to avoid direct contact with the breast, so that contact impedance problems can be minimised.

Figure 3.1 *Saline measurement tank embedded in the examination table.*

During examination, the body lies in a prone position, with one breast inserted into the saline filled tank. The base of the tank is raised to touch and compress the breast in order to maximise sensitivity. To satisfy safety requirements (EN60101-1), the AC current is not allowed to exceeding 1mA from DC to 1 kHz. The frequency of the injected current can be set to one of several values in the frequency ranged between 10 kHz to 10 MHz in our Mk4 EIM system.

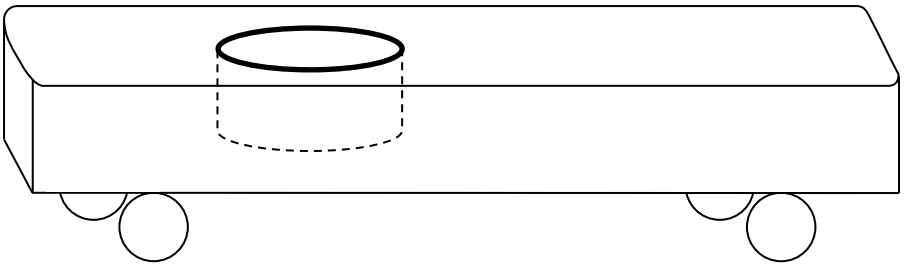

Figure 3.2 *The sketch of saline measurement tank and the examination table*

3.2.2 Data acquisition method

A novel feature of the system is the pattern of electrode placements and the choice of current patterns and receive measurement electrode pairs. Current is applied between a pair of electrodes and measurements made between electrode pairs (four-electrodes measurement). There are a total of 85 electrodes evenly distributed in a hexagonal pattern (Figure. 3.3). The distance between adjacent electrodes is 1.7 cm. 123 drive pairs are used and the total number of measurements is 1416. A multiplexing device has been used to switch between different driving and receiving electrodes.

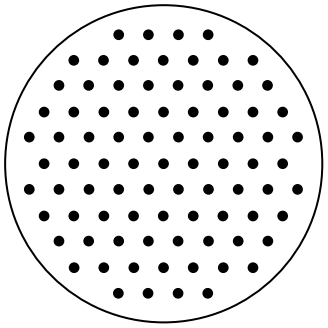

Figure 3.3 *85 electrodes in a hexagonal grid.*

The data acquisition pattern is novel. When a drive current is passed between a pair of electrodes voltage measurement is confined to a set of electrodes local to the drive pair, rather than collecting data over all possible pairs. The principal reason for this approach is to confine data acquisition to strong signals with best SNR and minimised "dynamic range". Measurements from electrode pairs away from the drive pair will be small and will inevitably have low SNR. These data are not used. The sets of data used are shown in Figure 3.4 and 3.5. Figure 3.4c shows a set of electrodes (within and on the blue hexagon) and a pair of drive electrodes (red circles). Data is only collected for this drive pair using the electrodes on and within

the hexagon. In particular data is only collected from adjacent pairs of electrodes parallel to the line joining the drive pair.

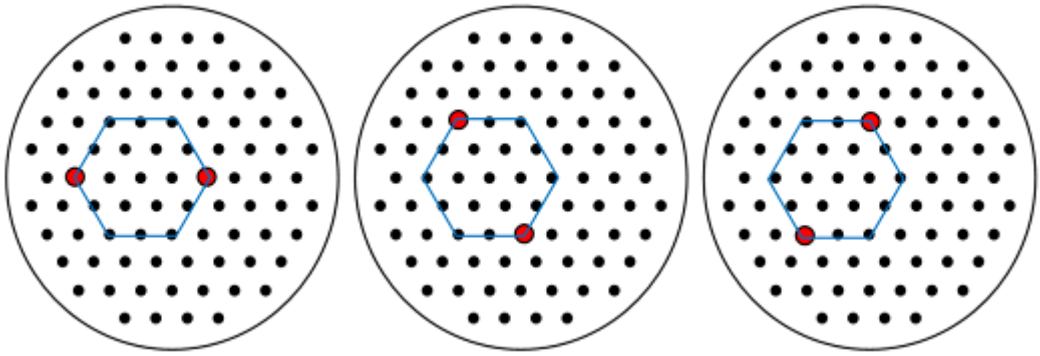

(a) (b) (c)

Figure 3.4 *Three pairs of drive electrodes (in red) for a local region (blue hexagon).*

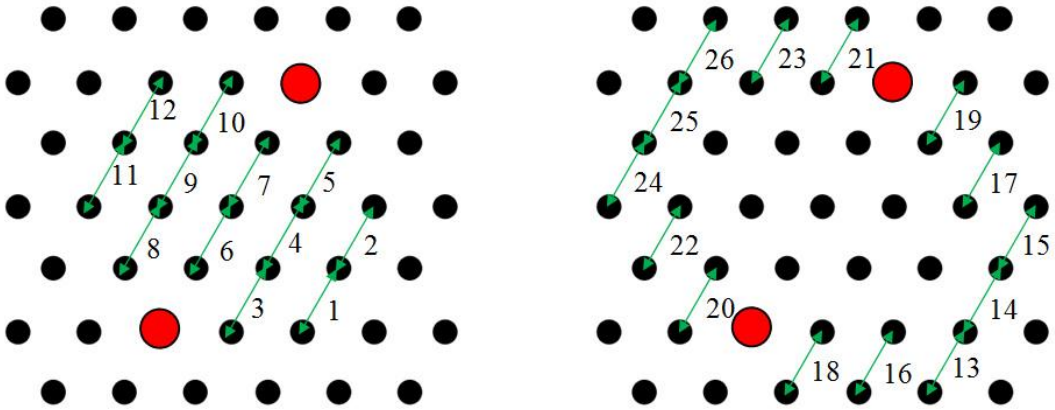

(a) (b)

Figure 3.5 *Receiving electrode pairs for each driving electrode pair.*

(a) 12 measurements within local region
(b) additional 14 measurements outside local region

There are 12 such pairs (Figure 3.5a). For this hexagon two other drive pairs are defined (Figure 3.4a and 3.4b) and for these drive configurations data is only collected from the equivalent 12 electrode pairs parallel to the drive pair. The three sets of data (3 drives, 36 measurements) constitute an isotropic data set for this hexagon. The hexagon is moved on by one electrode spacing and another data set collected. In effect the 3 fold hexagonal pattern is scanned over the face of the tank. Clearly within the hexagon for one drive pair other adjacent electrode pairs are available but the signals from these pairs will be reduced because their axes are not parallel to the axis of the drive pair. For example, if a pair is selected whose axis is

normal to the drive pair in a uniform tank the voltage measurement would have a zero value.

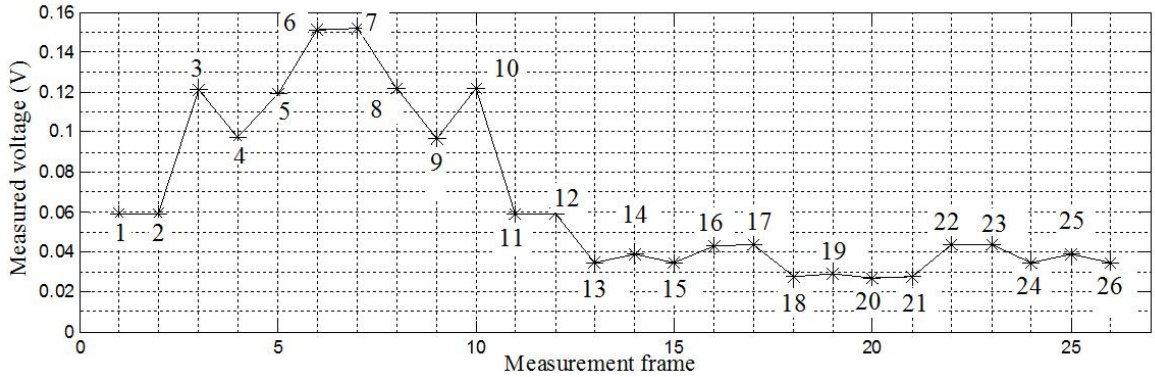

Figure 3.6 *Dynamic range of the voltage measurement frames according to Figure 3.4, which is simulating the measurement voltage of saline using the 60th current driving electrodes pair.*

Simulation shows that the sensitivity outside the local hexagonal region is lower than inside. There are an additional 14 pairs of receive electrodes outside the local region (Figure 3.5b) giving with the existing measurements a total of 26 measurements. Figure 3.6 plots the simulated values of these 26 voltage measurement for uniform conductivity, such that the first 12 measurements are within the local region, and the remaining measurements are outside the local region. The model is for a homogeneous distribution of saline with 0.05 S/m conductivity and 1 mA peak to peak current. The lowest reading within the local region is around 6 mV, twice that of the lowest reading outside the region, which is around 3 mV. Electrode pairs even further away would produce even smaller signals. Given that data collection time is linearly dependent on the number of data samples collected and reconstruction time is also linearly dependent on the number of data samples collected, it seems sensible to as far as possible concentrate on collecting signals of large amplitude. It is not claimed here that the optimum data collection strategy is being used but that the strategy adopted is a useful a-priori approach. Almost certainly a more detailed investigation can produce an improved strategy, but this has not been attempted here. Unlike traditional circular arrays the dynamic range of the signals is significantly smaller (~2.5:1) and the signal amplitude is large. Local regions close to the boundary will have less than twelve pairs of receive electrode pairs, which is why the number of measurements is less than 1476.

3.3 Software design

3.3.1 Mesh structure

Figure 3.7a presents a two dimensional mesh made up of triangles of same area, except for the triangles near the boundary. A three dimensional mesh is constructed by stacking several of these meshes on top of each other to represent several layers, linking corresponding elements to form triangular prisms between layers and dividing each prism into three tetrahedrals.

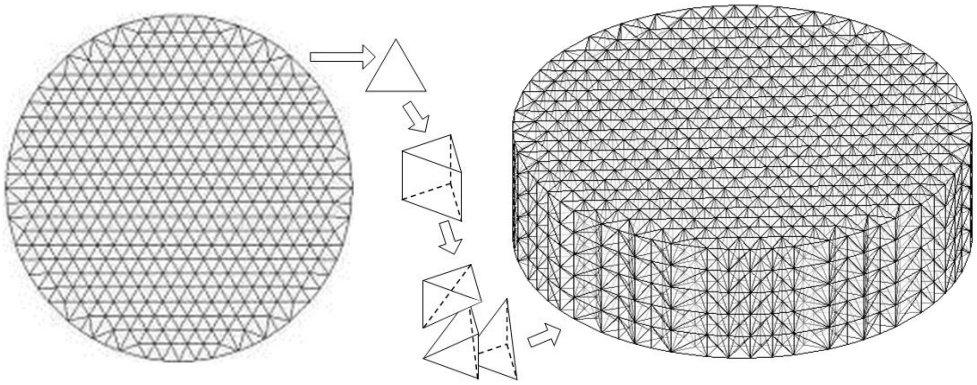

(a) (b)

Figure 3.7 *The transformations of (a) a two dimensional mesh with triangular elements into (b) three dimensional mesh with tetrahedral elements*

Figure 3.7b shows an example of a complete three dimensional mesh. There are in total 1684 nodes and 7020 tetrahedral elements in this mesh with five layers. The thickness for each layer need not necessary be the same as the other layers. Since sensitivity decreases with depth it may be useful to use thicker layers further away from the electrodes but this is not done here. The dimensions of the mesh are such that the positions of the electrodes lie on some of the nodes of the mesh. The mesh makes no attempt to model the electrodes in detail. This is possible in principle but will increase the number of mesh elements significantly and hence reconstruction time. Central to any EIT reconstruction algorithm is the need to accurately predict the voltages on the electrodes for a known conductivity distribution. To do this would require electrode modelling. It has long been known that this problem (and others) of data inconsistency can be at least partially addressed by using 'differential' imaging i.e. by comparing measurements taken with a breast in the tank and with saline only. This is the approach taken in the

current work. Each data set for reconstruction is therefore two data sets, one with the breast present and one without.

3.3.2 Reconstruction method

There are two sets of recorded data and one set of simulated data in the reconstruction of a three dimensional image. These are a reference set V_{Ref}, typically from a uniform conductivity of known value, a second set V_{Pat} from the patient or experimental phantom, and also a simulated set V_{RefSim} for a uniform phantom calculated using the forward transform. Then V_{Norm} is calculated in equation (3.1) as a normalised data set for the image reconstruction algorithm calculation. Taking the ratio or measured patient data to measured uniform data significantly reduces the effect of not using an electrode model.

$$V_{Norm} = V_{\mathrm{Re}\,fSim} \times V_{Pat} / V_{\mathrm{Re}\,f} \tag{3.1}$$

Absolute conductivity images shown in this paper are reconstructed using a Tikhonov Regularization method (Phillips, 1962; Tikhonov, 1963) as described by equation (3.2).

The reconstruction is iterative. An initial uniform conductivity c_0 is assumed (this is taken to be the same as the saline conductivity). A sensitivity matrix relating changes in conductivity to changes in voltage measurements (Geselowitz, 1971) is constructed using this starting conductivity and the tank geometry. A new estimate of the conductivity is then calculated using equation (3.2) with n = 0 (Barber, 2000). A new sensitivity matrix is calculated and a second updated estimate of conductivity calculated. This process is repeated until no further change in conductivity occurs.

$$c_{n+1} = \left[S_n{}^t S_n + \lambda I\right]^{-1}\left(S_n{}^t (V_{norm} - V_{\mathrm{Re}\,fSim}) - \lambda(c_n - c_0)\right) + c_n \tag{3.2}$$

S_n is the sensitivity matrix for conductivity c_n, and I is the identity matrix. V_{Norm} and V_{RefSim} are the same as those in equation (3.1). c_{n+1} is the unknown conductivity distribution that we are searching for, and c_0 is the simulated reference uniform conductivity distribution, which is known to be 0.5 mS/cm. To summarize the iterative process, a flowchart has been drawn in Figure 3.8 to describe the calculation process.

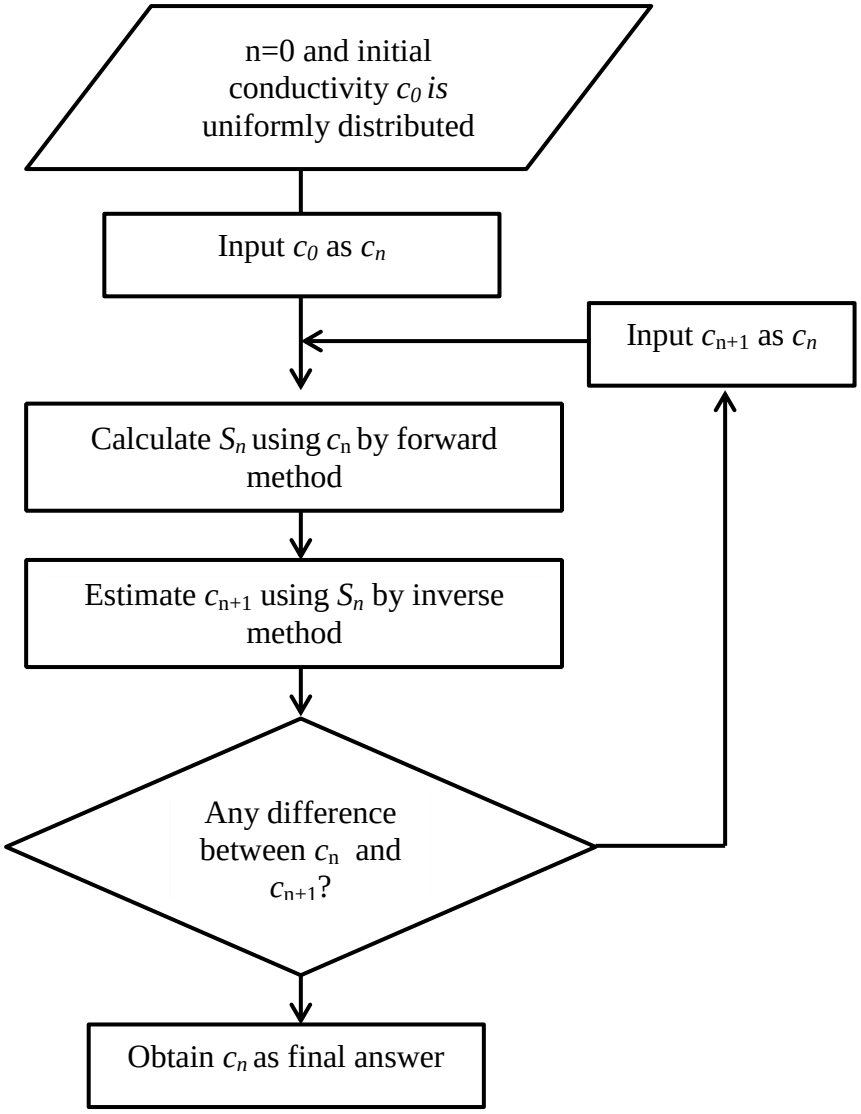

Figure 3.8 *Flow chart of the iterative reconstruction method*

The regularisation parameter lambda (λ = 1.5759) was obtained by using the L-curve method (Hansen, 1992) to make sure the iterating values in each pixel are actually converging into a solution. This value has been used in the reconstruction of all images.

3.4 Experiment

3.4.1 Objective

Simulated and real experiments have been carried out to analyse the sensitivity of the system, particularly for the sensitivity against depth. There are two sets of data: one is the simulated measurement data calculated using the forward transform, the second set is acquired from experiments using an agar phantom soaked in saline.

The model used to generate simulated data is configured to match as closely as possible the configuration of the physical model so that useful comparisons can be made. Simulated and real acquired data are reconstructed using the same identical image reconstruction method, with the same regularization parameter. Through the comparison between simulated images and agar images, we can estimate the error in data acquisition such as noise and stray capacitance of the electrical components and assess the effect on image quality. The phase angle difference between the reference and measured data has not been investigated because the permittivity of wet agar is assumed to be a constant. The magnitude of the voltage signal is taken to be the same as the real component of the signal, or related to it by a constant factor.

3.4.2 Experimental setup

The mesh model for the experimental set up is shown in Figure (3.9). A circular measurement tank in 18 cm diameter and 5 cm deep is used. The calculated volume is 1272 cm^3, which was designed to fit a breast with a maximum cup size of G. The three dimensional saline tank is represented by a five layers mesh (Figure 3.9b) and each layer is 1 cm thick.

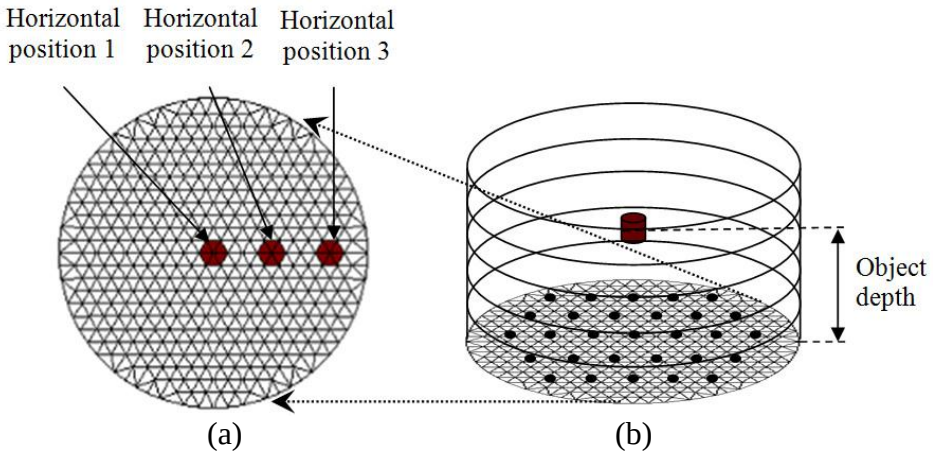

Figure 3.9 *(a) Top view: Three horizontal positions of the testing object; (b) 3D view: The measuring of object depth from electrode plane.*

Simulated data consists of uniform conductivity assigned to all mesh elements except for one hexagonal prism shaped object, which is located in three different horizontal positions (Figure 3.9a): centre (position 1), midway from centre to boundary (position 2), and near boundary (position 3). The width and thickness of the object are 1.4 cm and 1 cm, respectively. Conductivity of the object is 0.6

mS/cm, which is 20% higher than the background saline conductivity 0.5 mS/cm. The conductivity difference between human breast stroma tissue and cancerous malignant tissue at 20 kHz is of similar ratio (Wang et al., 2001). 5 vertical positions have been defined by using a 5 layer 3D mesh. Each layer contains 3 horizontal positions, in total there are 15 different locations of the object. Random white noise has been added to the simulated voltage measurement. The noise has value of 60 dB Signal to Noise Ratio (SNR) to simulate the real acquisition system.

An agar experiment has been set up for the comparison between simulated results. Saline has been used as the 0.5 mS/cm homogeneous conductivity background medium, and an agar object has been suspended in the designed location by using a non-conductive string. The agar object has been cut in cylindrical shape with diameter of 1.4cm and thickness of 1cm. The conductivity of agar is 0.6 mS/cm in a paste state before solidification, and the data was acquired 7 to 10 hours after the complete solidification. Thus, there may be around 150% increase of conductivity due to the agar drying out.

3.4.3 Analysis method

Key measures for any imaging system are sensitivity and resolution. The sensitivity of the system is quantified in the current work by a Half Maximum Height Area (HMHA) value. The image of the object is blurred relative to the true object by the imaging process. Since the reconstructed object is usually attenuated like a normal distribution with a peak at the centre region and does not have a sharp edge, a region has to be defined for the measurement of this circular object. The region is called the Half Maximum Height Area (HMHA) and is defined below. By integrating every signal above saline conductivity within this radius, we can compare the sensitivity of a single object located at different depths and horizontal positions. The resolution of the imaging system as a function of depth is relatively poor so that the image of an object will cross several layers. The measurements for HMHA are confined to the layer in which the object is situated.

The HMHA is calculated as below:

1. Elements of a reconstructed conductivity image, which are located as one line on one of the 2D layers as shown in Figure 3.10. The line is crossing through the

centre of the mesh from one end to the other end, as coloured in red. Three possible horizontal positions of the object are highlighted in blue. When we plot the conductivities of this line of elements against x-axis, we obtain the plot of circles in Figure 3.11. Zero value of x-axis represents the centre position of the 2D mesh.

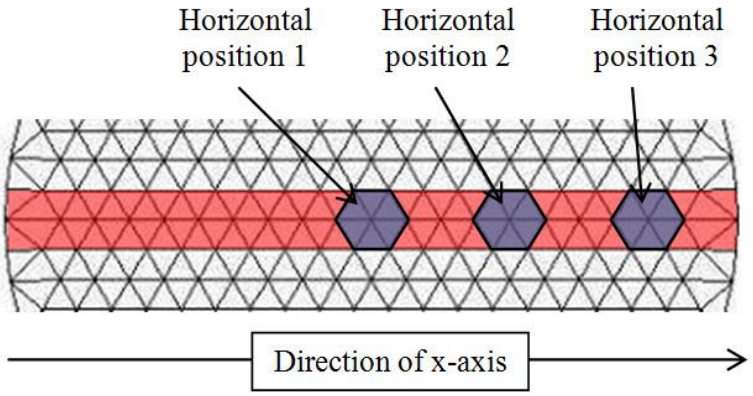

Figure 3.10 *Elements using for curve fitting in calculating FWHM.*

2. A curve fitting method is applied to estimate the solid curve in black. By calculating the full width half maximum (FWHM) we obtain the horizontal black dotted line. The area indicated by the green dotted line would be integrated as the HMHA value by using the area above the dotted line.

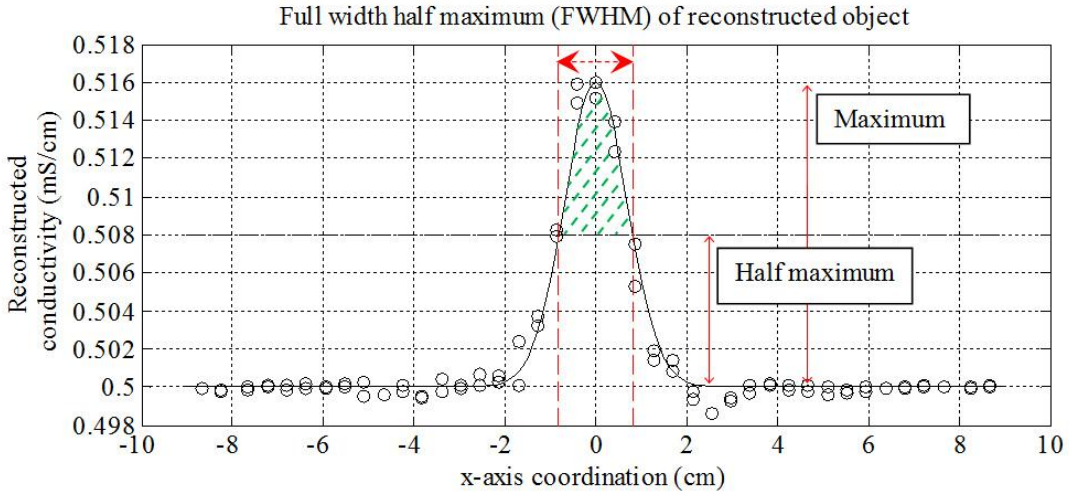

Figure 3.11 *An example of HMHA calculation for an object located in position 1.*

3.5 Results and Analysis

Figure 3.12 plots the simulated voltage calculated by the forward method against the recorded voltage from an agar experiment, both are measuring homogeneous conductivity distribution (saline) in 0.5 mS/cm with a depth of 5 cm. One dot represents one measurement datum and there are 1416 points in total. The values have been normalized using the maximum value. Although the curve demonstrates significant scatter the overall relationship between the simulated and real data is linear. The phase angle difference measured between the reference signal and the return signal is constant. The standard deviation of the 1416 measurements is 0.4270.

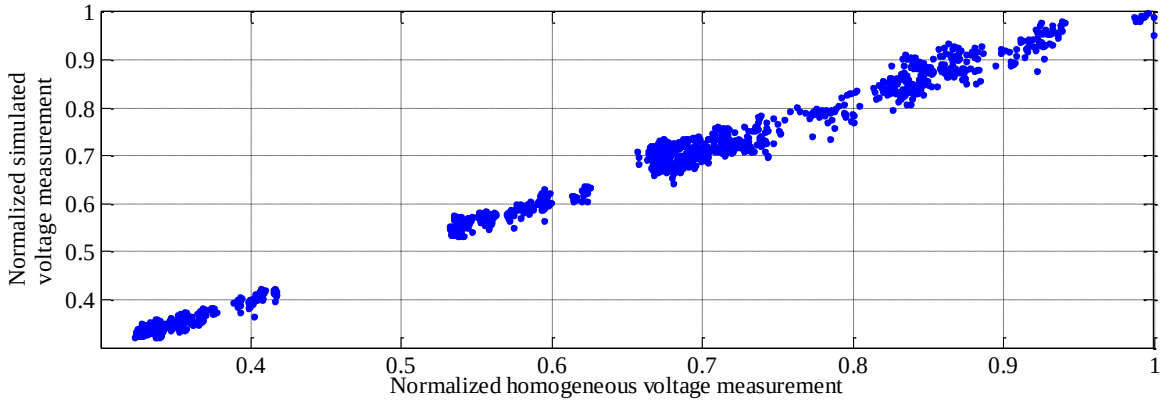

Figure 3.12 *Plotting the normalized values of simulated voltage measurement against real homogeneous voltage measurement.*

The sensitivity to a malignant cancer tissue object is evaluated by the Half Maximum Height Area (HMHA) value. The calculated HMHA values are listed in Table 3.1 and plotted as curves in Figure 3.13. In simulation, the HMHA values between different positions are close to each other. The ratio of the minimum and maximum value is ~1:6, showing that the sensitivity of a 1.4 cm diameter malignant cancer object can be reduced by 6 times inside a 4.5 cm depth of stroma tissue. From agar results, the sensitivity ratio was increased to ~1:3. The similarity between the curves in three different positions also reflects that the sensitivity is evenly distributed over the electrode plane, a consequence of the scan like form of the collection strategy.

Table 3.1 *Half Maximum Height Area (HMHA) of simulation and agar experimental results.*

Object depth	Horizontal position	HMHA of Simulation (mS)	HMHA of Agar (mS)
0.5 cm	1	0.17	0.29
1.5 cm	1	0.074	0.12
2.5 cm	1	0.031	0.12
3.5 cm	1	0.022	0.12
4.5 cm	1	0.026	0.16
0.5 cm	2	0.16	0.30
1.5 cm	2	0.067	0.13
2.5 cm	2	0.036	0.089
3.5 cm	2	0.023	0.078
4.5 cm	2	0.025	0.098
0.5 cm	3	0.14	0.28
1.5 cm	3	0.062	0.073
2.5 cm	3	0.029	0.090
3.5 cm	3	0.031	0.080
4.5 cm	3	0.023	0.071

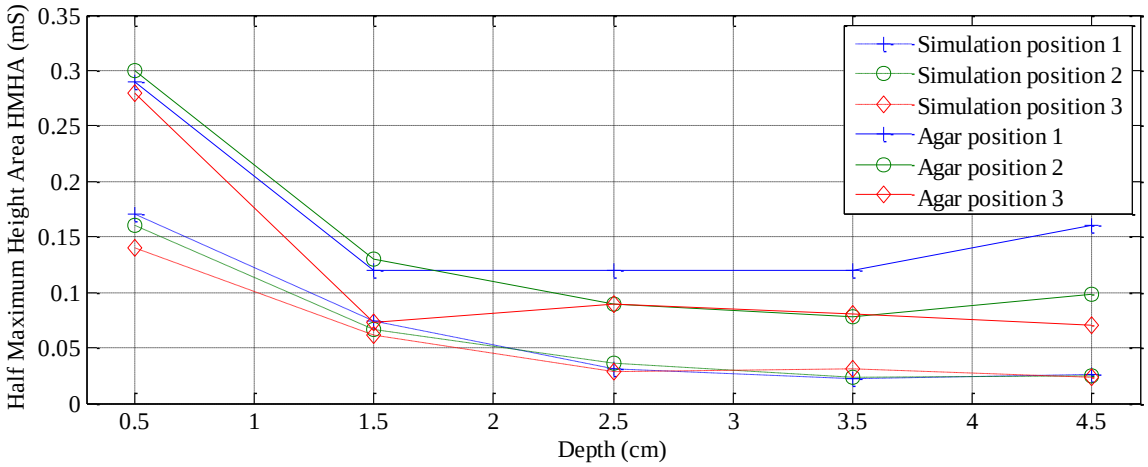

Figure 3.13 *Half Maximum Height Area (HMHA) of simulated and agar plotted against depth.*

The HMHA values of agar images tend to be double those from simulated images. As it was not possible to exactly match the size and shape and conductivity of the physical objects compared to the simulated objects exact matching is not really expected. The variation in sensitivity with depth is similar for both simulations and agar. Sensitivity can also be visually assessed from the reconstructed images presented in Figures 3.14, where the green circles indicate the original object locations.

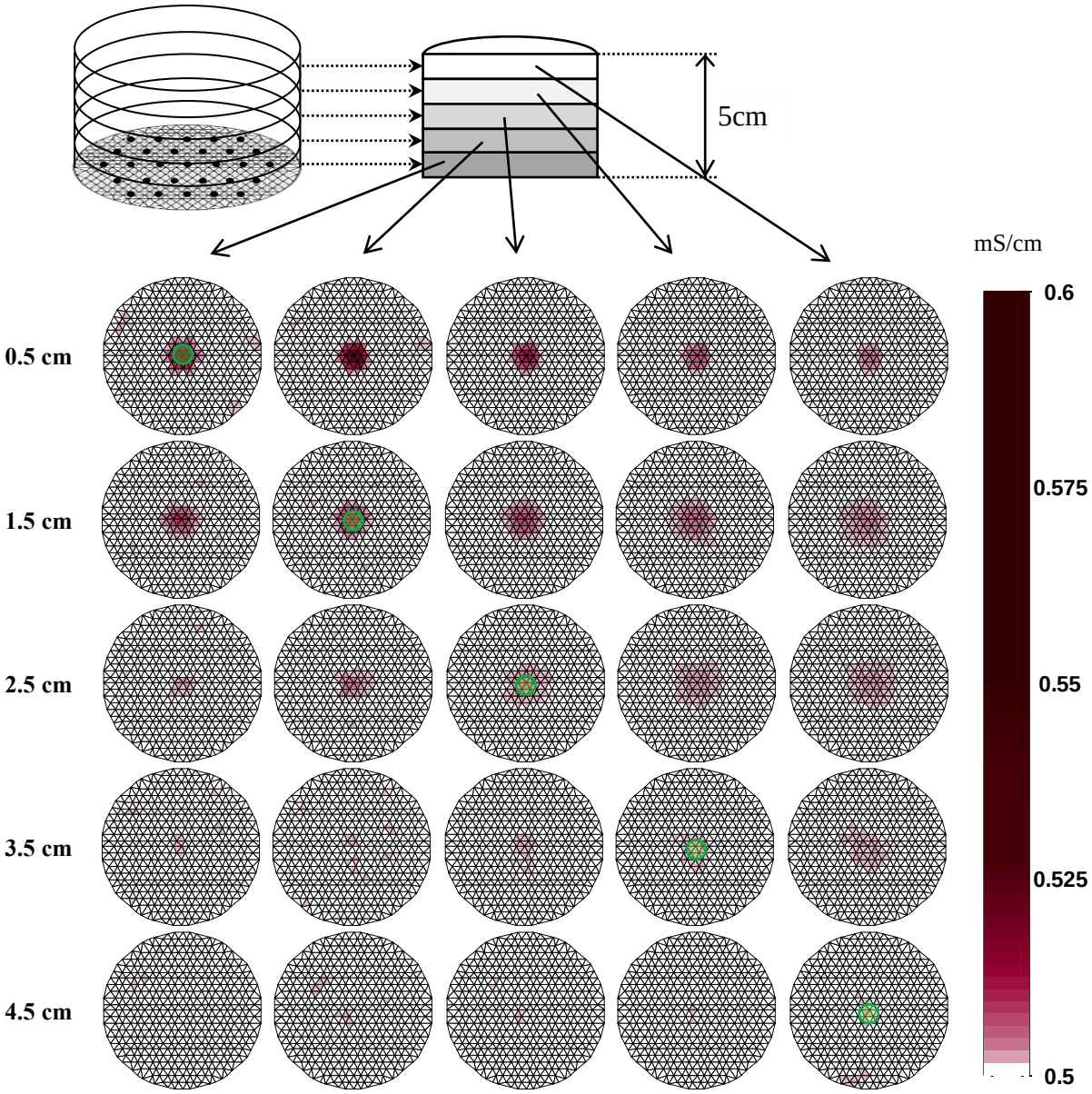

Figure 3.14 *Reconstructed images of simulated experiments with object in position 1.*

3.6 Conclusion and Future Work

A planar electrode array EIM system has been developed to detect breast cancer *in-vivo*. The design of measurement tank, electrode position and current injection pattern have been customized such that, the signal quality and sensitivity can be optimised for acquiring signals from the human breast. Sensitivity to an object for both simulation and agar experiments has been measured using the Half Maximum Height Area (HMHA) method, while the background conductivity is relative to stroma tissue and the object conductivity is relative to that of cancerous malignant tissue at 20 kHz. The falling sensitivity against depth for simulations is

similar to the agar experiments and the system performs as expected. Sensitivity is seen to reduce to around one-sixth by comparing values for the layer adjacent to the electrodes and the layer at a depth of 4.5 cm. The sensitivity values and the reduction in sensitivity with depth are similar for different positions across the tank, a reflection of the data collection strategy.

Further works have to be planned for future study. The 14 additional measurements plotted in figure 3.6 may need to be optimised to increase sensitivity for clinical use. Imaging of more complex multi-tissue models is planned. In signal calibration, there is a need to verify the performance at various frequencies, as the system has been designed to process signals with frequency ranging from 1 kHz to 10 MHz. Image reconstruction algorithm and regularization methods have to be modified to reconstruct multiple frequencies images, so that dielectric properties of the breast can be imaged to aid in the diagnosis of breast cancer.

3.7 Summary

This chapter introduced the Sussex Mk4 EIM system, which is developed for the detection of breast cancer in clinical use. Advantages on the design of saline measurement tank and electrode configuration are introduced. The novel current drive and voltage receive pattern are presented. The image reconstruction method for reconstructing 3D image is briefly introduced. Simulation studies and agar experiment have been carried out to test the performance of the system. Half Maximum Height Area (HMHA) method is used to justify sensitivity to the object against depth. From the results, the simulated result and agar result show similarity on sensitivity, that strong signal could be found from region near the electrodes, whereas sensitivity reduced to around one-sixth at a depth of 4.5 cm. Further works has been suggested for the system to be ready to process clinical data.

CHAPTER 4 IMAGE RECONSTRUCTION AND REGULARIZATION METHODS IN 3D ELECTRICAL IMPEDANCE MAMMOGRAPHY

This chapter presents the image reconstruction method that reconstructs data acquired from the Sussex Mk4 EIM system. The system has been developed for the detection of breast cancer by using EIM technique. Comparing to the other scanning technologies such as CT and MRI, the unique dielectric properties of biological tissues gives electrical Impedance Tomography (EIT) a potential advantage in diagnosing cancer.

The modified Newton-Raphson method is usually applied to reconstruct EIT images. The method assumes the EIT problem as a severely ill-posed non-linear equation. This is an inverse problem and could be solved by the estimation of the sensitivity matrix iteratively. To improve the accuracy of solution, regularisation has to be enforced, and the regularization method should be customized according to the configuration of the EIM system. The traditional Tikhonov regularization method was derived to solve ill-posed inverse problem, however the negative values yielded in the solution damaged the stability of the iterative reconstruction process. Besides, negative values create difficulties in the diagnosis of abnormal tissues by the analysis of dielectric properties from the resulting images. We need to make a balance between high regularization for enhanced stability and low regularization for increased accuracy.

This chapter starts by reviewing the Sussex Mk4 EIM system that has been developed for breast cancer detection, followed by the discussion of two regularization methods, positivity constraint and depth dependent regularization, which was enforced to the modified Newton-Raphson reconstruction for processing data acquired by the Sussex Mk4 EIM system. Simulated results were analysed to quantify the accuracy and stability of the algorithm.

4.1 Introduction

The majority of image reconstruction algorithms employed in clinical EIT studies use single iteration methods such as the Back-Projection method (Barber *et al.*, 1987) and the Newton's method (Cheney *et al.*, 1990). Single step method has higher stability and short processing time (Holder, 2004). Although non-linear or multiple iteration approaches are supposed to be more accurate and could produce higher spatial resolution images, ill-posedness of the EIT inverse problem could be increased by the wide range of human tissue conductivities, which increases the sensitivity to noise generated by incompatible information such as the anatomical differences between the mesh used and the subject's true anatomy, decreasing the reliability of images of clinical interest.

In breast cancer detection, dielectric properties of human tissues (Cole, 1940; Cole *et al.*, 1941) could be extracted from multiple frequency's *in-vitro* EIT experiments (Jossinet, 1988; Wang *et al.*, 1995). It shows us the possibility of acquiring further human tissue information than conventional screening technologies such as X-ray CT and MRI. Because of this, Electrical Impedance Mammography (EIM) images are usually analysed in multiple frequencies instead of a single frequency. To reconstruct multiple frequency breast images, both single step and iterative image reconstruction approaches have been used. The Dartmouth group (Osterman *et al.*, 2000; Kerner *et al.*, 2002; Soni *et al.*, 2004; Halter *et al.*, 2008) has successfully produced meaningful dual frequency *in-vitro* and *in-vivo* breast images, where the inverse problem was solved iteratively using non-linear Newton's method with regularization that reduces numerical instabilities. The Moscow group (Cherepenin *et al.*, 2000) developed a 3D EIM system that reconstructs physiological images (Cherepenin *et al.*, 2001; Cherepenin *et al.*, 2002; J. Campbell *et al.*, 2007; Trokhanova *et al.*, 2008) by using Back-Projection method. The conductivity of mammary glands were found to be related to different physiological events. The Duke University group developed a 3D EIM system (Ye *et al.*, 2006; Ye *et al.*, 2008) that solves the inverse problem using non-linear Gauss-Newton method with Tikhonov regularization, the solution converged well and produced image with the expected phantom object location.

Although EIM studies have been carried out for over 10 years, improvements are needed for EIM reconstruction algorithms. Firstly, image quality is still being affected by systematic noise which hamper reliability. Most of the iterative methods suffer from this problem. Secondly, there is a lack of normalization method for the anatomical and physiological differences between patients which interferes the diagnosis of breast cancer. Thirdly, the approval of clinical trial is difficult. Clinical trials may pose some ethical issues in certain countries, and this can delay the development EIM systems to be employed as effective conventional breast screening tools.

This chapter presents the studies of image reconstruction methods, which are developed for processing data acquired by the Sussex EIM Mk4 system. The system has been developed by the Biomedical Engineering Research Group for detecting breast cancer *in-vivo*. The research target focuses on the diagnosing ability using breast tissues' dielectric properties which enables us to characterise normal and abnormal breast tissues. The "stability" of reconstructed image has been given a higher priority than increasing the "spatial resolution" of images with reasonable and decent "accuracy". The modified Newton-Raphson iterative method has been implemented with the positivity constraint (Barber, 2004) regularization method and the depth dependent regularization methods, which were firstly enforced to EIM system for improving reconstruction stability. Regularization parameter is defined by the L-curve (Hansen, 1992) method. Model have been set up to simulate the environment with and without noise for analysing the performance of the new regularization methods.

4.2 Non-linear modified Newton-Raphson image reconstruction algorithm

The modified Newton-Raphson method was frequently employed in EIT since its first application in EIT in 1980's (Yorkey *et al.*, 1987). It is an iterative technique that starts solving an inverse problem by an initial guess model. A relationship matrix is necessary to be estimated such that an assumed solution could be calculated by a simple matrix transformation. By comparing the assumed solution to the actual measured solution, the relationship matrix could be re-estimated by a modified

model which subtracts the error, thus calculating a new assumed solution. This process is iterative and solution should be converged to represent a successful result.

In EIT, if we consider the measured voltage distribution and conductivity distribution as two single-column arrays, the relationship between these two arrays could be described by a matrix, termed as *sensitivity matrix*, which is based on how voltage is developed at every point when the current is applied. To calculate the conductivity distribution from a voltage distribution, we have to solve the inverse problem with the sensitivity matrix. This inverse calculation is considered as an ill-posed problem and the situation could be affected by the length of conductivity distribution array and voltage distribution array. Regularization is a standard approach to this problem, and Tikhonov Regularization (Phillips, 1962; Tikhonov, 1963) is the method that is generally used in the EIT society.

Two sets of data are recorded. The first set of data is a reference referred as V_{ref}, typically from a conductivity of known value c_{ref}, and the second set of data V_m from the patient with unknown conductivity distribution c. From the EIT equation.

$$v = V_m - V_{ref} = S(c - c_{ref}) = Sc \tag{4.1}$$

And the formal solution is

$$(S^t S)^{-1} S^t (V_m - V_{ref}) = c - c_{ref} \tag{4.2}$$

Where S is the sensitivity matrix and the inverse problem of S is very ill-conditioned. Also, S is in general a function of c so direct solution of this equation is not possible. A standard approach to this is to regularize S^tS by Tikhonov Regularization (Yorky et al 1987) with the constraint that c-c_{ref} is as close to zero as possible, such that in matrix terms

$$0 = I(c - c_{ref}) \tag{4.3}$$

where I is the identity matrix. We then combine these two equations and write

$$\begin{pmatrix} V_m - V_{ref} \\ 0 \end{pmatrix} = \begin{pmatrix} S \\ \alpha I \end{pmatrix} (c - c_{ref}) \tag{4.4}$$

There are two opposing ‘forces’ here. Equation (4.2) is trying to find a value of which fits the data and equation (4.3) is trying to ensure that the value of c is as close to the reference as possible. The parameter α balances these two ‘forces’. The solution of the above equation is

$$\left[\begin{pmatrix} S^t & \alpha I \end{pmatrix} \begin{pmatrix} S \\ \alpha I \end{pmatrix}\right]^{-1} \begin{pmatrix} S^t & \alpha I \end{pmatrix} \cdot \begin{pmatrix} V_m \\ V_{ref} \end{pmatrix} = (c - c_{ref}) \tag{4.5}$$

Once we have calculated c_1 the first iteration of c we then compute S with this value and replace c_{ref} with c_1 and repeat the process. But this time our constraint is trying to set $c - c_1$ to zero. What we actually want is for the constraint to continue to set $c - c_{ref}$ to zero. To do this we write $c - c_{ref} = c - c_1 + c_1 - c_{ref} = c - c_1 + (c_1 - c_{ref}) = 0$ *or* $c - c_1 = -I\,(c_1 - c_{ref})$ as the constraint. We now write

$$\begin{bmatrix} V_m - V_{ref} \\ -\alpha I (c_1 - c_{ref}) \end{bmatrix} \cdot c = \begin{pmatrix} S_1 \\ \alpha I \end{pmatrix} (c - c_1) \tag{4.6}$$

Our iteration then becomes

$$\left[\begin{pmatrix} S_1{}^t & \alpha I \end{pmatrix} \begin{pmatrix} S_1 \\ \alpha I \end{pmatrix}\right]^{-1} \begin{pmatrix} S_1{}^t & \alpha I \end{pmatrix} \cdot \begin{bmatrix} V_m - V_{ref} \\ -\alpha (c_1 - c_{ref}) \end{bmatrix} = (c - c_1) \tag{4.7}$$

For the nth iteration it is

$$\left[\begin{pmatrix} S_n{}^t & \alpha I \end{pmatrix} \begin{pmatrix} S_n \\ \alpha I \end{pmatrix}\right]^{-1} \begin{pmatrix} S_n{}^t & \alpha I \end{pmatrix} \cdot \begin{bmatrix} V_m - V_{ref} \\ -\alpha (c_n - c_{ref}) \end{bmatrix} = (c - c_n) \tag{4.8}$$

Expanding this gives us the usual solution equation,

$$(S_n{}^t S_n + \lambda I)^{-1} \left(S_n{}^t (V_m - V_{ref}) - \lambda I (c_n - c_{ref}) \right) = (c - c_n) \tag{4.9}$$

where $\lambda = \alpha^2$.

This is the non-linear form of the modified Newton-Raphson algorithm (Lionheart, 2004). The convergence of solution depends on λ whereas the original algorithm effectively reduces λ at each iteration. The process of iteration can

continue as far as is justified by the signal-to-noise ratio in the measured data, and a criterion should be defined for stopping the iteration process.

Enforcing Tikhonov Regularization can generally solve the ill-posed problem, but not enough to achieve acceptable stability and accuracy. The more regularization constraint that can be added the closer we can get to the true solution. The next section introduces another regularization technique for the modified Newton-Raphson algorithm which could ensure enough stability and accuracy.

4.3 Methods

We need to tackle the problem of generating negative conductivity values. These conductivity values are reconstructed by the modified Newton-Raphson algorithm using identity regularization matrix *I*. It is a serious problem for iterative process because any negative values from the estimated solution could affect the values in the sensitivity matrix that is used to calculate for the next iteration. One of the methods to tackle this problem is to enforce positivity constraint in the reconstruction algorithm.

L-curve method has been chosen for estimating the value of regularization parameter λ. Findings show that traditional methods are not enough to search for the "correct" corner. Further details are written in the following sub-section.

Another improvement on the modified Newton-Raphson algorithm is for the absolute values in different layers. Since sensitivity decrease through depth, the regularization constraint should be relaxed for those layers which produce weaker signals because they are further away from the electrode.

4.3.1 Positivity Constraint

We attempt to improve the stability and accuracy by adding constraint in the regularization of the image reconstruction algorithm. Indeed in multiple frequency imaging, attention should be given to the convergence property through iteration because we want to avoid reconstruction errors being multiplied in multiple frequencies analysis. When we look at the negative value problem, an additional regularization constraint can be enforced in order to obtain a more promising

solution. The positivity constraint (Barber, 2004) method replaces the subtraction $c - c_{ref}$ by a logarithm division $log(c / c_{ref})$ in equation (4.1) and the equation becomes

$$\Delta \log v = \log\left(\frac{V_m}{V_{ref}}\right) = F \log\left(\frac{c}{c_{ref}}\right) = F\Delta \log c \tag{4.10}$$

The new sensitivity matrix F is calculated by using the know values of v, S and c that derived below.

$$F = \frac{\Delta \log v}{\Delta \log c} = \frac{\Delta \log v}{\Delta v} \cdot \frac{\Delta v}{\Delta c} \cdot \frac{\Delta c}{\Delta \log c} = \frac{1}{v} \cdot S \cdot c \tag{4.11}$$

Equation (4.3) becomes

$$0 = I \cdot \log\left(\frac{c}{c_{ref}}\right) \tag{4.12}$$

Then

$$\begin{bmatrix} \log\left(\frac{V_m}{V_{ref}}\right) \\ 0 \end{bmatrix} = \begin{bmatrix} F \\ \alpha I \end{bmatrix} \log\left(\frac{c}{c_{ref}}\right) \tag{4.13}$$

Now for non-linearity iteration, we write

$$\log\left(\frac{c}{c_{ref}}\right) = \log\left(\frac{c}{c_1} \times \frac{c_1}{c_{ref}}\right) = \log\left(\frac{c}{c_1}\right) + \log\left(\frac{c_1}{c_{ref}}\right) \tag{4.14}$$

In matrix form

$$-I \cdot \log\left(\frac{c_1}{c_{ref}}\right) = \log\left(\frac{c}{c_1}\right) \tag{4.15}$$

and first iteration becomes

$$\begin{bmatrix} \log\left(\frac{v_m}{v_{ref}}\right) \\ -\alpha I \log\left(\frac{c_1}{c_{ref}}\right) \end{bmatrix}^{-1} = \begin{bmatrix} F_1 \\ \alpha I \end{bmatrix} \log\left(\frac{c}{c_1}\right) \tag{4.16}$$

Thus in matrix form for the nth iteration

$$\left[\begin{pmatrix} F_n^{\,t} & \alpha I \end{pmatrix}\begin{pmatrix} F_n \\ \alpha I \end{pmatrix}\right]^{-1}\begin{pmatrix} F_n^{\,t} & \alpha I \end{pmatrix}\cdot\begin{bmatrix} \log\left(\frac{v_m}{v_{ref}}\right) \\ -\alpha I \log\left(\frac{c_n}{c_{ref}}\right) \end{bmatrix} = \log\left(\frac{c}{c_n}\right) \qquad (4.17)$$

Expanding this gives us the solution equation,

$$(F_n^{\,t}F_n + \lambda I)^{-1}\left(F_n^{\,t}\log\left(\frac{v_m}{v_{ref}}\right) - \lambda I \log\left(\frac{c_n}{c_{ref}}\right)\right) = \log\left(\frac{c}{c_n}\right) \qquad (4.18)$$

where $\lambda = \alpha^2$. Figure 4.1 presents the flowchart of the image reconstruction method using positivity constrain.

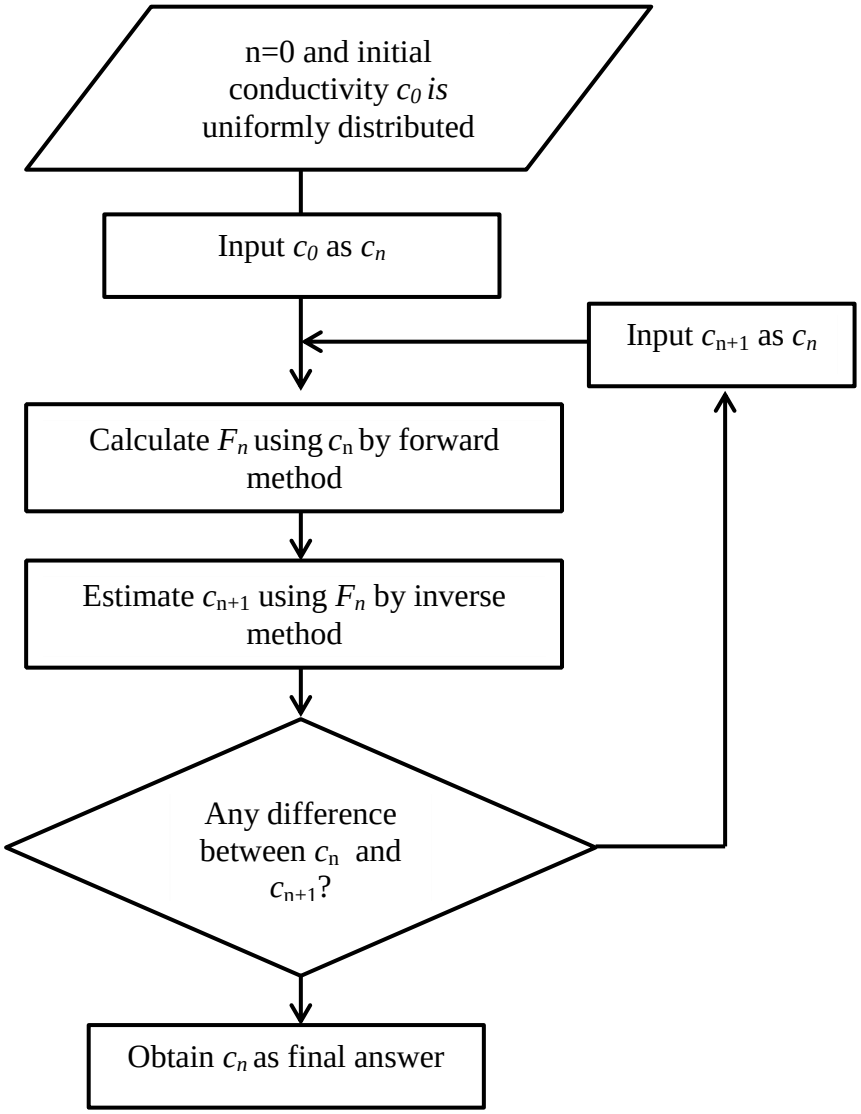

Figure 4.1 *Flow chart of the iterative reconstruction method using positivity constraint*

4.3.2 L-curve method

A variety of methods have been proposed for the estimating regularisation parameter λ such as discrepancy principle, error-estimation method, generalised cross validation (GCV) and the L-curve criterion (Hansen, 1998). L-curve criterion is selected for analysing our EIM image reconstruction with the following reasons:

1) Ideally prior assumption should be considered in inverse calculation, however it is not possible to estimate exactly how much noise is embedded in the recorded data. Similar with GCV, L-curve criterion does not use the level of noise explicitly in calculation, and is suitable for reconstructing data recorded from a complex electronic system.

2) In the comparison between GCV and L-curve criterion (Hansen, 1998), L-curve criterion never leads to large errors while GCV occasionally does. L-curve criterion consistently over-smooths whereas under-smoothing, which can terminate iteration process, does not happen. Thus L-curve criterion is more suitable for iterative process of non-linear problem.

Tikhonov Regularization replaces the solution of a linear system by the minimisation problem with a suitable value of regularisation parameter λ.

$$min\{\|Ax-b\|^2 + \lambda^2\|x\|^2\} \tag{4.19}$$

and the minimisation problem has an unique solution,

$$x = (A^TA + \lambda^2 I)^{-1}A^Tb \tag{4.20}$$

Let matrix A be of dimension $m \times n$ with $m \geq n$, and the singular value decomposition (SVD) of A is given by $\sum_{i=1}^{n} u_i \sigma_i v_i^T$, the regularised solution x_λ becomes,

$$x = \sum_{i=1}^{n} f_i \frac{(u_i^T b)}{\sigma_i} v_i \tag{4.21}$$

where f_i are the Tikhonov filter factors, which depends on σ_i and λ as

$$f_i = \frac{\sigma_i^2}{\sigma_i^2+\lambda^2} \simeq \begin{cases} 1, & \sigma_i \gg \lambda \\ \sigma_i^2/\lambda^2, & \sigma_i \ll \lambda \end{cases} \tag{4.22}$$

The solution and residual norms for x_λ in terms of the SVD are,

$$\|x\|_2^2 = \sum_{i=1}^{n}(f_i \frac{u_i^T b}{\sigma_i})^2 \quad (4.23)$$

$$\|Ax - b\|_2^2 = \sum_{i=1}^{n}((1 - f_i)u_i^T b)^2 \quad (4.24)$$

The two terms form the basis for L-curve analysis. By plotting the log values of these two terms, an L-shape curve should be obtained. The optimal regularization parameter usually lies on the corner, where the "perturbation error" and "regularization error" is balanced.

When the inverse problem is solving data measured on uniform conductivity distributions, the L-curve is L shaped and has one corner. But when the inverse problem is solving data measured on a breast model, the L-curve has two corners and is not in L shaped (Figure 4.2). According to Hanson's description, the single corners for the L shape curves are "global corners" (Hansen *et al.*, 2007). For models with non-uniform conductivity distribution an extra "local corner" will exist (Figure 4.3) and the curve is labelled as a problematic L-curve.

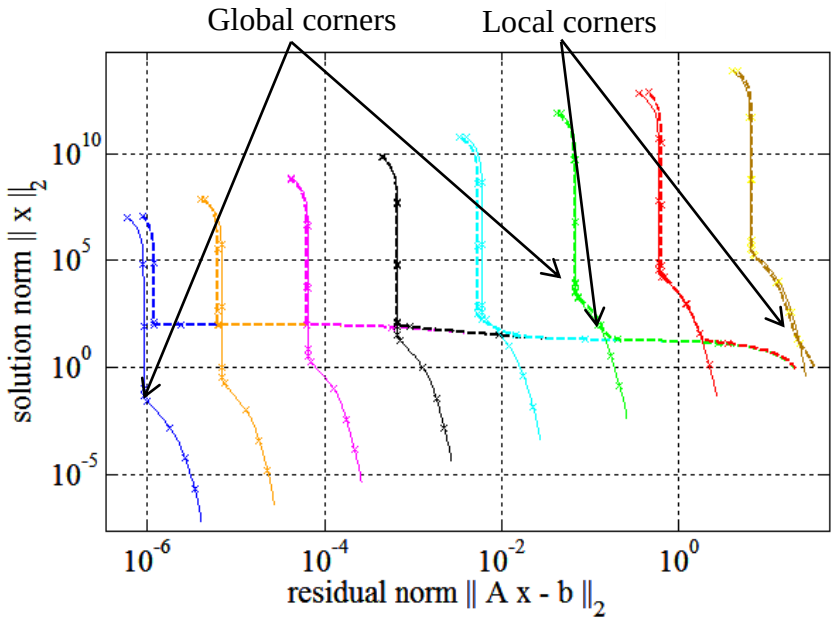

Figure 4.2 *L-curves for simulated models. Different colours from left to right represent different simulated signal to noise level in the measurement data set, which are accordingly in 0, 140, 120, 100, 80, 60, 40, 20dB. Two types of lines represent two models: solid line is uniform conductivity distribution, dotted line is breast model.*

Empirically, regularization parameters on the “global corners” are too small for reconstructing noise-added problems. The choice between “global corner” and “local corner” becomes critical. We observed that, “local corners” are changeable with different conductivity distributions. As such we assume the locations of “local corners” are depending on the measuring object, and we should choose regularization parameters from the “local corners”.

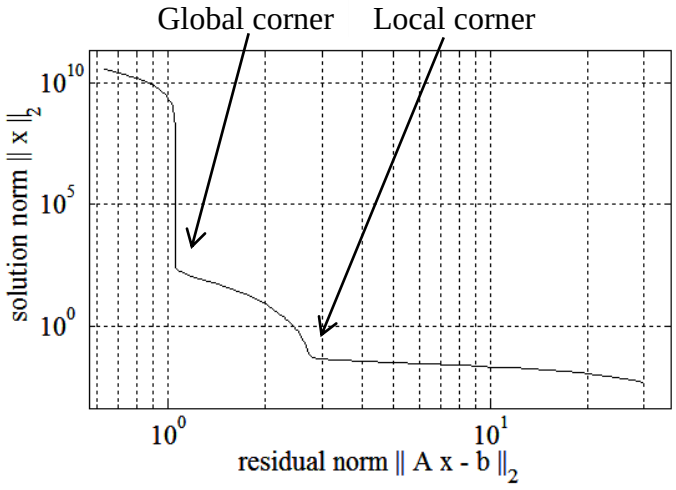

Figure 4.3 *Global corner and Local corner on the L-curve that generated from a non-uniform conductivity distribution.*

In summary, L-curve method estimates the regularization parameter that balances the errors between signal and regularization. It also depends on the design, such as electrode configuration or boundary position, of the EIM system.

4.3.3 Depth dependent regularization

In order to compensate sensitivity for regions in weak signal, the depth dependent regularization method is developed to increase regularization. Regularization parameter λ obtained from the L-curve method is multiplied by a factor taking into account the depth of a particular layer, such that regularization parameter is updated by the equation

$$\lambda' = f(d) \times \lambda \tag{4.25}$$

Figure 4.4 shows a uniform conductivity distribution model. By forward calculation (without regularization) an initial conductivity distribution is obtained. As the layer locates further away from the electrode plane are less sensitivity and the

values of reconstructed conductivity are smaller. From this we take the mean conductivity value of each layer, divided by the mean conductivity value in the first layer (which is the layer attaching to the electrode plane) to obtain the compensation factors.

$$f(d) = \bar{c}_d / \bar{c}_1 \tag{4.26}$$

The compensation factors ranged from zero to one, whereas the factor is always 1 for first layer. A smaller compensation factor reduces the level of regularization, so that the reconstructed conductivity values would be increased.

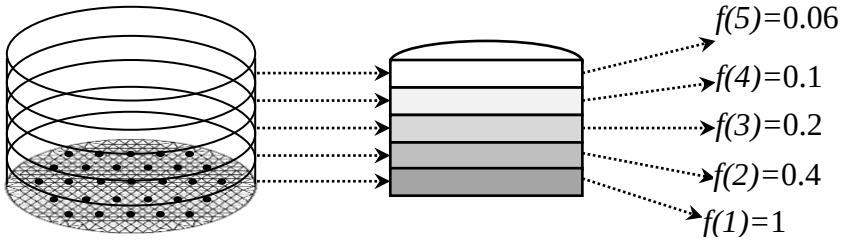

Figure 4.4 *Example compensation factors for layers in different depths*

Regularisation parameter λI from equation (4.18) then becomes a diagonal matrix (Figure 4.5) constructed by *(d x m)* diagonal elements, where *d* is the number of layers in the 3D mesh, and *m* equals to the number of elements in each layer. The first *m* diagonal elements belongs to the first layer and their value equal to $f(1)$ x λ, where λ is the output from the L-curve method. Then the next *m* diagonal elements have value of $f(2)$ x λ, and so on until the last m diagonal elements with value $f(d)$ x λ.

$$\begin{bmatrix} f(1,1)\times\lambda & 0 & 0 & 0 & 0 & 0 & 0 & 0 \\ 0 & \ddots & 0 & 0 & 0 & 0 & 0 & 0 \\ 0 & 0 & f(1,m)\times\lambda & 0 & 0 & 0 & 0 & 0 \\ 0 & 0 & 0 & f(2,1)\times\lambda & 0 & 0 & 0 & 0 \\ 0 & 0 & 0 & 0 & \ddots & 0 & 0 & 0 \\ 0 & 0 & 0 & 0 & 0 & f(2,m)\times\lambda & 0 & 0 \\ 0 & 0 & 0 & 0 & 0 & 0 & \ddots & 0 \\ 0 & 0 & 0 & 0 & 0 & 0 & 0 & f(d,m)\times\lambda \end{bmatrix}$$

Figure 4.5 *The regularization parameter λ in matrix form.*

4.4 Simulated experiment

Simulated experiment has been designed for testing the performance of the modified image reconstruction algorithm. The image quality for the two algorithms, with and without enforcing the positivity constraint, is compared by using the reconstructed absolute conductivity images from a simulated experiment. The model was set up as a human breast with a malignant object. Both algorithms are implemented with the L-curve method and depth dependent regularization methods that we proposed in the previous section. Analysis and discussion are as follows.

4.4.1 Settings

A simulated breast model has been constructed as Figure 4.6. It is simulating a human breast dipped into the measurement tank of the Sussex EIM Mk4 system. The breast is being compressed and attaching to the base plane, where electrodes are embedded into. The 4cm thick breast model is being evenly divided into four layers. The 3D mesh that is constructed by triangular elements is presented in figure 6. Two types of tissues in a human breast, namely adipose and connective tissues, were used to build this breast model. According to the distribution of colour elements in Figure 4.7, conductivity of connective tissue, adipose tissue and background saline are respectively 0.8 mS/cm, 0.6 mS/cm and 0.5 mS/cm. In such, layer one is pure adipose tissue surrounded by saline. Layer two to layer four are identical with connective tissue dominated at the central area surrounded by adipose tissue, and a thin layer of saline surrounding the breast model.

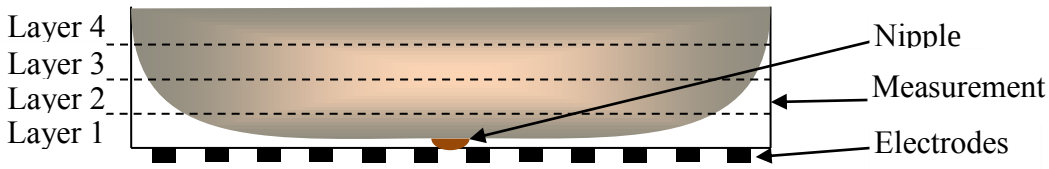

Figure 4.6 Side view of a simulated breast model dipped in the measurement tank

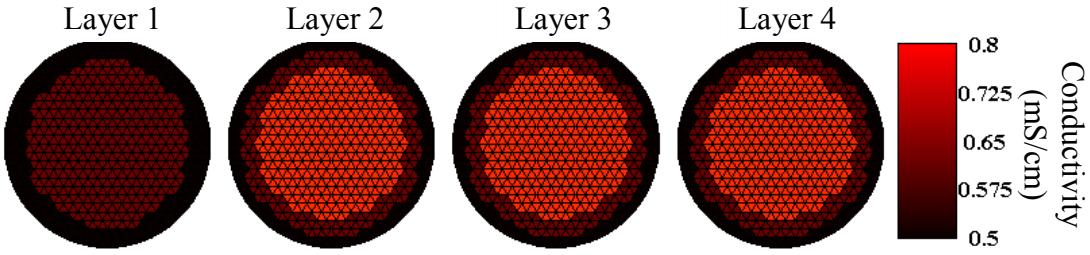

Figure 4.7 The 4 layers 3D mesh simulating breast model

In order to examine the ability of the image reconstruction algorithm for the diagnosis of breast cancer, an object simulating malignant tissue was set in three different models, that the malignant object is located at three different depths, which are in layer 2, layer 3 and layer 4 respectively. The horizontal position of the object is shown in figure 4.8.

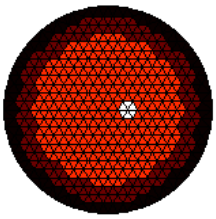

Figure 4.8 *Location of the malignant object*

The conductivity of the malignant object is 2.4 mS/cm, which is three times the conductivity of normal connective tissues. Thus the ratio of conductivity between adipose, connective and malignant tissues is 0.75 **:** 1 **:** 3, according to the *in-vitro* result (Jossinet, 1998) that measured conductivities of human breast tissues at frequency 50 kHz.

The images were reconstructed with both noise-free data and noise-added data. Two types of reconstruction errors are calculated for each reconstructed 3D image, definitions are as below:

$$\text{Image reconstruction error} = mean(|c_i - c_{0i}|) \qquad (i = 1 \sim N) \qquad (4.27)$$

$$\text{Region of interest error} = 1 - \frac{\max(c)}{c_0} \qquad (4.28)$$

Image reconstruction error measures the mean deviation (Kenney *et al.*, 1962) induced from all pixels of 3D image. It compares the differences between the original conductivity model and reconstructed conductivity distribution. The conductivity distribution c is subtracted by the original conductivity distribution c_0 pixel by pixel, to convert all values into positive then take the mean. It is described by equation (4.27), N is the total number of elements in the 3D mesh.

Region of interest error measures how much the object in the region of interest degraded through the reconstruction process. It uses peak conductivity to measure

error. The peak conductivity of measuring object could be affected by weak sensitivity region of the EIT system, or too strong regularization.

4.4.2 Results for noise-free data

The reconstructed images for noise-free simulation are shown in below figures. Figure 4.9 shows the results reconstructing the model with object in the layer 2, Figure 4.10 in layer 3 and Figure 4.11 in layer 4. In each figure, the top row images are reconstructed by the traditional modified Newton-Raphson method (MNR) without using positivity constraint (POS) and bottom row images are reconstructed with positivity constraint (POS). The vertical location of layers 1 to 4 could be referred to Figure 4.5.

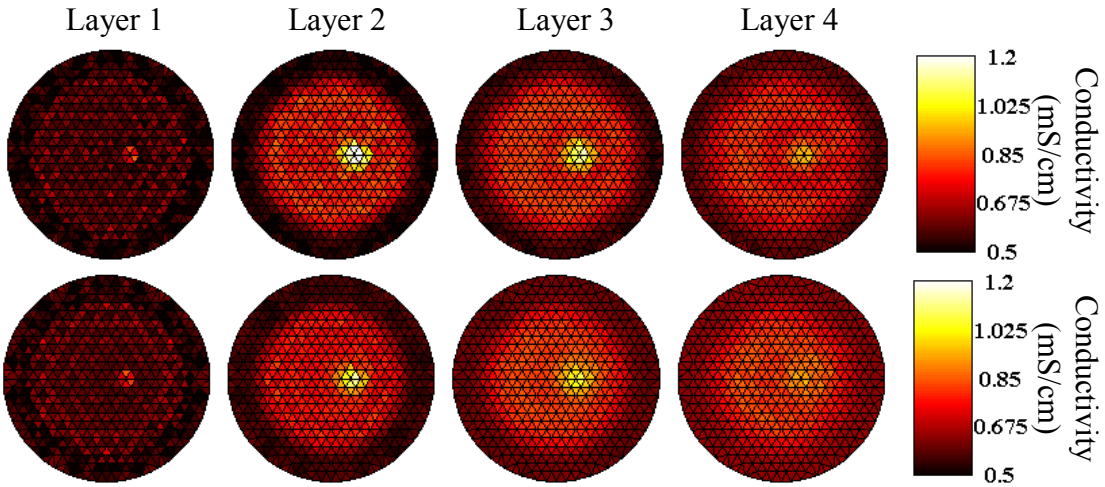

Figure 4.9 *Reconstructed image for model with object in layer 2. Top row images were reconstructed only by MNR. Bottom row images were reconstructed with POS.*

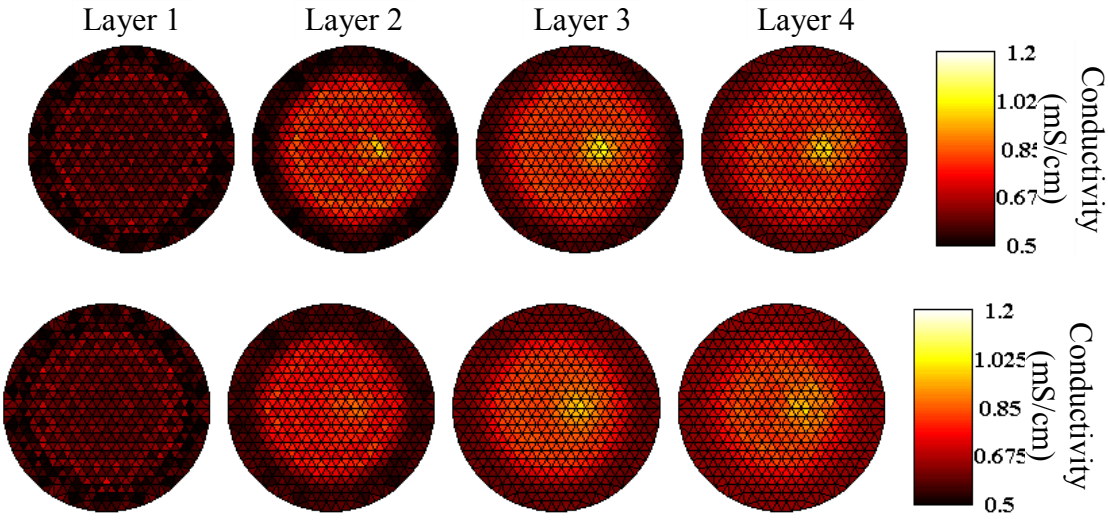

Figure 4.10 *Reconstructed image for model with object in layer 3. Top row images were reconstructed only by MNR. Bottom row images were reconstructed with POS.*

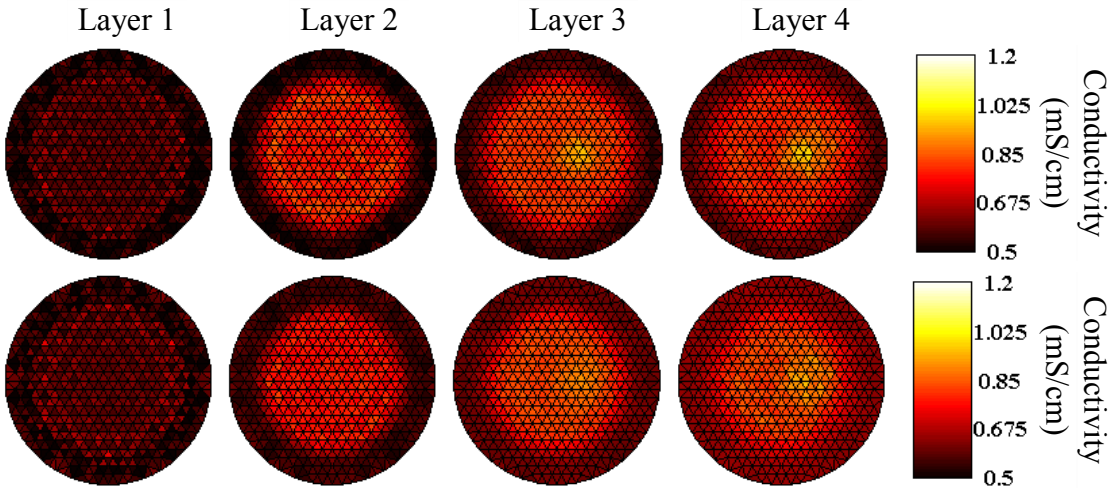

Figure 4.11 *Reconstructed image for model with object in layer 4. Top row images were reconstructed only by MNR. Bottom row images were reconstructed with POS.*

4.4.3 Results for noise-added data

The reconstructed images for 60dB noise-added simulation are shown in Figure 4.12, 4.13 and 4.14.

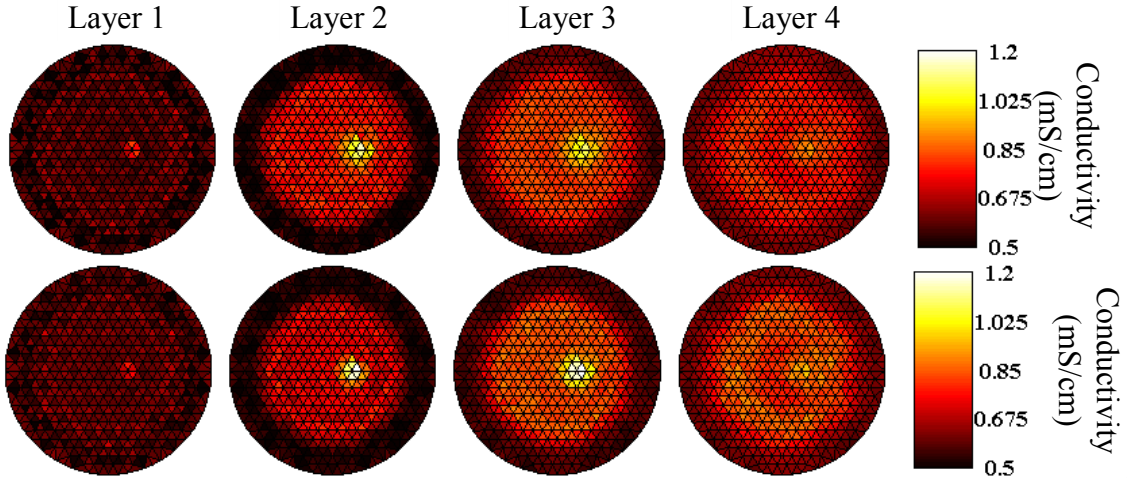

Figure 4.12 *Reconstructed 60dB model with object in layer 2. Top row images were reconstructed only by MNR. Bottom row images were reconstructed with POS.*

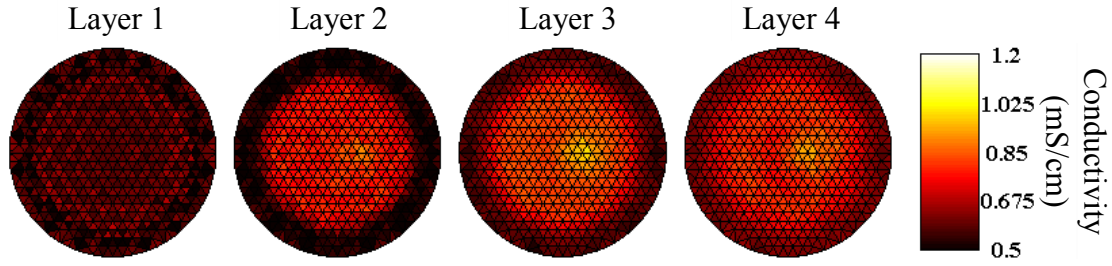

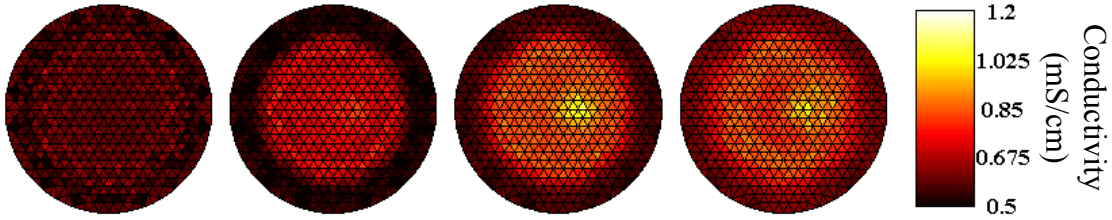

Figure 4.13 *Reconstructed 60dB model with object in layer 3. Top row images were reconstructed only by MNR. Bottom row images were reconstructed with POS.*

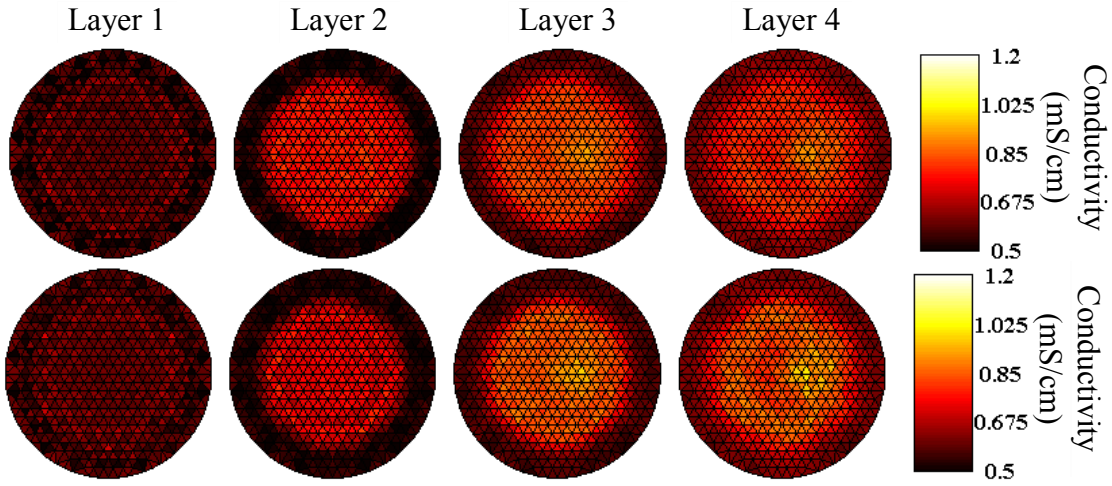

Figure 4.14 *Reconstructed 60dB model with object in layer 4. Top row images were reconstructed only by MNR. Bottom row images were reconstructed with POS.*

4.4.4 Discussion

The errors

The conductivity images captured in Figures 4.9 to Figure 4.11 are reconstructed from simulated noise-free data. Comparing between MNR and POS, the object reconstructed by MNR has higher conductivity and sharper boundary. Statistically, table 4.1 listed the image reconstruction errors. The values of MNR are generally lower than POS from the noise-free section. Table 4.2 listed the region of interest errors. The values of MNR are also lower than POS from the noise-free section.

One of the reasons is that, over-smooth image happens if the additional regularization constraint enforcing is a smoothing function, and POS is a smoothing function. Accuracy can be reduced if regularization is enforced to ideal data set. However, regularization is necessary because returning signal is not ideal in reality. The existence of noise increases the ill-posedness of the problem and enforcing

regularization constraint is the only solution of iterative image reconstruction method, thus error will be relatively higher without regularization.

The conductivity images captured in Figures 4.12 to 4.14 are reconstructed from simulated 60dB noise data. We obtained an opposite result here. From the images, we can see the object reconstructed by POS is clearer than MNR. Statistically, the image reconstruction errors and region of interest errors from POS images are lower than MNR images. The accuracy of POS is relatively higher than MNR. It shows that MNR is incapable to solve with noisy problems, and it is necessary to enforce additional constraint when reconstructing noisy data.

From the images, we found the peak values are located on layer that the object is originally located on, which shows that the proposed depth dependent regularization method can produce promising results on calibrating geometry distortion of depth. Note that uniform measurement data is the only a-priori information used to define the depth dependent parameters and the method can also be applied to reconstruction image for data set that measuring an unknown model.

Table 4.1 *The image reconstruction errors*

Image reconstruction error		Object on layer 2	Object on layer 3	Object on layer 4
Noise free	MNR	0.1137	0.2451	0.2759
	POS	0.1943	0.2818	0.3011
SNR 60dB Noise added	MNR	0.1909	0.2793	0.3286
	POS	0.1353	0.2284	0.2692

Table 4.2 *The region of interest errors*

Peak conductivity error		Object on layer 2	Object on layer 3	Object on layer 4
Noise free	MNR	0.4259	0.5728	0.5929
	POS	0.5269	0.5908	0.6014
SNR 60dB Noise added	MNR	0.5216	0.5882	0.6125
	POS	0.4502	0.5545	0.5824

From Table 4.1 the image reconstruction error of POS in noise free images is higher than noise-added images. Same result can be found in Table 4.2 and this is because the regularization parameters that selected automatically by the depth

dependent regularization method are not optimized. Further test has been done to verify this. For the reconstruction of noise-free object on layer 2 using POS method, if the depth dependent regularization parameters are replaced by the noise-added parameters, the image reconstruction error will be reduced to 0.1116, which is still less than the error produced by MNR, yet is better than the noise-added result. Further discussions about the regularization are written below.

Regularization estimation

From the above discussion, the regularization estimation seems to be producing over-smoothing of regularization parameters for the noise-free data by using POS method. Table 4.3 listed all regularization parameters estimated by the L-curve and depth dependant methods. Note that the regularization parameters of MNR and POS that are estimated by the L-curve cannot be compared since their solution equations are different.

Table 4.3 *The estimated regularization parameters*

	Object in layer	L-curve	Depth dependent regularization			
			Layer 1	Layer 2	Layer 3	Layer 4
MNR (noise-free)	2	0.00047283	1	0.70216	0.44383	0.33137
	3	0.00047283				
	4	0.00047283				
POS (noise-free)	2	0.001164	1	0.66828	0.38626	0.27196
	3	0.001164				
	4	0.001164				
MNR (60dB noise)	2	0.017763	1	0.28794	0.1289	0.08864
	3	0.016767				
	4	0.017616				
POS (60dB noise)	2	0.0030477	1	0.24434	0.091132	0.054947
	3	0.0028706				
	4	0.0030539				

The regularization parameters estimated by L-curve method ensure the reconstructed images to be converged through iterations. Table 4.4 listed the image reconstruction errors through iterations for the noise-free images. We can see the values are converging and almost stable after 5 iterations.

Similar results are obtained for the 60dB noise simulation as listed in Table 4.4 and Table 4.5. Results in these two tables show that L-curve method ensures stable solution.

Table 4.4 *Image reconstruction error through iterations for noise-free simulation*

Iteration	MNR Layer 1	MNR Layer 2	MNR Layer 3	POS layer 1	POS Layer 2	POS Layer 3
1	0.1441	0.2585	0.2828	0.2147	0.2701	0.2932
2	0.1120	0.2461	0.2789	0.2008	0.2803	0.3003
3	0.1140	0.2452	0.2753	0.1966	0.2819	0.3013
4	0.1137	0.2451	0.2761	0.1952	0.2818	0.3011
5	0.1137	0.2451	0.2759	0.1947	0.2818	0.3011

Table 4.5 *Image reconstruction error through iterations for 60dB noise simulation*

Iteration	MNR Layer 1	MNR Layer 2	MNR Layer 3	POS layer 1	POS Layer 2	POS Layer 3
1	0.2029	0.2822	0.3308	0.1664	0.2312	0.2501
2	0.1902	0.2806	0.3292	0.1472	0.2354	0.2657
3	0.1909	0.2792	0.3286	0.1407	0.2308	0.2687
4	0.191	0.2794	0.3286	0.138	0.2293	0.269
5	0.1909	0.2793	0.3286	0.1368	0.2287	0.2691

In general, the proposed regularization methods enhance the accuracy of reconstructed images from noise-added data. The methods estimate regularization parameters for individual measurement data. The methods ensure the reconstructed conductivity distribution is converging through iteration, and the target object is located in the correct depth.

One problem we may have to tackle is that the regularization estimated for noise free data may produce over-smoothed image. Further investigation is needed.

4.5 Summary

This chapter presented the image reconstruction and regularization method we used for processing data measured by the Sussex EIM Mk4 System. Based on the modified Newton-Raphson algorithm, three regularization methods have been proposed to reconstruct 3D breast images. The first method is the positivity constraint method, which is customized for reconstructing human breast images by

providing a smoothing regularization function for the image reconstruction process. It ensures iterative image reconstruction can be converged even with noisy data. The second method L-curve was found to be suitable for searching the optimal regularization parameter. Such the regularization parameter can be estimated automatically but not empirically. The third method, depth dependent regularization defines different levels of regularization for different layers. The location of reconstructed images show great improvement as it correctly depicts the location of the reconstructed object, and the weak sensitivity problem from the far end of the electrode plane has been corrected. As the noise added to the simulated data is simulating noise we obtained from clinical trial, the results from this study are generally satisfying our needs in processing clinical data.

CHAPTER 5 COMBINED RING-PLANAR ELECTRODE CONFIGURATION FOR A CLINICAL 3D ELECTRICAL IMPEDANCE MAMMOGRAPHY SYSTEM

This chapter proposes the specifications of a modified clinical 3D EIM system based on the achievements and experiences gained from the previous versions of clinical EIM Systems. A simulation study is conducted to show the improvement on sensitivity for the modified electrode configurations.

Chapter 5.1 reviews electrode configurations of the published EIM systems, and the two EIM systems, De Montfort EIM Mk2 system and Sussex EIM Mk4 system, that was developed by the Sussex Biomedical Engineering research group. Section 5.2 evaluates of the clinical trial results of Sussex EIM Mk4 system and revisits the key targets of an ideal EIM system. Chapter 5.3 derives the EIT sensitivity matrix by using the Gezelowitz's approach and introduces the sensitivity analysis method for configuring EIT boundary measurement and electrode position. Chapter 5.4 brings out the details of the ring electrode and planar electrode configurations by listing the current injection patterns and sensitivity matrix analysis. Chapter 5.5 presents the benchmark of an ideal EIM system which adapted the Combined Ring-Planar (CRP) electrode configuration. Current injection patterns and sensitivity analysis are presented. Chapter 5.6 is a comparison between the new CRP configuration and the previous configurations. Results are being discussed, followed by chapter 5.7 with summary.

5.1 Introduction

Early clinical Electrical Impedance Tomography (EIT) systems (Barber *et al.*, 1984; Jossinet, 1988; Griffiths *et al.*, 1989; Cook *et al.*, 1994) were designed for 2-D imaging. It was assumed that the injected current through the ring of electrodes around the body surface was confined into a 2-D plane. In reality, current is flowing in 3 dimensional way and the potential distribution should be calculated in the same way. In the 90s, more EIT research were based on 3D models as there was a need to

increase accuracy and image resolution. Classic studies, such as the reconstructed 3D images based on multiple ring electrodes measurement (Metherall *et al.*, 1996), complete electrode model based on 3D finite element method (P. J. Vauhkonen *et al.*, 1999), and planar electrode design (Cherepenin *et al.*, 2001), have made great contribution to the EIT community.

The 3D EIT technique has been prospected well for breast cancer detection. Although more research groups are involved in the development of Electrical Impedance Mammography (EIM) system, and the first clinical EIM system (Assenheimer *et al.*, 2001) has been commercialized in 2000, no promising clinical EIM images could be published because of the difficulties found from clinical trials. To tackle those difficulties and to propose an optimal system design became the goals of the Biomedical Engineering Research Group.

This chapter first reviews several EIM systems including two EIM systems that were developed by the Biomedical Engineering Research Group. Problems are listed out which were based on our experience through clinical trials. Then the principle of sensitivity matrix is introduced, which brings into the design of the proposed optimal electrode configuration with new drive and receive patterns. A simulation is conducted to compare the sensitivity performance between the previous and proposed system.

5.2 Background

This section is a review on various EIM systems. The advantages and limitations are briefly analysed for each system.

5.2.1 Various EIM systems

In breast imaging, the first commercialized clinical EIM system is the T-Scan™ technology TS2000 system (Assenheimer *et al.*, 2001), which was developed in Israel (Piperno *et al.*, 1990) and commercialized in year 2000. It is a 3D EIM system with embedded electrodes on the flat surface of a hand-held probe (figure 5.1) (Voges *et al.*, 2006). The system is ideal for real time breast screening because of its compact size, and multiple images can be obtained by moving the probe and used to

verify the analysis result. However, the distances between electrodes are limited due to the small hand probe surface area, because of this, the depth of the injected current is limited which in turn weakens the sensitivity to the region underneath.

Figure 5.1 *The TS2000 scan probe*

The Moscow research group developed another 3D EIM system (Cherepenin *et al.*, 2001) that applies planar electrode configuration. 3D breast images are reconstructed, that each layer of the 3D image is parallel to the electrode plane (figure 5.2). From the latest result (Trokhanova *et al.*, 2008), the mastopathy and other non-cancerous diseases of the mammary gland can be diagnosed by using the averaged conductivity of each layer but not pixel by pixel.

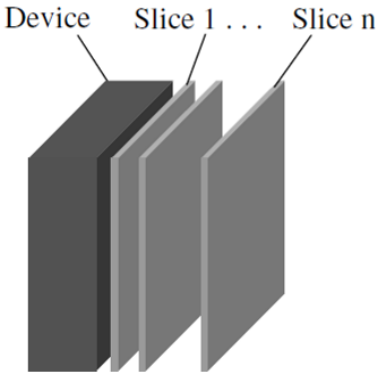

Figure 5.2 *Layers of 3D breast image*

The Rensselaer Polytechnic Institute research group developed the 4th generation of Adaptive Current Tomography (ACT4) system as Electrical Impedance Spectroscopy System (Saulnier *et al.*, 2007) for breast cancer detection. One major investigation is on the adaptive method Gisser *et al.* (1987) in data collection, that currents are injected simultaneously through all planar electrodes into the object while voltage on each electrode is measured. This method, also named as

the optimal current method, gives a perfect uniform current distribution and the best distinguishability. It is a very competent method of data collection.

Figure 5.3 *The ACT4 instrument*

The Dartmouth research group developed their Electrical Impedance Tomography Spectroscopic (EITS) system (Hartov *et al.*, 2000) using circular array configuration. The electrodes are mounted on a radially translating interface which couples them to the breast through direct contact, a conductive gel is applied to the surface of the electrodes to improve coupling and reduce the high impedance of the skin. Results (Osterman *et al.*, 2000) show that, normal breasts usually produce smooth images, while malignancies tend to have inhomogeneous images.

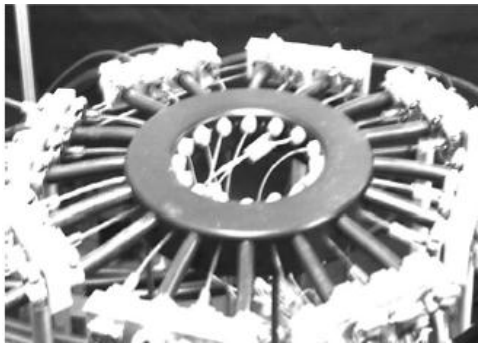

Figure 5.4 *Electrodes of the EITS system*

From the publication regarding these 3D EIM systems for the screening of breast cancer, there are two major groups of electrode configurations. One is the ring electrode configuration which arranges electrodes in circular shape, usually multiple sets of data are acquired because each set of data could only produce one 2D image.

As such multiple slices of images could be combined to form a 3D image. Another configuration is the planar electrode configuration which usually fixes electrodes on a plane such as hand-held probe. The breast is compressed during data collection, and 3D breast image can be reconstructed by using one set of acquired data.

Two clinical EIM systems have been developed by the Biomedical Engineering Research Group as in-vivo breast screening tools, and were introduced as below:

5.2.2 The De Montfort EIM Mk2 system

The development of the De Montfort EIM Mk2 system (Wang *et al.*, 1998) (figure 5.5) started in 1998 in Leicester, UK. The system adopts the ring electrodes configuration and using back-projection algorithm to reconstruct 2D human breast conductivity image.

Figure 5.5 *The De Montfort EIM Mk2 System*

For the ease of clinically use, electrodes were embedded inside a tailor made brassiere. The system was reported as a novel design by the UK journalists as the device is portable and could be installed even in small surgeries, not necessarily in big hospitals. Comparing De Montfort EIM Mk2 to the other breast screening techniques such as biopsy and CT, the data acquisition process is painless, rapid, non-invasive and clean. The system adopts the 32 ring electrodes configuration, but since the electrodes are fixed inside a bra, multiple layers screening was not allowed, thus only one slice of 2D image can be produced for each breast. Besides, as fabric-based electrodes are used, contact impedance problem exists and cause systematic

artefacts in the reconstructed images. In Dartmouth's EITS system, the same problem happens but they solved the problem by using conductivity gel as the contacting media between electrodes and the skin. Cable length was another problem because capacitances differs between cables and this increase the difficulties in data calibration.

5.2.3 The Sussex EIM Mk4 System

The Sussex EIM Mk4 system (Tunstall *et al.*, 2010) (figure 5.6) is the first 3D EIM system developed by the research group. The EIM Mk2 system has only considered imaging of distributions of resistance varying in two dimensions, the Sussex EIM Mk4 system is designed specifically for genuine 3D imaging. There are two major modifications, namely the utilisation of a saline tank and the application of planar electrode configuration.

Figure 5.6 *The Sussex EIM Mk4 System*

The saline tank design adopted the wet electrode technique (Wang *et al.*, 2007). Saline was acting as the contact medium between electrodes and the skin of breast. This significantly minimises the contact impedance problem found from previous versions of systems which applied dry electrode design (Wang *et al.*, 2007). The system requires patient to lie on the measurement trolley and dip one of her breast into the saline tank for acquiring data. In such, the patient could be relaxed and her body stabilized during data collection process to avoid errors induced by body movement. The electrodes are fixed on the bottom plane of the scan-head, and the volume of the saline tank could be adjusted by ascending or descending the bottom plate for accommodating breasts of different cup sizes. Comparing to the previous

version, the size of the system is bigger because of the saline tank and the hydraulic system that supporting warm saline for every measurement. Installation could be a problem for small surgeries as it occupies more space.

The planar electrode configuration was generally applied in other 3D EIM systems such as the T-Scan™ system, the Moscow's 3D EIM system and the ACT4 system. The Sussex EIM Mk4 system has an unique feature - electrodes are evenly distributed in hexagonal shape. The 120^{o} rotatable current injection and voltage measurement patterns and confines data acquisition to strong signals (please refer to chapter 3 for details). Besides the sensitivity problem always relate to the distance between electrodes and the object. The central region would have the weakest sensitivity for ring electrode configuration, geometry distortion can happen in the direction from the central to the boundary. For planar electrode configuration, sensitivity drops along the direction from the electrode plane. Although geometry distortion problem through the X-Y plane (2D) was solved, it still exists through the Z plane (3D). There was calibration study (please refers to chapter 4) in the depth direction, but still the overall performance of the system could not be met as expected.

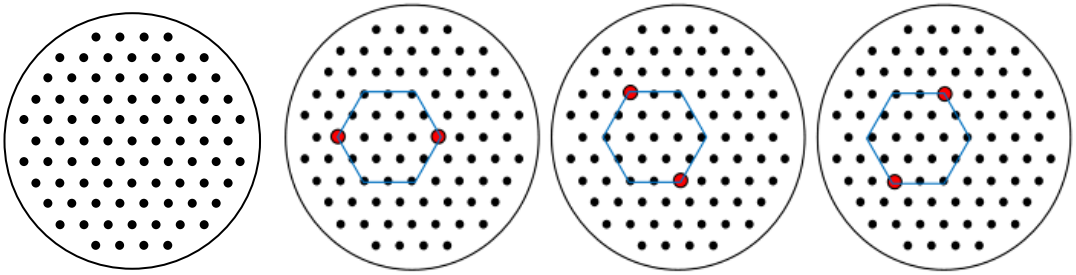

Figure 5.7 *(a) Electrodes are evenly distributed in hexagonal shape and, (b) The 120^{o} rotatable current injection and voltage measurement patterns*

The first clinical trial was started in 2009 at the Oxford Radcliffe Hosptial, UK and data were collected by using the Sussex EIM Mk4 system. The results were encouraging as the 3D breast images were found to be more stable and having a higher resolution comparing with the 2D breast images that produced by previous EIM systems. Clear benign and malignant objects can be shown from the clinical results (please refers to chapter 5).

5.3 Achievements, difficulties and evaluations

This section summarized the achievements we obtained and the difficulties we encountered from the two EIM systems that were developed by the Biomedical Engineering Research group. Those experiences, especially the difficulties, are valuable because most of them are the real problems we will encounter from the clinical trials. A summary is given to compare the achievements and difficulties to the research targets of our research group for the development of EIM system, this helps us in proposing the specification of an optimal clinical EIM system.

5.3.1 Achievements

The De Montfort EIM Mk2 system

The size of De Montfort EIM Mk2 system is compact in comparing to typical clinical screening devices such as CT and MRI. As we can see from figure 5.5, the system consists of a set of computer, a control box and the brassiere. In addition, the manufacturing cost of the system is low, and it would be possible for the system to become clinical regular check-up tools that are owned by GP surgeries and potentially benefit more people.

The image reconstruction process is rapid and can be used as real-time breast screening tools. The electrodes were embedded into a brassiere, which is physical and psychologically comfortable to patients. As such breast screening procedure would not be a painful experience anymore.

The Sussex EIM Mk4 system

Accuracy has definitely been improved since the device was using 85 planar electrodes, which increased the number of independent measurement and was a very important factor for the inverse calculation.

Also, repeatability is increased by the using of saline tank in measuring body impedance as contact impedance error has been greatly reduced.

Breast images are reconstructed three dimensionally thus the image resolution is increased. At the same time, 2D images are reconstructed by using back-projection for previewing and real time analysis.

The system does not require huge space compared to other clinical screening technologies such as X-ray, MRI and CT. The whole system was installed in a small room of the Oxford Radcliffe Hospital. As a clinical screening tool, the machine was clean and safe which satisfied the clinical hygiene and safety requirements.

5.3.2 Difficulties

The De Montfort EIM Mk2 system

The weak sensitivity in the central region is the major problem, which is the same for all EIT systems that use the ring electrode configuration. There are two approaches to increase the sensitivity. One is to reduce the size of the ring, which means to reduce the distance between electrodes and the object. Another approach is to optimize the electrodes current driving and voltage receiving patterns (Webster, 1990). For drive and receive pattern, such as adaptive method, could give the best sensitivity but it costs more to develop electronic devices for injecting current through all electrodes simultaneously.

The electrode-skin contact impedance is another problem, which is due to an electrochemical effect between the electrodes and the skin, and it causes voltage to drop at each electrode. The contact impedances depends on the thickness and properties of the skin, therefore the voltage changes are different at each electrode-skin interface. The system uses four electrodes data acquisition method which can reduce the error, but the problem still exists as the electrodes are in direct contact to the skin. Another method is to consider the errors as unknown parameters in the image reconstruction (Kolehmainen *et al.*, 1997).

The Sussex EIM Mk4 system

Although sensitivity is evenly distributed and strong near the electrode plane, results showed that sensitivity drops significantly at the depth around 3cm. The detection of abnormal tissues in such depth became unstable as the signal noise is relatively higher. This is the main problem we experienced from the Mk4 system as it has been designed with the planar electrode configuration.

There are random noises that only occur in clinical environment such as patient movement. This can also cause random artefacts to the images. The system need to be designed with higher endurance to those random noises.

Physiological and anatomical variation between patients is another problem. Conductivity changes with the woman's menstrual cycle and adipose tissue density in the breast. Until now no published calibrating method could be found to correct these errors, and we believe more sample data is necessary to develop a suitable calibration method.

We encountered the air bubble problem in the clinical trials. In normal practice, a patient should lie on the trolley in prone position and dip one of her breast into the saline tank. The breast does not touch the electrodes on the bottom plane directly because there is 1-2mm spacing between the electrode-skin interfaces to avoid contact impedance problem. However air can be trapped in this space, which causes resistivity to the measurement. The problem has been solved by adding some channels so that air can escape when the breast is pressing downwards (Huber *et al.*, 2010). This can ensure that the space between the breast and the electrodes can be uniformly filled with saline.

5.3.3 Evaluation

Sensitivity was found to be the major problem for both systems. From simulation we can prove that sensitivity should not be a problem in noise-free environment but it is not realistic. But even noise added simulation connot reflect the reality because the white noise added in the simulated data is different from the systematic noise that may cause relatively large artefacts to the images. We found

that, those artefacts mainly appear in the weak sensitivity regions. To the stronger sensitivity regions, the image quality is absolutely fine.

To tackle this, we tried to enforce constraints in image reconstruction to compensate signal in weak sensitivity regions, but results showed that the differences between normal and abnormal tissues could be lost by the regularization of noises. Thus, sensitivity should be enhanced from the root by changing the electrode configuration so that the system can have stronger sensitivity throughout the whole measuring volume.

Below is a summary of conclusions we drew from all the experience we gained so far and the proposals we put forward for the development of the next generation's EIM system.

1. Sensitivity must be increased in order to:
    a. Detect smaller cancerous tissue
    b. Detect cancerous tissue in weaker sensitivity regions, such as the central region from the circular boundary and the in-depth region from the bottom plane.
    c. Enhance the endurance to systemic noise
2. We suggest to keep using the saline tank because wet electrodes can effectively solve the contact impedance problem.
3. It is good to use both 2D and 3D image reconstruction methods:
    a. Although the resolution of 2D image is lower than 3D image, 2D image reconstruction is fast (less than 1 second) and is ideal for as previewing images for clinical application.
    b. Average reconstruction time for each set of 3D breast images is long (around 15 minutes), but 3D images have a much higher resolution than 2D images, and therefore 3D images are better for locating abnormal tissues.

4. More clinical sample data is needed in order to:

    a. Build a database that defines different kinds of cancerous breast tissue.

    b. Develop method that could eliminate the variation between patients.

Since increasing sensitivity seems to be the most important issue, studies were carried out on a modified electrode configuration and the details of which will be presented in the following sections.

5.4 Method

This section introduces the sensitivity relationship of between conductivity and voltage measured by four electrodes method. An optimal electrode configuration was proposed for breast cancer detection based on the derived sensitivity relationship.

5.4.1 The sensitivity matrix

In EIT measurement, a series of potential difference on a surface are measured to calculate the conductivity of a closed volume. The relationship between the measured potential difference and the conductivity of the closed volume can be described by the Geselowitz's reciprocal theorem (Geselowitz, 1971) listed in chapter 2 equation (2.48):

$$g_p = -\int_{\Omega} c_p \nabla\phi_u \cdot \nabla\psi \mathrm{d}v \tag{5.1}$$

The matrix form can be written as

$$g_p = Sc_p \tag{5.2}$$

where g_p is a vector of measurement, and c_p is a vector of image element.

Each element of the sensitivity matrix S is given by

$$S_{ij} = -\int_{ith\ pixel} \nabla\phi(c) \cdot \nabla\psi(c) \mathrm{d}v \tag{5.3}$$

$\nabla\phi(c)$ is the field across the i^{th} pixel element produced by the current through the j^{th} drive pair. $\nabla\psi(c)$ is the field that would be developed across the element if a unit current were driven between the j^{th} receive pair.

If the elements are tetrahedral, the fields are uniformly distributed across the element and the discrete form of sensitivity matrix becomes

$$S_{ij} = \nabla\phi(c) \cdot \nabla\psi(c) \cdot A \tag{5.4}$$

where A is the volume of the i^{th} tetrahedral element.

5.4.2 Sensitivity analysis

From equation 5.4, the sensitivity of the i^{th} element (with conductivity c) is calculated by integrating of the multiplication of two potential gradients $\nabla\phi(c)$, $\nabla\psi(c)$ and the element volume dv. $\nabla\phi(c)$ is induced across the element by injecting current through the j^{th} drive pair, and $\nabla\psi(c)$ is induced across the element by injecting current through the j^{th} receive pair. Dotted lines in figure 5.8 are the field lines generated by the j^{th} drive pair and j^{th} receive pair. According to the Coulomb's law, when current is injecting constantly by an electric dipole, the field strength is dependant on the position of the i^{th} pixel element and governed by $C/(d_p * d_n)$, where C is a constant, d_p is the distant between element and positive electrode, and d_n is the distant between element and negative electrode. As stated by Geselowitz's reciprocal theorem, the drive and receive pair take the same measure to the sensitivity, then sensitivity on the i^{th} element when acquiring the j^{th} frame could be presented by

$$S_{ij} \propto {}^{1}/_{(d_{i,j1} * d_{i,j2} * d_{i,j3} * d_{i,j4})} \tag{5.5}$$

where $d_{ij1..ij4}$ are the distances between the i^{th} pixel element and the four electrodes the $j1$ to $j4$ respectively.

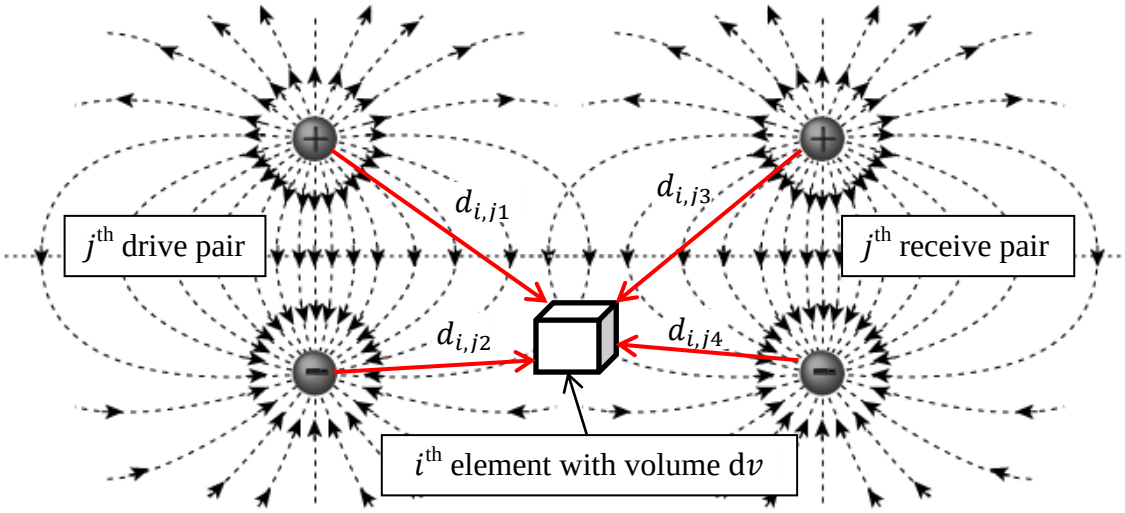

Figure 5.8 *Sensitivity depends on the distances between element and the four electrodes*

Equation (5.5) could be applied to a 3D mesh and enforced with particular electrode configuration to examine the sensitivity on each node.

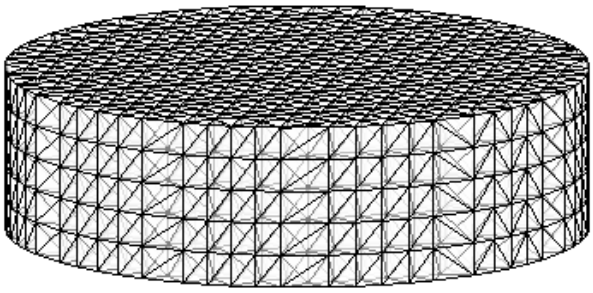

Figure 5.9 *A 3 layers 3D mesh simulating the saline tank*

Consider a 3D mesh that simulates the saline tank (figure 5.9). The mesh is in circular shape with diameter in 18 cm. The height of the mesh is 5cm and is divided into 5 layers that consist of uniform tetrahedral elements. There are 11700 elements and are connected by 2526 nodes. For each current injection and voltage measurement pattern and one node, one sensitivity value can be calculated. For each possible current injection and voltage measurement pattern, a node has a vector of sensitivity values. In this study, the L2 norm of this vector is used as a quantified index for the sensitivity of the corresponding node, and it is calculated by equation (5.6):

$$S_i = \sqrt{\sum_{j=1}^{P} \left| {}^{1}/_{(d_{i,j1} * d_{i,j2} * d_{i,j3} * d_{i,j4})} \right|^2} \qquad (5.6)$$

where P is the total number of the drive and receive patterns.

Ring electrode configuration

For the ring electrode configuration, 32 ring electrodes are placed to surround the circular tank in 1cm depth. The adjacent drive and receive pattern is applied, which is the same as the pattern applied for the De Montfort EIM Mk2 system. The sensitivity of each node are calculated by equation (5.6). The values are normalized and plotted in as a 3D graph in figure 5.10 left. The darker dots are having higher sensitivity to the drive and receive pattern, and the plotted figure looks like a doughnut (figure 5.10 right). It is clear that sensitivity in central region is relatively weaker.

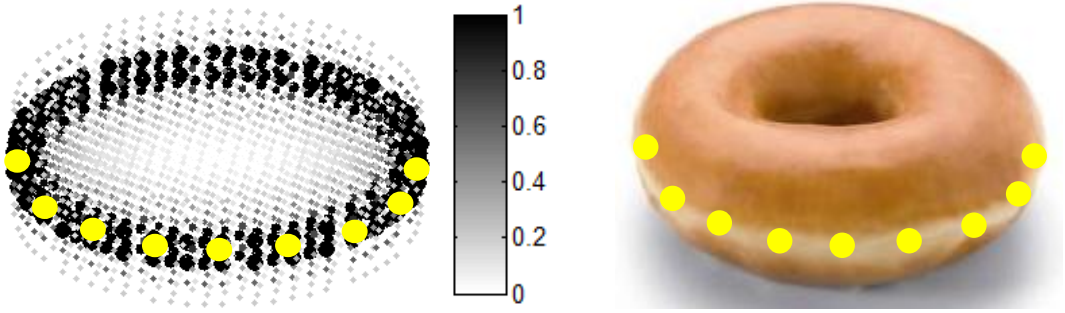

Figure 5.10 *Nodes sensitivity graph for ring electrode configuration (left) and a doughnut for comparison (right). Yellow dots indicate the electrodes.*

Planar electrode configuration

85 electrodes are placed at the bottom of the 3D mesh in hexagonal shape (as shown in figure 5.7). The drive and receive pattern of the Sussex EIM Mk4 system is applied. The overall sensitivities on each node are calculated by equation (5.6). Results are normalized and plotted in figure 5.11 left. The higher sensitivity region looks like a dome (figure 5.11 right). Sensitivity is relatively weaker in region further away from the bottom plane. Sensitivity is also weaker near the circular boundary.

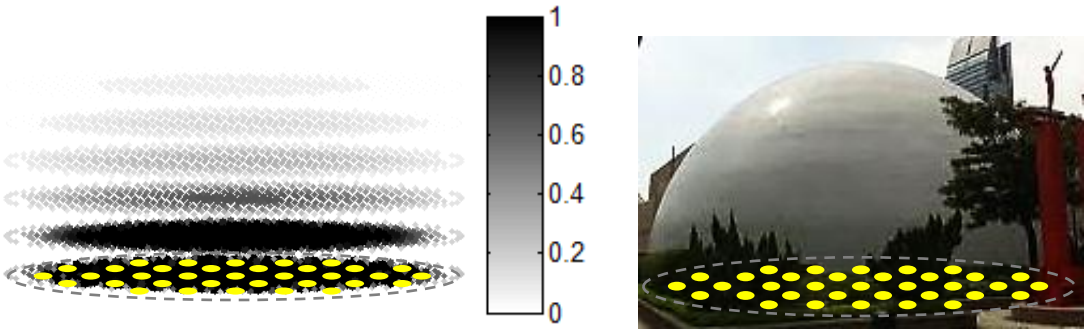

Figure 5.11 *Nodes sensitivity graph for planar electrode configuration (left) and a dome for comparison (right). Yellow dots indicate the electrodes.*

In the detection of breast cancer, if the breast is in a saline tank and in the flattened shape (as shown in figure 5.12), the required high sensitivity region is indeed at the centre of the saline tank (the red region surrounded by the dotted red line). From figure 5.10 and 5.11 we can see that, neither ring nor planar electrode configurations could produce good sensitivity on the target region. In order to optimize the sensitivity of breast cancer detection by using EIM technique, a novel electrode configuration with customized drive and receive pattern is proposed in next section.

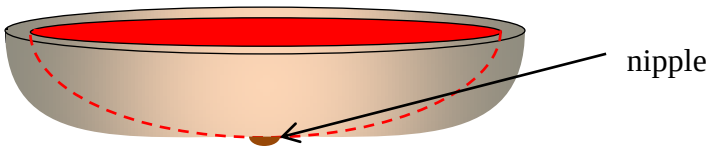

Figure 5.12 *Flattened human breast and the required sensitive region (dotted red line)*

5.4.3 The Combined Ring and Planar (CRP) electrode configurations

To compensate the weak sensitivity problems, an optimal electrode configuration is proposed which combines the ring and the planar electrode configurations into one configuration. It combines the strength of ring and planar electrode configurations, maximising the sensitivity for the region with high probability of breast cancer. It is based on the planar electrode configuration of the Sussex EIM Mk4 system, which has 85 electrodes at the bottom plane of a saline tank, plus the ring shaped 36 electrodes at the boundary of the saline tank (as shown in figure 5.13). The 36 electrodes are located at 1cm below the top of the saline tank. The electrodes are highlighted in blue in figure.

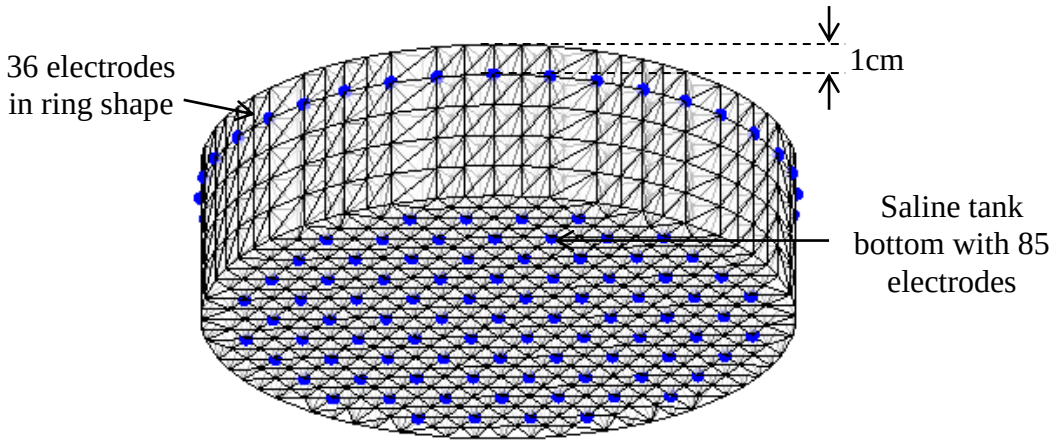

Figure 5.13 *Combined Ring and Planar (CRP) electrode configuration. Electrodes are fixed on the bottom plane and near to the top boundary of the circular saline tank*

The combined ring and planar (CRP) electrode configuration is novel and it has not been used by other EIM systems. It is specifically customized for the human breast using wet electrode technique to achieve a lower noise-level. It inherits the achievements of the Sussex EIM Mk4 system, and it aims to improve sensitivity on the centre region.

5.4.4 Drive and Receive Patterns

The current injection and voltage measurement (drive-receive) patterns of the CRP electrode configuration is build upon two sets of drive-receive patterns.

Firstly, the drive-receive pattern for the 85 electrodes on the bottom plane is the same to that used by the Sussex EIM Mk4 system. The pattern has 123 pairs of current driving electrodes. When a current is injected to a pair of electrodes, voltage will be measured by the neighbouring 9 – 12 pairs of electrodes. There are a total 1416 drive-receive patterns.

The second drive-receive pattern is for the 32 ring electrodes where we use the opposite electrodes drive-receive method since it has the highest sensitivity at the centre (Kauppinen, 2006). There are 36 pairs of drive electrodes, and they are located opposite to each other. Each pair of driving electrodes has 33 pairs of receiving electrodes. Each pair of the receiving electrodes are neighbouring to each other.

5.5 Simulation study

The performance of the CRP electrode configuration is compared to the ring electrode configuration and planar electrode configuration using sensitivity analysis methods. A 5 layer 3D model has been constructed for comparing the differences between two images reconstructed by planar and the CRP electrode configurations.

5.5.1 Sensitivity Analysis

The sensitivity distributions of ring, planar and CRP electrode configurations are plotted against region of interests in figures 5.14, 5.15 and 5.16, respectively. The region of interests moves from the centre (0cm from centre) to the boundary (9cm from centre). The 6 curves in each figure represent region of interest on different layers, and the 1^{st} layer represents the layer closest to the bottom of the saline tank.

Figure 5.14 plots the sensitivity distribution for the ring electrode configuration. Sensitivity of each layer decreases from the boundary of the saline tank to the centre. The electrodes are actually located on the 5^{th} layer, which has the highest sensitivity. The sensitivity of the 4^{th} layer and the 6^{th} layer overlap to each other. This could be explained by the symmetrical geometry from the electrodes of the two layers. For the lowest layer, there is an exception where a small decrease in sensitivity is found near the boundary, which may suggest less current is passing through this region.

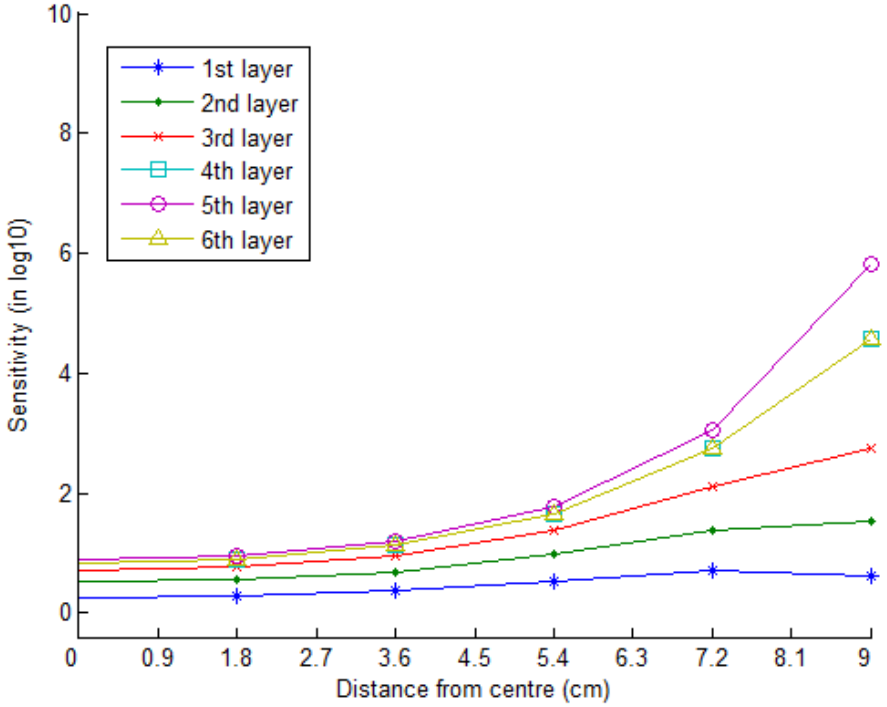

Figure 5.14 *Sensitivity distributions for ring electrode configuration*

Sensitivity is plotted in logarithm scale. The sensitivity of most layers decrease rapidly near the saline tank boundary. The most dramatic drop is found from the 5^{th} layer where electrodes are located. The sensitivity decrease 10^5 times from the boundary to the centre. It is difficult to detect an object when it is near to the centre of the saline tank.

Figure 5.15 plots the sensitivity distribution for the planar electrode configuration. Sensitivity in all layers drops from the centre to the boundary. Within each layer, sensitivity does not drop as much in the ring electrode configuration, but the sensitivity differences between different layers are huge, which is almost 10 times. Sensitivity at the centre is higher as the number of electrodes near saline tank boundary is relatively less than the centre. Note that sensitivity decreases with layers and the drop is in logarithm scale, which may suggest that sensitivity in upper layer is extremely weak, such as the boundary of the 6^{th} layers where the value is below 2.

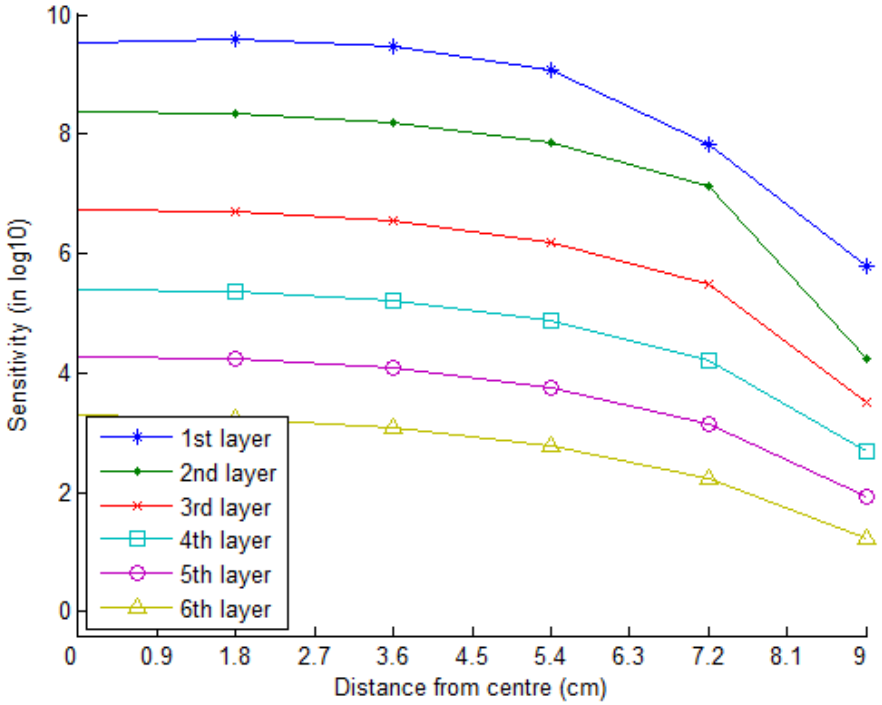

Figure 5.15 *Sensitivity distributions for planar electrode configuration*

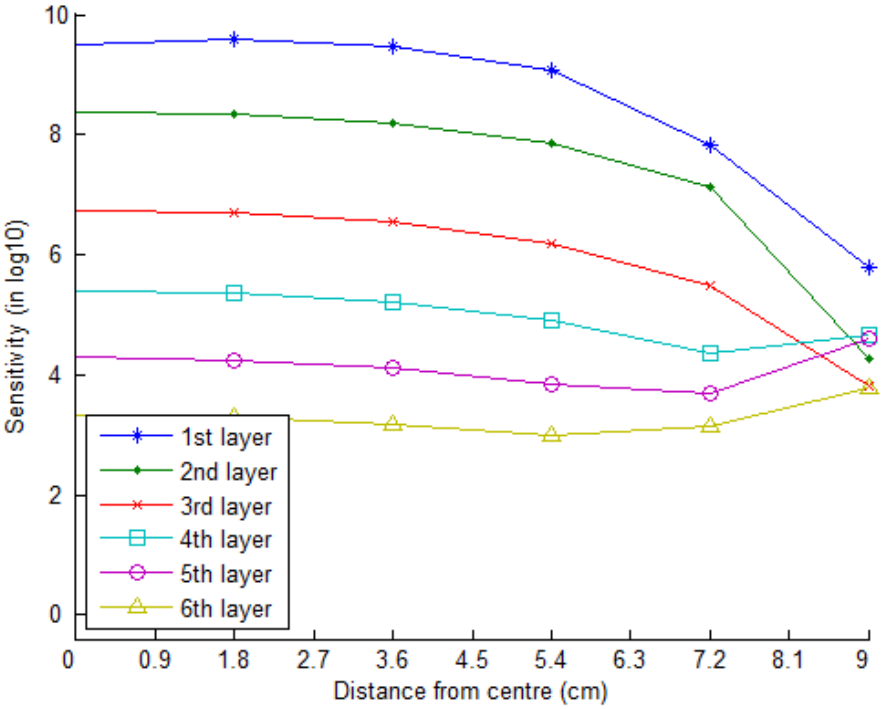

Figure 5.16 *Sensitivity distributions for CRP configuration*

Figure 5.16 plots the sensitivity distribution for the CRP electrode configuration. Generally there is no change for the sensitivity in the first three layers, the additional ring electrodes affect the sensitivity of the top three layers only. For top three layers, there is an obvious increase of sensitivity around 2cm near the

boundary. Since the electrodes are located on the 5th layer, the highest sensitivity increase by about 100 times. Sensitivity on the 4th and the 6th layer has also increased by 10 times.

These figures show that CRP configuration could improve sensitivity for the elements close to the boundary of the three layers close to the ring electrodes.

Furthermore, sensitivity at each node is calculated using equation (5.6), and the node sensitivity graph is plotted as figure 5.17. Comparing to the planar electrode configuration (figure 5.11 left), the values at the top three layers are generally higher, and significant improvement can also be found at the boundary of the top three layers.

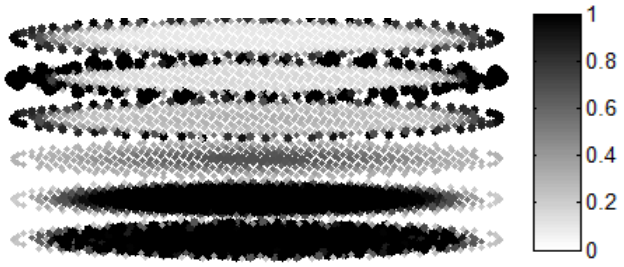

Figure 5.17 *Nodes sensitivity for the CRP electrode configuration.*

5.5.2 Reconstructed images

Figure 5.18 shows the simulated model with three objects in each layer. It is a simulation using three rods inserted into the saline tank. The background conductivity is 0.5mS/cm, and the conductivity of the 3 rods is homogeneous and is 0.55mS/cm, which is 10% higher than the background conductivity.

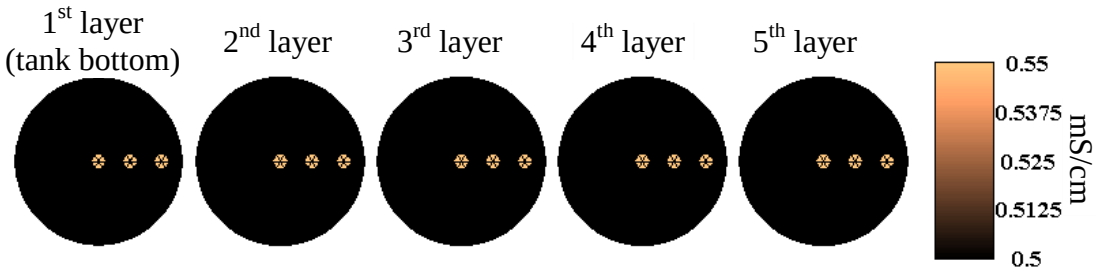

Figure 5.18 *The simulated model with three objects in each layer.*

The set up of the 3D mesh is same as 5.13, which is having 18cm diameter and in 5cm depth. The mesh is split vertically into 5 layers, such that depth of each layer equals 1cm. The diameter of each of the rods is 1.4cm.

Images are reconstructed using the modified Newton-Raphson algorithm. Identity matrix is used as regularization matrix, and the regularization parameter is defined using the L-curve method that we have introduced in chapter 4. 60dB white noise has been added to the simulation to simulate real environment.

There are two set of results for comparison. One set is reconstructed using the planar electrode configuration, and the other is reconstructed using the CRP electrode configuration. The reconstructed images are shown in figure 5.19.

For the reconstructed images with the planar electrode configuration, the rods start to fade out from the 3rd layer and nearly disappeared in the 5th layer. The sensitivity is weak on the layer located 4cm away from the electrode plane. For the reconstructed images with the CRP electrode configuration, the object near the boundary of the 4th and the 5th layers can still be seen, however the signal for the object at the centre of the 5th layer is as weak as the planar electrode configuration.

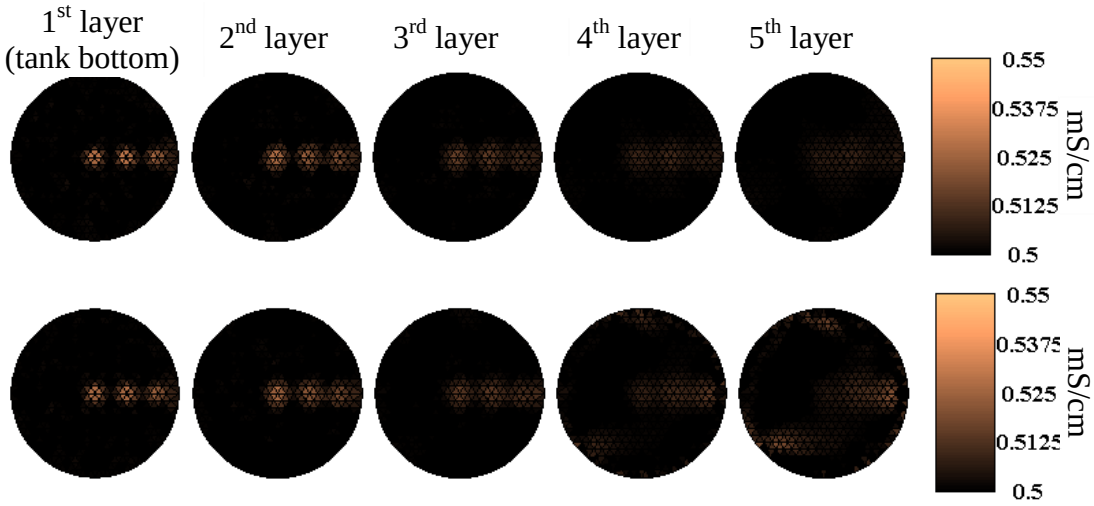

Figure 5.19 *The reconstructed images (middle row – planar electrode configuration, bottom row – CRP electrode configuration).*

Note that two clusters of artefacts could be found from the 5th layer the images with the CRP configuration. That could be an amplification of noise by the ring electrode configuration, as sensitivity is relatively higher near the boundary of the 4th and 5th layers.

5.5.3 Discussion and conclusion

Overall, the CRP electrode configuration shows improvement when we compare the results to the ring electrode configuration and to the planar electrode configuration. The sensitive regions of ring electrode configuration and planar electrode configuration have a different shape. Sensitivity analysis results show that the sensitive regions of individual electrode configuration can be combined by using the CPR design.

The regions further away from the bottom electrode plane and the ring electrodes are still suffering from the weak sensitivity problem. If the system is used by a patient with larger breast size, the depth of the saline tank increase, and the region between the ring and the planar electrodes would still suffering from the weak sensitivity problem. To solve this, we may have to add additional ring, or using a different drive-receive pattern.

The drive-receive patterns studied so far are four-electrodes method, other current-drive method are not discussed in the study. Method such as the optimal current method (Webster, 1990), which generates uniform current distribution by injecting current of appropriate magnitude through all the electrodes, can be useful as sensitivity can be increased further. More flexible design, such as injecting current from the top ring and measuring voltage by the electrodes on the bottom plane simultaneously, can also enhance the system performance in an effective way.

5.6 Summary

This chapter reviews various EIM systems and evaluates the Sussex EIM Mk4 system and the De Montfort EIM Mk2 system. Conclusions are drawn from the strength and weakness analysis of the two systems. Feasibility study of a new electrode configuration, which combines the ring and planar electrode configurations (CRP), is presented to increase the sensitivity in breast cancer detection. The performance between ring, planar and CRP electrodes configuration are compared using sensitivity analysis and simulated image reconstruction. It shows that sensitivity can be increased near the additional ring electrodes.

CHAPTER 6 CONCLUSIONS AND FUTURE WORK

This chapter concludes the achievement and difficulties from the research works discussed in previous chapters. Also gives suggestions for future work.

6.1 Conclusions

The research addressed in this thesis has been directed at:

1. Developing imaging and analysing techniques for the Sussex Mk4 EIM system

2. Investigating methods to improve sensitivity to detect abnormal breast tissue

For the development of imaging and analysing techniques for the Sussex Mk4 EIM system, the research work is concluded as below:

The functionalities of the Sussex Mk4 EIM system, such as the use of "wet" electrode configuration and planar electrode configuration, have been introduced. Sensitivity of the system, particularly on its data acquisition method by using the 85 electrodes design, has been analysed by comparing between the simulated and agar experimental results. Results showed that stable signal was returned from the system. The simulated and experimental results show similarity on the object position and conductivity distribution, that the object was found to be in the original position but sensitivity becomes weak at a depth of 4.5 cm far from the electrode plane. The sensitivity in far end of the electrode plane would need to be enhanced.

Image reconstruction and regularization methods have been studied in order to improve sensitivity in the far end region, and also to provide the application in clinical use. The "one-click" functionality is important for clinical application, as the users know nothing about EIT. The software should produce meaningful clinical images. The image reconstruction and regularization methods have to be standardized such that systematic noise and physiological / anatomical variations between patients have to be eliminated from the resulting images.

To achieve the above requirements, investigation of the image reconstruction algorithm has been carried out. Positivity constraint has been enforced in the image reconstruction algorithm to ensure enough endurance to the systematic noises. A simulated 3D breast model has been constructed for testing. Results show that image reconstruction error decreased when the reconstruction is regularized by the positivity constraint in noise-added environment. L-curve method has been selected to estimate optimal regularization parameter from the measurement data. This method balances perturbation error and regularization error automatically such that the reconstruction calculation can be an automated process. The depth dependent regularization method has been implemented. It shows great improvement as it correctly depicts the location of the reconstructed object, which corrected the weak sensitivity problem from the far end of the electrode plane. However some images have been over-smoothed in noise-free environment and this requires further investigation.

The development of image analysis method has been carried out to automate the breast cancer diagnosis process. The Cole-Cole theory has been revisited, which brings out the method to diagnose breast cancer based on the electrical properties of human breast tissues. Several problems in EIM image analysis are listed out, that a new method named “Ratio Difference Frequency” (RDF) imaging is proposed to tackle these problems. The method was first tested by a phantom experiment using biological and non-biological objects. The biological object (apple) has been successfully extracted from the mixed (with agar) model by using the RDF method. Then 13 sets of clinical test data were used for testing. As the RDF imaging method extract different types of tissue by using the tissues’ rate of change of conductivity between two frequencies, specific tissue is supposed to be extracted in certain ranges of frequency. From this assumption, we found the adipose tissue can be extracted between frequencies of 20 kHz and 50 kHz, while malignant tissue can be extracted between higher frequencies, which are 2 MHz and 5 MHz. Out of the 13 data sets, 10 of them were diagnosed as healthy and 3 of them contain malignant tissues from the RDF images. The results exactly match to the clinical diagnosis from the X-ray mammogram images. The result is encouraging and proved that the Sussex Mk4 EIM system is capable to detect breast cancer.

Further studies have been conducted to improve sensitivity of the system. The studies are based on sensitivity analysis to modify electrode configuration of the EIM system. Currently there are two major groups of electrode configurations. One is the ring electrode configuration and the other is the planar electrode configuration. Each of them has their strength and weak sensitivity regions. Studies showed that, by combining both design, the strength of individual sensitivity regions can also be combined. It is a preliminary study of sensitivity analysis for particular electrode configuration and current injecting and voltage measuring pattern. The development of the software has been completed and ready to be used as a tool for investigating sensitivity with other configurations.

6.2 Future work

Base on the studies of this thesis, there are three suggested area for researchers to follow:

6.2.1 Optimizing current driving and voltage receiving pattern

As mentioned in chapter 5, it was suggested to study on other current driving and voltage receiving patterns. So far the patterns studied are four-electrodes method, and the CRP electrode configuration actually provides a flexible space for the development of current driving and voltage receiving pattern. Current could be flowing from the ring electrodes to the planar electrodes, or using the adaptive current injection method, injecting current simultaneously from multiple electrodes to obtain uniform current distribution to increase sensitivity in the central region.

6.2.2 Estimating regularization parameter

Regularization method depends on the electrode configuration. So it was suggested to study after finding the optimal current driving and voltage receiving pattern. As mention in chapter 4, although the combined regularization methods that using positivity constraint, L-curve and depth dependent method can estimate regularization parameters based on the quality of incoming data, the regularization method still have chance to over-smooth certain area of the 3D image. Further study is suggested especially in the use of L-curve.

Regularization can be loading dependent, because the common mode error mentioned in chapter 5 is loading dependent. Such noise could be eliminated by change the hardware (electronic) configuration, or it would become a difficult problem for the imaging software to handle with. It may be worth putting more investment in this area as it is seriously affecting the diagnosis ability of the system.

REFERENCE

Assenheimer, M., Orah, L.-M., Dov, M., David, M., Udi, N., Ron, N., & Abraham, S. (2001). The T-SCAN technology: electrical impedance as a diagnostic tool for breast cancer detection. *Physiol. Meas. , 22*, 1–8.

Avis, N. J., & Barber, D. C. (1995). Incorporating a-Priori Information into the Sheffield Filtered Backprojection Algorithm. *Physiol Meas., 16*, A111-A122.

Barber, D. C., Brown, B. H., & Freeston, I. L. (1983). Imaging Spatial Distributions of Resistivity Using Applied Potential Tomography. *Electronics Letters, 19*(22), 933-935.

Barber, D. C., & Brown, B. H. (1984). Applied Potential Tomography. *Journal of Physics E-Scientific Instruments, 17*(9), 723-733.

Barber, D. C., & Seagar, A. D. (1987). Fast reconstruction of resistance images. *Clin Phys Physiol Meas, 8 Suppl A*, 47-54.

Barber, D. C., & Brown, B. H. (1988). Errors in reconstruction of resistivity images using a linear reconstruction technique. *Clin Phys Physiol Meas, 9 Suppl A*, 101-104.

Barber, D. C. (1990). Quantification in impedance imaging. *Clin Phys Physiol Meas, 11 Suppl A*, 45-56.

Barber, D. C. (2000). Electrical Impedance Tomography. In Bronzino, J. D. (Ed.), *The Biomedical Engineering Handbook: Second Edition* (Vol. 68): CRC Press.

Barber, D. C. (2004). *EIT: The view from Sheffield*. Bristol and Philadelphia: Institute of Physics Publishing.

Bayford, R. H. (2006). Bioimpedance tomography (Electrical impedance tomography). *Annual Review of Biomedical Engineering, 8*, 63-91.

Bertolini, M., Nitrosi, A., Borasi, G., Botti, A., Tassoni, D., Sghedoni, R., & Zuccoli, G. (2011). Contrast detail phantom comparison on a commercially available unit. Digital breast tomosynthesis (DBT) versus full-field digital mammography (FFDM). *J Digit Imaging, 24*(1), 58-65.

Boone, K., Barber, D., & Brown, B. (1997). Imaging with electricity: report of the European Concerted Action on Impedance Tomography. *J Med Eng Technol, 21*(6), 201-232.

Breckon, W. R., & Pidcock, M. K. (1987). Mathematical aspects of impedance imaging. *Clin Phys Physiol Meas, 8 Suppl A*, 77-84.

Brown, B. H., & Seagar, A. D. (1987). The Sheffield data collection system. *Clin Phys Physiol Meas, 8 Suppl A*, 91-97.

Brown, B. H., Leathard, A. D., Lu, L., Wang, W., & Hampshire, A. (1995). Measured and expected Cole parameters from Electrical Impedance Tomographic Spectroscopy images of the human thorax. *Physiol Meas., 16*(Supp3A), 56-67.

Campbell, A. M., & Land, D. V. (1992). Dielectric properties of female human breast tissue measured in vitro at 3.2 GHz. *Phys Med Biol, 37*(1), 193-210.

Campbell, J., & Dimache, N. (2007). 3D EIT - MEIK in clinical application: observations and preliminary results. *World Congress on Medical Physics and Biomedical Engineering 2006, Vol 14, Pts 1-6, 14*, 3906-3910.

Chauveau, N., Hamzaoui, L., Rochaix, P., Rigaud, B., Voigt, J. J., & Morucci, J. P. (1999). Ex vivo discrimination between normal and pathological tissues in human breast surgical biopsies using bioimpedance spectroscopy. *Electrical*

Bioimpedance Methods: Applications to Medicine and Biotechnology, 873, 42-50.

Cheney, M., Isaacson, D., Newell, J. C., Simske, S., & Goble, J. (1990). NOSER: An algorithm for solving the inverse conductivity problem. *International Journal of Imaging Systems and Technology, 2*(2), 66-75.

Cherepenin, V. A., & Korjenevsky, A. V. (2000). United States Patent No. 6167300.

Cherepenin, V. A., Karpov, A. Y., Korjenevsky, A. V., Kornienko, V. N., Mazaletskaya, A., Mazourov, D., & Meister, D. (2001). A 3D electrical impedance tomography (EIT) system for breast cancer detection. *Physiol Meas, 22*(1), 9-18.

Cherepenin, V. A., Karpov, A. Y., Korjenevsky, A. V., Kornienko, V. N., Kultiasov, Y. S., Ochapkin, M. B., Trochanova, O. V., & Meister, J. D. (2002). Three-dimensional EIT imaging of breast tissues: system design and clinical testing. *IEEE Trans Med Imaging, 21*(6), 662-667.

Cole, K. S. (1940). Permeability and Impermeability of Cell Membranes for Ions. *Cold Spring Harbor Symposia on Quantitative Biology, 8*, 110-122.

Cole, K. S., & Cole, R. H. (1941). Dispersion and absorption in dielectrics I. Alternating current characteristics. *Journal of Chemical Physics, 9*(4), 341-351.

Cook, R. D., Saulnier, G. J., Gisser, D. G., Goble, J. C., Newell, J. C., & Isaacson, D. (1994). ACT3: a high-speed, high-precision electrical impedance tomograph. *IEEE Trans Biomed Eng, 41*(8), 713-722.

Dobbins, J. T. (2009). Tomosynthesis imaging: At a translational crossroads. *Medical Physics, 36*(6), 1956-1967.

Duffin, W. J. (1990). *Electricity and magnetism* (4th ed. ed.): McGraw-Hill.

Foster, K. R., & Schwan, H. P. (1989). Dielectric properties of tissues and biological materials: A critical review *Crit. Rev. Biomed. Eng. , 17*, 25-104.

Frerichs, I., Hahn, G., Schiffmann, H., Berger, C., & Hellige, G. (1999). Monitoring Regional Lung Ventilation by Functional Electrical Impedance Tomography during Assisted Ventilation. *Annals New York Academy of Sciences, Apr 20*(873), 493-505.

Gennaro, G., Toledano, A., di Maggio, C., Baldan, E., Bezzon, E., La Grassa, M., Pescarini, L., Polico, I., Proietti, A., Toffoli, A., & Muzzio, P. C. (2010). Digital breast tomosynthesis versus digital mammography: a clinical performance study. *European Radiology, 20*(7), 1545-1553.

Geselowitz, D. B. (1971). An application of elecvocardiographic lead theory to impedance plethysmography. *IEEE Trans Biomed Eng, BME-18*, 38-41.

Gisser, D. G., Isaacson, D., & Newell, J. C. (1987). Current topics in impedance imaging. *Clin Phys Physiol Meas, 8 Suppl A*, 39-46.

Griffiths, H., & Zhang, Z. (1989). A dual-frequency electrical impedance tomography system. *Phys Med Biol, 34*(10), 1465-1476.

Griffiths, H. (2001). Magnetic induction tomography. *Measurement Science & Technology, 12*(8), 1126-1131.

Hagness, S. C. T., Allen; Bridges, Jack E. . (1998). Two-Dimensional FDTD Analysis of a Pulsed Microwave Confocal System for Breast Cancer Detection: Fixed-Focus and Antenna-Array Sensors. *IEEE transactions on biomedical engineering, 45*(12, DECEMBER), 1470-1479.

Hahn, G., Dittmar, J., Just, A., Quintel, M., & Hellige, G. (2010). Different approaches for quantifying ventilation distribution and lung tissue properties by functional EIT. *Physiol Meas., 31*(8), S73-S84.

Halter, R. J., Hartov, A., & Paulsen, K. D. (2008). A broadband high-frequency electrical impedance tomography system for breast imaging. *IEEE Trans Biomed Eng, 55*(2 Pt 1), 650-659.

Hansen, P. C. (1992). Analysis of Discrete Ill-Posed Problems by Means of the L-Curve. *SIAM Review, 34*(4), 561-580.

Hansen, P. C. (1998). *Parameter-Choice Methods*. Philadelphia: SIAM.

Hansen, P. C., Jensen, T. K., & Rodriguez, G. (2007). An Adaptive Pruning Algorithm for the Discrete L-Curve Criterion. *J. Comput. Appl. Math. , 198*, 483-492.

Harrach, B., Seo, J. K., & Woo, E. J. (2010). Factorization method and its physical justification in frequency-difference electrical impedance tomography. *IEEE Trans Med Imaging, 29*(11), 1918-1926.

Hartov, A., Mazzarese, R. A., Reiss, F. R., Kerner, T. E., Osterman, K. S., Williams, D. B., & Paulsen, K. D. (2000). A multichannel continuously selectable multifrequency electrical impedance spectroscopy measurement system. *IEEE Trans Biomed Eng, 47*(1), 49-58.

Henry, C. L., Phyllis, E. J., William, W. B., & Glenn, I. L. (1985). Assessment of fat-free mass using bioelectrical impedance measurements of the human body. *The American Journal of Clinical Nutrition, 41*(APRIL 1985), 810-817.

Holder, D. S. (1992). Electrical impedance tomography (EIT) of brain function. *Brain Topogr, 5*(2), 87-93.

Holder, D. S. (2004). *Electrical Impedance Tomography*: Taylor & Francis.

Horesh, L. S., Martin; Bollhofer, Matthias; Douiri, Abdel; Holder, David S; Arridge, Simon R. . (2005). Multilevel Preconditioning for 3D Large-scale Soft-Field Medical Applications Modelling. *International Journal of Information and Systems Sciences, 2*(4), 532-556.

Hua, P. (1987). *Electrical impedance tomography in medicine.* PhD Preliminiary proposal, University of Wisconson, Madison.

Hua, P., Woo, E. J., Webster, J. G., & Tompkins, W. J. (1993). Finite-Element Modeling of Electrode Skin Contact Impedance in Electrical-Impedance Tomography. *Ieee Transactions on Biomedical Engineering, 40*(4), 335-343.

Huber, N., Béqo, N., Adams, C., Sze, G., Tunstall, B., Qiao, G., & Wang, W. (2010). *Further investigation of a contactless patient-electrode interface of an Electrical Impedance Mammography system*. Paper presented at the 10th International Conference on Biomedical Applications of Electrical Impedance Tomography (EIT 2009).

Isaacson, D. (1986). Distinguishability of Conductivities by Electric Current Computed Tomography. *Medical Imaging, IEEE Transactions on 5*(2), 91 - 95.

Jossinet, J. (1988). A hardware design for imaging the electrical impedance of the breast. *Clin Phys Physiol Meas, 9 Suppl A*, 25-28.

Jossinet, J. (1998). The impedivity of freshly excised human breast tissue. *Physiol Meas, 19*(1), 61-75.

Kao, T. J., Isaacson, D., Newell, J. C., & Saulnier, G. J. (2006). A 3D reconstruction algorithm for EIT using a handheld probe for breast cancer detection. *Physiol Meas, 27*(5), S1-11.

Kao, T. J., Boverman, G., Kim, B. S., Isaacson, D., Saulnier, G. J., Newell, J. C., Choi, M. H., Moore, R. H., & Kopans, D. B. (2008). Regional admittivity spectra with tomosynthesis images for breast cancer detection: preliminary patient study. *IEEE Trans Med Imaging, 27*(12), 1762-1768.

Kauppinen, P. H., Jari; Malmivuo, Jaakko (2006). Sensitivity Distribution Visualizations of Impedance Tomography Measurement Strategies. *International Journal of Bioelectromagnetism, 8*(1), VII/1 - VII/9.

Kenney, J. F., & Keeping, E. S. (1962). *Mathematics of Statistics* (Vol. 1): Princeton, NJ.

Kerner, T. E., Paulsen, K. D., Hartov, A., Soho, S. K., & Poplack, S. P. (2002). Electrical impedance spectroscopy of the breast: clinical imaging results in 26 subjects. *IEEE Trans Med Imaging, 21*(6), 638-645.

Kim, B. S., Boverman, G., Newell, J. C., Saulnier, G. J., & Isaacson, D. (2007). The complete electrode model for EIT in a mammography geometry. *Physiol Meas, 28*(7), S57-69.

Kolehmainen, V., Vauhkonen, M., Karjalainen, P. A., & Kaipio, J. P. (1997). Assessment of errors in static electrical impedance tomography with adjacent and trigonometric current patterns. *Physiol Meas, 18*(4), 289-303.

Kuen, J. W., E. J.; Seo, J. K. (2009). Multi-frequency time-difference complex conductivity imaging of canine and human lungs using the KHU Mark1 EIT system. *Physiol Meas, 30*(6), S149-164.

Kulkarni, R. B., Gregory; Isaacson, David; Saulnier, Gary J.; Kao, Tzu-Jen; Newell, Jonathan C. . (2008). An Analytical Layered Forward Model for Breasts in Electrical Impedance Tomography. *Physiol Meas. , June*(29(6)), S27-S40.

Laszlo, K., Maximilian, E., Regina, H., Alexander, Z., Markus, S., Armin, S., Matthias, E., Andreas, M., Katja, S.-Z., Nikolaos, A. P., & Edgar, B. (2007). Comparison between breast volume measurement using 3D surface imaging and classical techniques. *The Breast, 16*, 137-145.

Li, J. H. J., C ;Faust, U (1996). Fast EIT data acquisition system with active electrodes and its application to cardiac imaging. *Physiol. Meas., 17*, A25-A32.

Lionheart, W. R. B. (2004). *The reconstruction problem*. Bristol and Philadelphia: Institute of Physics Publishing.

Malich, A., Fritsch, T., Anderson, R., Boehm, T., Freesmeyer, M. G., Fleck, M., & Kaiser, W. A. (2000). Electrical impedance scanning for classifying suspicious breast lesions: first results. *European Radiology, 10*(10), 1555-1561.

McEwan, A., Romsauerova, A., Yerworth, R., Horesh, L., Bayford, R., & Holder, D. (2006). Design and calibration of a compact multi-frequency EIT system for acute stroke imaging. *Physiol Meas., 27*(5), S199-S210.

Metherall, P., Barber, D. C., Smallwood, R. H., & Brown, B. H. (1996). Three-dimensional electrical impedance tomography. *Nature, 380*(6574), 509-512.

Murphy, E. K., Isaacson, D., Saulnier, G. J., & Newell, J. (2010). Analysis of forward solvers for electrical impedance tomography in a mammography geometry. *Journal of Physics: Conference Series, 224*(1), 012033.

Murphy, S. C., & York, T. A. (2006). Electrical impedance tomography with non-stationary electrodes. *Measurement Science & Technology, 17*(11), 3042-3052.

Oh, T. I., Wi, H., Kim do, Y., Yoo, P. J., & Woo, E. J. (2011). A fully parallel multi-frequency EIT system with flexible electrode configuration: KHU Mark2. *Physiol Meas, 32*(7), 835-849.

Osterman, K. S., Kerner, T. E., Williams, D. B., Hartov, A., Poplack, S. P., & Paulsen, K. D. (2000). Multifrequency electrical impedance imaging: preliminary in vivo experience in breast. *Physiol Meas, 21*(1), 99-109.

Phillips, D. L. (1962). A technique for the numerical solution of certain integral equations of the first kind. *J Assoc Comput, Mach*(9), 84-97.

Piperno, G., Frei, E. H., & Moshitzky, M. (1990). Breast cancer screening by impedance measurement. *Front Med Biol Eng. , 1990*(2(2)), 111-117.

Powell, H. M., Barber, D. C., & Freeston, I. L. (1987). Impedance imaging using linear electrode arrays. *Clin Phys Physiol Meas, Vol. 8*(Suppl. A), 109-118.

Samani, A., Bishop, J., Ramsay, E., & Plewes, D. (1999). *A 3-D contact problem finite element model for breast shape deformation derived from MRI data.* Paper presented at the Proc. ASB, 23rd Ann. Meeting (Pittsburg, PA) (American Society of Biomechanics).

Saulnier, G. J., Liu, N., Tamma, C., Xia, H., Kao, T. J., Newell, J. C., & Isaacson, D. (2007). An electrical impedance spectroscopy system for breast cancer detection. *Conf Proc IEEE Eng Med Biol Soc, 2007*, 4154-4157.

Schwan, H. P. (1957). Electrical properties of tissue and cell suspensions. *Adv Biol Med Phys. , 5*, 147-209.

Scott, D. M., & McCann, H. (2005). *Process imaging for automatic control*. New York: Marcel Dekker ; London : Taylor & Francis [distributor].

Sha, L. W., Ward, E. R., & Stroy, B. (2002). A review of dielectric properties of normal and malignant breast tissue. *Ieee Southeastcon 2002: Proceedings*, 457-462.

Shallof, A. M., & Barber, D. C. (1996). *Tissue characterisation using a multi-frequency of electrical impedance tomography.* Paper presented at the Advances in Electrical Tomography (Digest No: 1196/143), IEE Colloquium on London , UK

Smith, A. (2008). Fundamentals of breast tomosynthesis: improving the performance of mammography. *Breast, 2008*, 1-8.

Soni, N. K., Hartov, A., Kogel, C., Poplack, S. P., & Paulsen, K. D. (2004). Multi-frequency electrical impedance tomography of the breast: new clinical results. *Physiol Meas, 25*(1), 301-314.

Stoneman, M. R., Kosempa, M., Gregory, W. D., Gregory, C. W., Marx, J. J., Mikkelson, W., Tjoe, J., & Raicu, V. (2007). Correction of electrode polarization contributions to the dielectric properties of normal and cancerous breast tissues at audio/radiofrequencies. *Phys Med Biol, 52*(22), 6589-6604.

Surowiec, A. J., Stuchly, S. S., Barr, J. R., & Swarup, A. (1988). Dielectric-Properties of Breast-Carcinoma and the Surrounding Tissues. *IEEE Transactions on Biomedical Engineering, 35*(4), 257-263.

Tang, M., Wang, W., Wheeler, J., McCormick, M., & Dong, X. (2002a). Effects of incompatible boundary information in EIT on the convergence behavior of an iterative algorithm. *IEEE Trans Med Imaging, 21*(6), 620-628.

Tang, M., Wang, W., Wheeler, J., McCormick, M., & Dong, X. (2002b). The number of electrodes and basis functions in EIT image reconstruction. *Physiol Meas., 23*(1), 129-140.

Tikhonov, A. N. (1963). Solution of incorrectly formulated problems and the regularization method. *Soviet Mathematics, 4*, 1035-1038.

Tingberg, A. (2010). X-ray tomosynthesis: a review of its use for breast and chest imaging. *Radiat Prot Dosimetry, 139*(1-3), 100-107.

Trokhanova, O. V., Okhapkin, M. B., & Korjenevsky, A. V. (2008). Dual-frequency electrical impedance mammography for the diagnosis of non-malignant breast disease. *Physiol Meas., 29*(6), S331-344.

Tunstall, B., Wang, W., McCormick, M., Walker, R., & Rew, D. (1997). Preliminary in vitro studies of electrical impedance mammography (EIM): a future technique for non-invasive breast tissue imaging ? *The Breast Aug. Vol 6*(4), 253-253.

Tunstall, B., Duan, W., Lu, H., Huber, N., Béqo, N., Sze, G., & Wang, W. (2010). Preliminary findings of a clinical investigation into the use of 3-dimensional impedance imaging for the detection of breast lesions in-vivo. *XIV International Conference on Electrical Bioimpedance and 11th Conference on Biomedical Applications of Electrical Impedance Tomography (ICEBI & EIT 2010) conference proceedings, 224*.

Vauhkonen, M., Vadasz, D., Karjalainen, P. A., Somersalo, E., & Kaipio, J. P. (1998). Tikhonov regularization and prior information in electrical impedance tomography. *IEEE Trans Med Imaging, 17*(2), 285-293.

Vauhkonen, P. J., Vauhkonen, M., Savolainen, T., & Kaipio, J. P. (1999). Three-dimensional electrical impedance tomography based on the complete electrode model. *IEEE Trans Biomed Eng, 46*(9), 1150-1160.

Voges, U., Becker, H., Çakmak, H., Fodor, R., & Klosek, H. (2006). Impedanz-Tomographie-System zur Mamma-Diagnostik und -Therapie. Hermann-von-Helmholtz-Platz 1, 76344 Eggenstein-Leopoldshafen: Institut für Angewandte Informatik.

Wang, W., Brown, B. H., & Barber, D. C. (1995, 11 May 1995). *Performance of the Sheffield Mk3A multi-frequency system for electrical impedance tomography*. Paper presented at the Innovations in Instrumentation for Electrical Tomography, IEE Colloquium on.

Wang, W., Tunstall, B., Chauhan, D., & McCormick, M. (1998). The design of De Montfort Mk2 electrical impedance mammography system. *Proceedings of the 20th Annual International Conference of the Ieee Engineering in Medicine and Biology Society, Vol 20, Pts 1-6, 20*, 1042-1043.

Wang, W., Tang, M., McCormick, M., & Dong, X. (2001). Preliminary results from an EIT breast imaging simulation system. *Physiol Meas, 22*(1), 39-48.

Wang, W., Wang, L., Qiao, G., Prickett, P., Bramer, B., Tunstall, B., & Ai-Akaidi, M. (2007). Study into the repeatability of the electrode-skin interface utilizing electrodes commonly used in Electirical Impedance Tomography. *13th International Conference on Electrical Bioimpedance and the 8th Conference on Electrical Impedance Tomography 2007, 17*, 336-339.

Webster, J. G. (1990). *Electrical Impedance Tomography*: Adam Hilger.

Wheeler, J., Wang, W., & Tang, M. (2002). A comparison of methods for measurement of spatial resolution in two-dimensional circular EIT images. *Physiol Meas, 23*(1), 169-176.

Wu, T., Stewart, A., Stanton, M., McCauley, T., Phillips, W., Kopans, D. B., Moore, R. H., Eberhard, J. W., Opsahl-Ong, B., Niklason, L., & Williams, M. B. (2003). Tomographic mammography using a limited number of low-dose cone-beam projection images. *Med Phys, 30*(3), 365-380.

Xu, G. Z., Wang, R. P., Zhang, S., Yang, S., Justin, G. A., Sun, M. G., & Yan, W. L. (2007). A 128-electrode three dimensional electrical impedance tomography system. *2007 Annual International Conference of the Ieee Engineering in Medicine and Biology Society, Vols 1-16*, 4386-4389.

Ybarra, G. A., Liu, Q. H., Ye, G., Ye, L. K. H., Lee, J. H., Joines, W. T., & George, R. T. *Breast Imaging using Electrical Impedance Tomography (EIT)* (Vol. 2008): American Scientific Publishers.

Ye, G., Lim, K. H., George, R., Ybarra, G., Joines, W. T., & Liu, Q. H. (2006). A 3D EIT system for breast cancer imaging. *2006 3rd Ieee International Symposium on Biomedical Imaging: Macro to Nano, Vols 1-3*, 1092-1095.

Ye, G., Lim, K. H., George, R. T., Ybarra, G. A., Joines, W. T., & Liu, Q. H. (2008). 3d Eit for Breast Cancer Imaging: System, Measurements, and Reconstruction. *Microwave and Optical Technology Letters, 50*(12), 3261-3271.

Yorkey, T. J., Webster, J. G., & Tompkins, W. J. (1987). Comparing reconstruction algorithms for electrical impedance tomography. *IEEE Trans Biomed Eng, 34*(11), 843-852.